JOURNAL OF THE AERONAUTICAL SCIENCES

UNIVERSITY OF MICHIGAN
OCT 22 1951
ENGINEERING LIBRARY

VOLUME 18 OCTOBER, 1951 NUMBER 10

CONTENTS

Exploratory Wind-Tunnel Investigation of Wings and Bodies at $M = 6.9$...CHARLES H. MCLELLAN 641

The Evaluation of Theoretical Critical Compression in Sandwich Plates.....J. N. GOODIER AND I. M. NEOU 649

Allowable Compressive Stresses in Aircraft Structures.....B. E. GATEWOOD AND E. L. WILLIAMS 657

Summary of Recent Experimental Investigations in the N.O.L. Hyperballistics Wind Tunnel.....PETER P. WEGENER 665

Skin-Friction and Heat-Transfer Characteristics of a Laminar Boundary Layer on a Cylinder in Axial Incompressible Flow.....R. A. SEBAN AND R. BOND 671

Analysis of a Friction Damper for Clutch-Type Servomechanisms.....HERBERT K. WEISS 676

The Lift Distribution on Low Aspect Ratio Wings at Subsonic Speeds.....H. R. LAWRENCE 683

Readers' Forum: "Effects of Density Fluctuations on the Turbulent Skin Friction of an Insulated Flat Plate at High Supersonic Speeds," by T. Y. Li and H. T. Nagamatsu; "On Subsonic Conical Methods," by Seymour Lampert; "Small Pitot Tubes with Fast Pressure Response Time," by W. S. Bradfield and G. E. Yale; "Cooling Required To Stabilize the Laminar Boundary Layer on a Flat Plate," by E. R. Van Driest; "Secondary Flow in Cascades," by J. M. Stephenson; "Note on the Hypersonic Similarity Law for an Unyawed Cone," by Lester Lees; "A Limitation on Shock Position," by E. W. Graham; "Comment on 'Vibration of Rectangular Plates,'" by Charles Massonnet; "Author's Reply," by Harold Lurie; "Shear Flow in a Thin-Skin Tapered Beam," by H. W. Sibert.....696–704

Published by the

INSTITUTE OF THE AERONAUTICAL SCIENCES, INC.

JOURNAL OF THE AERONAUTICAL SCIENCES

Editor: HUGH L. DRYDEN, *Director, N.A.C.A.*

Associate Editor: ROBERT R. DEXTER *Managing Editor:* BERNEICE H. JARCK

Editorial Committee

Aerodynamics

Francis Clauser
Howard Emmons
Alexander Flax
R. Paul Harrington
R. T. Jones
Carl Kaplan
H. W. Liepmann
C. C. Lin
H. F. Ludloff
Harold Luskin
John R. Markham
Clark B. Millikan
Shatswell Ober
W. Bailey Oswald
Allen E. Puckett
Elliott G. Reid
H. J. F. Reid
Russell Robinson
G. B. Schubauer
W. R. Sears
John Stack
Theodore von Kármán
Richard von Mises

Flight Testing

W. K. Ebel
R. R. Gilruth
Melvin N. Gough
E. G. Stout

Meteorology

C. F. Brooks
D. M. Little
E. J. Minser
F. W. Reichelderfer
H. C. Willett

Structures and Materials

W. B. Bleakney
E. W. Conlon
L. H. Donnell
E. C. Hartmann
N. J. Hoff
Samuel Levy
E. E. Lundquist
J. S. Newell
Alfred S. Niles
W. Ramberg
E. Reissner
F. R. Shanley
H. W. Sibert
C. R. Strang
S. Timoshenko
H. S. Tsien
Chi-Teh Wang

Rotating Wing Aircraft

F. B. Gustafson
K. H. Hohenemser
Bartram Kelley
R. B. Maloy
Ralph McClarren
R. H. Miller
R. H. Prewitt
Igor I. Sikorsky

Physiologic Problems

H. G. Armstrong
Louis H. Bauer
Eugene Du Bois
W. Randolph Lovelace, II
Ross A. MacFarland
A. D. Tuttle

Flight Propulsion

George W. Brady
Frank W. Caldwell
L. S. Hobbs
E. E. Johnson
Joseph Keenan
R. P. Kroon
Hans Reissner
Abe Silverstein
C. Fayette Taylor
E. S. Taylor
P. Taylor
E. S. Thompson
H. S. Tsien

Aircraft Design

W. E. Beall
W. K. Ebel
Hall L. Hibbard
Richard Hutton
C. L. Johnson
A. A. Kartveli
C. J. McCarthy
Fred E. Weick
Robert J. Woods

Air Transport

Charles Froesch
J. A. Herlihy
R. D. Kelly
Otto B. Kirchner
Jerome Lederer
John C. Leslie
R. Dixon Speas

Instruments

Allan G. Binnie
W. G. Brombacher
Charles H. Colvin
B. M. Craig
C. S. Draper
S. G. Eskin
O. E. Esval
W. L. Howland
George H. Purcell
C. F. Savage
O. Hugo Schuck
L. N. Schwien
C. L. Seward, Jr.
L. D. Statham
R. C. Sylvander
D. K. Warner
P. F. Weber
Elmer P. Wheaton

Vibration and Flutter

Lee Arnold
M. A. Biot
R. L. Bisplinghoff
William Bollay
Chieh-Chien Chang
I. E. Garrick
Martin Goland
J. P. Den Hartog

Fuels and Oils

D. P. Barnard
J. H. Doolittle
Graham Edgar
R. T. Goodwin
S. D. Heron
A. M. Rothrock

SUBSCRIPTION RATES

JOURNAL OF THE AERONAUTICAL SCIENCES, Published Monthly.—United States and Possessions: 1 Year, $12.00; Single Copies, $1.50. Foreign Countries Including Canada (American Currency Rates): 1 Year, $13.00; Single Copies, $1.50.

AERONAUTICAL ENGINEERING REVIEW, Published Monthly.—United States and Possessions: 1 Year, $3.00; Single Copies, $0.50. Foreign Countries Including Canada (American Currency Rates): 1 Year, $3.50; Single Copies, $0.50.

Notices of change of address should be sent to the Institute at least 30 days prior to actual change of address.

Manuscripts for publication, proofs, and all correspondence should be addressed to the Editorial Office of the JOURNAL.

Correspondence regarding subscriptions may be addressed to Publication Office, 20th and Northampton Sts., Easton, Pa., or to the Editorial Office of the JOURNAL OF THE AERONAUTICAL SCIENCES, 2 East 64th Street, New York 21, New York.

Copyright, 1951, by the Institute of the Aeronautical Sciences, Inc.

Entered as Second Class Matter at the Post Office, Easton, Pa., May 1, 1937. Acceptance for mailing at a special rate of Postage provided for in the Act of August 24, 1912. Authorized April 29, 1937.

JOURNAL OF THE AERONAUTICAL SCIENCES

VOLUME 18 OCTOBER, 1951 NUMBER 10

Exploratory Wind-Tunnel Investigation of Wings and Bodies at $M = 6.9$

CHARLES H. McLELLAN*

Langley Aeronautical Laboratory, N.A.C.A.

SUMMARY

Results of an exploratory investigation of wings and bodies at a Mach Number of 6.9 in the Langley 11-in. hypersonic tunnel are presented. Force data were obtained on a square and a triangular plan-form wing having 5 per cent thick diamond sections, on a circular cone-cylinder body, and on a semicircular cone-cylinder body. Pressure-distribution data were also obtained on the square plan-form wing and the circular body.

The results have been compared with calculations made by various theoretical methods. The more exact theoretical treatments gave overall force values in good agreement with experimental results. Measured pressure distributions departed appreciably from calculated results in some cases because of the influence of boundary layer.

INTRODUCTION

IN EVALUATING THE PERFORMANCE of contemplated missiles at high supersonic (hypersonic) Mach Numbers, it has been necessary up to this time to use theoretical results without experimental verification. An 11-in. hypersonic wind tunnel capable of providing the necessary experimental data has recently been developed and put into operation by the N.A.C.A. at its Langley laboratory. The purpose of the present paper is to discuss the results of an exploratory investigation of wings and bodies in this new facility at a Mach Number of 6.9 and to compare these results with available theories.

SYMBOLS

c = wing chord
C_c = wing chordwise force coefficient
C_D = wing or body drag coefficient based on plan-form area
C_L = wing or body lift coefficient based on plan-form area
$C.P.$ = center of pressure
D = drag
L = lift
p_1 = free-stream static pressure
p_2 = surface pressure
α = angle of attack
β = radial position measured from the top of the body

Presented at the Hypersonic Aerodynamics Session, Nineteenth Annual Meeting, I.A.S., New York, January 29–February 1, 1951.

* Head, 11-In. Hypersonic Tunnel Section.

DESCRIPTION OF APPARATUS AND MODELS

Tunnel

The Langley 11-in. hypersonic tunnel is shown schematically in Fig. 1. Air is discharged from a 50-atmosphere high-pressure tank through a pressure regulator to a heater, where it is heated to about 700°F. After leaving the heater, the air is expanded through a two-dimensional single-step nozzle designed for a Mach Number of 7.08 and then passes through an adjustable second throat to a vacuum tank. The tunnel is described more fully in reference 1, and the results of surveys of the flow through the nozzle are presented in reference 2. The flow surveys showed that the Mach Number at the test section was approximately 6.9 and that a central core of the stream having a cross section about 5 in. square had sufficiently uniform flow for model testing.

The high stagnation temperature used in the present tests is required to maintain the air temperature in the test section above the liquefaction temperature of air at the test-section pressure. The presence of liquid air particles in the nozzle has been observed when a sufficiently high stagnation temperature was not used. Furthermore, for this condition, pressure measurements in the flow have shown that large increases in entropy occur which are indicative of liquefaction. It is therefore believed essential that the high stagnation temperature be used. This problem of liquefaction is discussed in greater detail in reference 3.

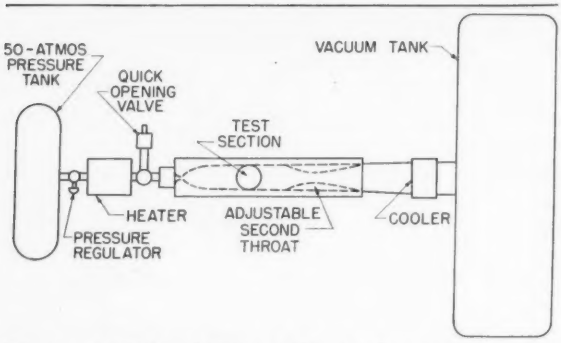

FIG. 1. Schematic diagram of the N.A.C.A. Langley 11-in. hypersonic tunnel.

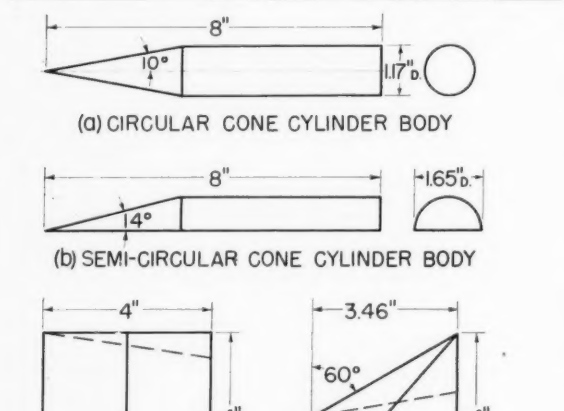

FIG. 2. Wing and body configurations tested.

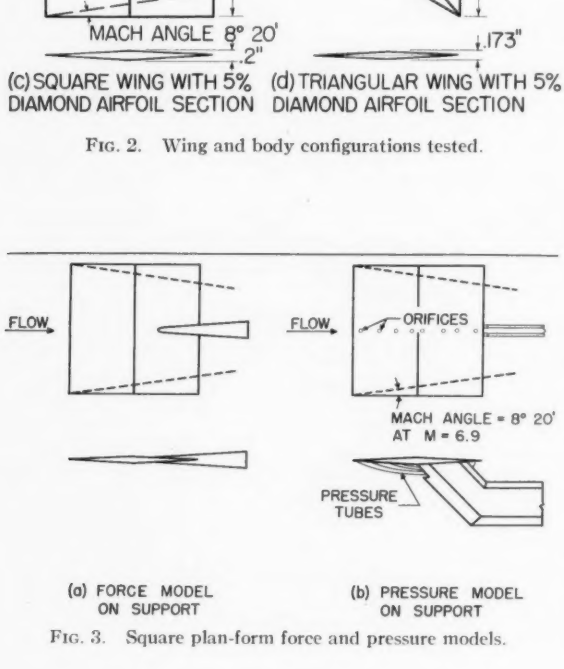

FIG. 3. Square plan-form force and pressure models.

Models

The four models used in this investigation are shown in Fig. 2. The two body shapes consisted of a circular cone-cylinder body having a 10° half-angle circular cone with a cylindrical afterbody four diameters in length and a semicircular cone-cylinder body having the lower surface flat. The cross-sectional areas of the two bodies were equal at corresponding streamwise stations; thus the cone angle was increased for the flat-bottomed body. Two wings were also included. One had a square plan form, and the other had a triangular plan form with 60° swept leading edges. Both wings had 5 per cent thick diamond airfoil sections. The test Reynolds Number was approximately 1,000,000 based on the 4-in. chord of the square plan-form wing. This Reynolds Number corresponds to a wing of 4-ft. chord flying at a Mach Number of 7 at an altitude of about 120,000 ft. Fig. 2 also shows the small portions of the wings which lie within the regions of three-dimensional flow from the tips of the square plan-form wing and from the apex of the delta wing.

Instrumentation

Both pressure and force measurements were made on the circular body and the square plan-form wing, while only force measurements were made on the semi-circular body and the triangular plan-form wing. The forces were measured by means of a strain-gage balance located in the sting support of the model. The wing force models were attached to the balance by the conical support shown in Fig. 3a. Corrections to the lift and drag due to the aerodynamic forces on the unshielded portion of the conical support have been applied to the wing force test results. The two body force models were mounted on a support that was shielded from the stream. Two balances were used—one for low angles of attack where the forces were extremely small, and one for the high angles of attack where the forces were relatively large.

The pressures on the circular cone-cylinder body were measured by one row of orifices running the length of the body. Pressure measurements around the model at angles of attack were obtained by rotating the model about its longitudinal axis.

Fig. 3b shows the chordwise row of orifices that were used to obtain the pressure distributions on the square plan-form wing. It can be seen that the area affected by the three-dimensional flow at the tips is small and that the distributions obtained by these orifices will be essentially two-dimensional. Since the model was extremely thin, it was impractical to locate the connecting pressure tubes entirely within the model. Tubes were therefore brought out through the surface opposite the one in which the measurements were being made. Experimental studies have indicated that the presence of these tubes and the model support does not have a measurable effect on the flow over the

top of the wing. The pressures were measured by means of optically recording aneroid units described in reference 1.

Results and Discussion

Wing Pressure Distributions

With the aid of existing supersonic flow tables, the pressure distribution in the two-dimensional flow region of the square plan-form wing can be easily determined by the use of the characteristics system, and there is little reason to use the approximate methods. A comparison of the experimental and theoretical pressure distribution for the square plan-form wing is shown in Fig. 4 for angles of attack of 0° and 10°. The pressure distributions are presented in the form of a local static pressure p_2 minus the stream static pressure p_1 divided by the stream static pressure. This ratio has a value of zero when the local surface pressure is equal to the stream pressure and is -1 at zero absolute surface pressure. Theoretical pressures obtained by the characteristics system are presented as dotted curves. The results indicate large deviations of the experimental pressures from the theoretical values near the leading edge of the wing. A similar deviation occurs just back of the break in the surface at the maximum thickness. The deviation results from the rapid growth of boundary layer near the leading edge and just back of the maximum thickness at the high test Mach Number.

A study of the growth of boundary layer at this Mach Number showed that, at the test Reynolds Number of 1,000,000, the calculated pressure rise near the leading edge due to a laminar boundary layer was in good agreement with the experimental deviation of the pressures from theory. At a Mach Number of 7, the boundary-layer displacement thickness is about ten times as great as at a Mach Number of 1 at the same Reynolds Number. This thick boundary layer can be seen in the schlieren photograph of the square plan-form wing presented in Fig. 5.

At 10° angle of attack, the flow over the rear surface of the wing is separated, and the pressures remain constant at the same value as for the forward upper surface. It is evident from the pressure diagram (Fig. 4) that this flow separation has only a small effect on the lift because of the small lift contribution of the upper surface at high Mach Numbers.

Wing Force Characteristics

There is no available theoretical method for rigorous calculation of the characteristics of the complete wings. The linearized theory, however, may be used for an approximate evaluation of the tip effects. In the case of the square wing, the tip effect reduces the lift-curve slope by 7 per cent. Analysis of the pressure data (Fig. 4) indicates that the section lift-curve slope is reduced by about the same amount because of viscous effects. Thus, a total reduction in slope of about 15 per cent below the two-dimensional values obtained by the characteristics method would be anticipated. The test data (Fig. 6) indicated a reduction of about 10 per cent. It would appear from this result that the tip effect is overestimated by the linearized theory. Further investigation is required to evaluate the tip effect more accurately. In Fig. 6, the lift curve, calculated by Linnell's hypersonic approximation for two-dimensional flow[4] is essentially the same as for the characteristics theory at low and moderate angles of

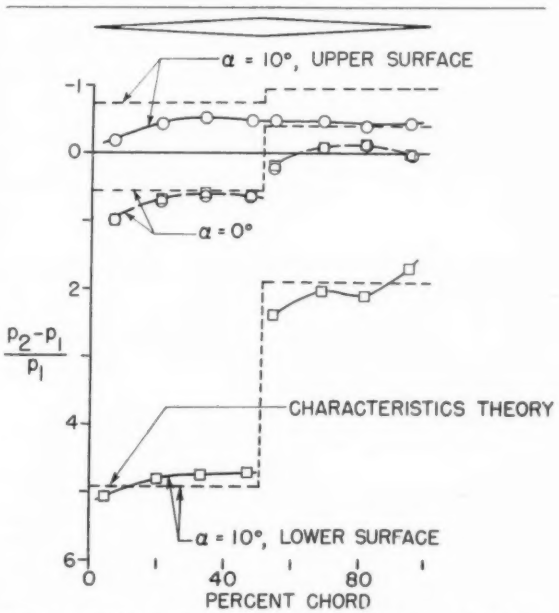

FIG. 4. Typical pressure distributions on the square plan-form wing, $M = 6.9$.

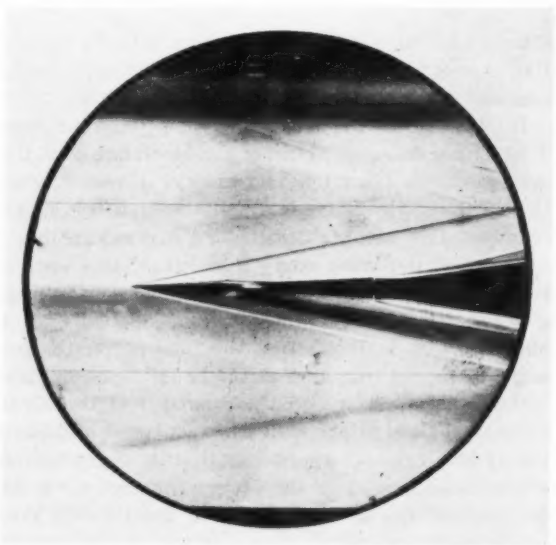

FIG. 5. Schlieren photograph of flow about the square plan-form wing, $\alpha = -0.5°$, $M = 6.9$.

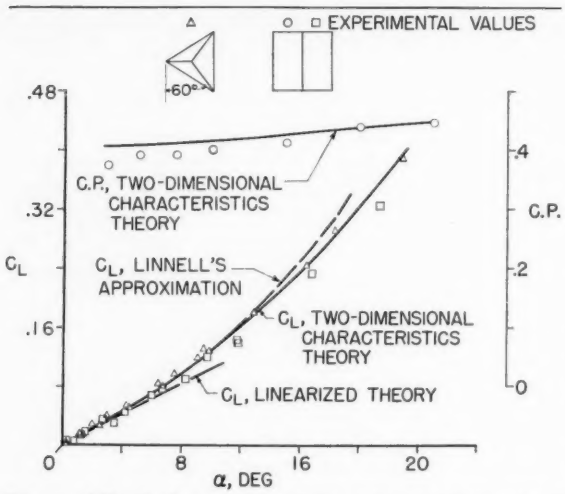

FIG. 6. Lift of the square and the delta plan-form wings, $M = 6.9$.

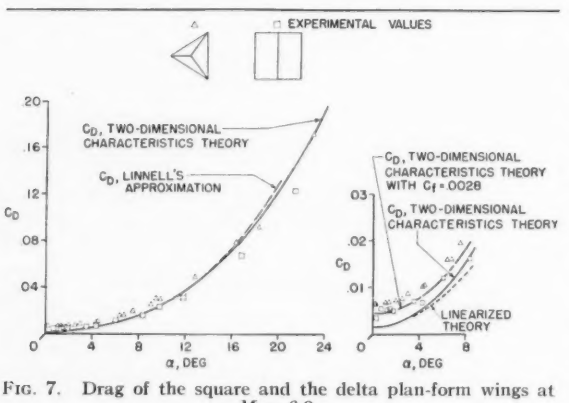

FIG. 7. Drag of the square and the delta plan-form wings at $M = 6.9$.

attack, while at high angles, which are actually beyond the range in which it should be applied, it is appreciably greater.

In the case of the triangular wing, only the two-dimensional flow area ahead of the Mach line from the apex can be analyzed by exact theory. However, with the 60° swept leading edges and the high test Mach Number, this area constitutes approximately three-quarters of the wing area. The lift of this area is slightly greater than for a two-dimensional wing. The linearized theory, which can be applied at low angles of attack, shows that the total lift of the triangular wing is the same as the two-dimensional lift. The lift has therefore been compared over the whole range of angle of attack with the exact two-dimensional theory in Fig. 6. It can be seen that the experimental slope is approximately the same as predicted by the two-dimensional theory and slightly greater than that for the square plan-form wing. The difference between the two-dimensional theoretical results and the test data from the delta wing is probably of the same magnitude as the experimental errors because of the accuracy of the measurements and the errors in evaluating the effect of the support sting on the forces on the delta wing.

The center of pressure as obtained from pressures along the centerline of the square wing is also presented in Fig. 6. The measurements indicate that the center of pressure is slightly more forward at low angles of attack than theory predicts and tends to become equal to the theoretical value at high angles.

The drag characteristics from the force measurements for the two wings are presented in Fig. 7. The solid curve shown in this figure is the drag coefficient calculated by the two-dimensional characteristic theory. The linearized theory gives essentially the same drag coefficients for the two wings. At zero angle of attack, the linearized theory gives drags that are nearly equal to the two-dimensional theoretical drag. However, as the angle is increased, the rate of increase of the drag coefficient from the linearized theory is appreciably less than for the characteristic theory, since the lift is underestimated by the linearized theory.

Linnell's hypersonic approximation gives essentially the same drag as the characteristics theory at low and moderate angles and only slightly higher drags at high angles of attack, although they are beyond the angles at which this theory would be expected to apply.

At low angles, the drag of the square plan-form wing measured by the balances is appreciably greater than the inviscid theory predicts. However, when a friction drag coefficient of 0.0028 calculated for laminar flow at the test Reynolds Number is added to the inviscid theoretical drag, the total agrees with the force measurements. The value of the friction drag coefficient is twice the pressure drag coefficient at zero angle of attack. Of course, the 5 per cent diamond section used in this investigation has a relatively low pressure drag. Only moderate percentage reductions in total drag could therefore be obtained for this section by reducing the wing thickness below 5 per cent at the test Reynolds Number. From the same standpoint, changing to a wing section that might be expected to have lower pressure drag, such as a wedge with the point of maximum thickness at the trailing edge, will have only a secondary effect on the total drag. If it is assumed that the boundary layer remained laminar, the effect of the thickness and wing section would be relatively greater at higher Reynolds Number. However, the test Reynolds Number is within the range of interest in missile applications.

Fig. 7 shows that the drag of the delta wing is slightly higher than that of the square wing at high angles of attack, mainly because of the higher lift. At low angles, the drag is about 30 per cent higher than for the square wing. The linearized theory indicates that the pressure drag of the delta wing is only about 2 per cent greater than for the square wing. The increase is primarily a result of a decrease in the effective Reynolds

Number of the delta wing. Based on the local chord, the delta-wing Reynolds Number is about 90 per cent of that of the square wing at the centerline and decreases to zero at the tip.

Lift-drag ratio data for the wings are presented in Fig. 8 as a function of angle of attack. The theoretical curve obtained using the inviscid two-dimensional characteristic theory is compared with the values given by the diamond symbols that were obtained from an integration of the pressures over the centerline of the square wing. It can be seen that the pressure results are in reasonable agreement with the inviscid theory and indicate a maximum L/D of over 10.

When friction is included, the theoretical curve of L/D drops appreciably at low angles, and the maximum L/D is about 6, which is about 25 per cent less than that expected at a Mach Number of 2. Since considerable scatter exists in the force data for the square plan-form wing (the square symbols), it appears that the theoretical curve with friction can be considered to represent approximately a faired curve of the data. Considerably less scatter is evident in the force data from the delta wing (the triangular symbols) because of improved instrumentation and techniques. The L/D of the delta wing is slightly lower than for the square wing, primarily as a result of the lower effective Reynolds Number of the delta wing. At high angles, there is no noticeable difference in lift-drag ratio of the two wings; in fact, they closely approach the calculated curve corresponding to a flat plate with no chordwise component. This curve is independent of Mach Number and represents an upper limit for any airfoil regardless of the plan form, provided no leading-edge suction is obtained. At the higher angles of attack, the pressure L/D values are close to the limiting curve.

Because of the large frictional component of the drag, it appears that an appreciable increase in maximum L/D could be effected for a wing of given area and thickness ratio by reducing the aspect ratio, thereby increasing the Reynolds Number. At Mach Numbers of the order of 7 or higher, it appears from this investigation that aspect ratios considerably lower than unity can be used without appreciable loss of lift-curve slope.

In order to illustrate the nature of the flow about the wing, a schlieren photograph of the square plan-form diamond airfoil wing mounted on the sting balance at an angle of attack of $-16.8°$ is shown in Fig. 9. In this photograph, it can be seen that the shock is close to the high-pressure surface of the model. On the low-pressure side of the model, an expansion to a Mach Number of nearly 11 just back of the leading edge would be expected in the absence of viscous effects; however, a rapid growth of boundary layer results in the occurrence of a shock at the leading edge. A maximum Mach Number of about 8 occurs well back of the leading edge. Separation occurs at about the maximum thickness on the low-pressure side at this angle of attack.

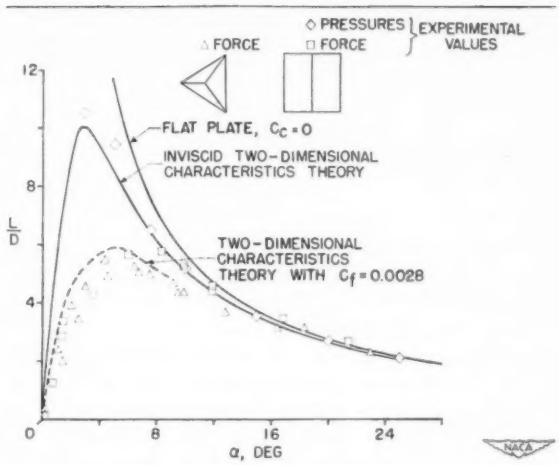

FIG. 8. Lift-drag ratio of the square and the delta plan-form wings at $M = 6.9$.

FIG. 9. Schlieren photograph of flow about the square plan-form wing, $\alpha = -16.8°$, $M = 6.9$.

Cone Pressure Distributions

One of the simpler cases of bodies of revolution to analyze is the cone-cylinder body at zero angle of attack. In this case, the pressures on the forward or conical portions of the body can be obtained from the work of Taylor and Maccoll,[5] which has been calculated and tabulated by the M.I.T. group in reference 6. The flow over the rear or cylindrical portion can be calculated using the flow from the conical portion and the three-dimensional characteristics system. For the particular body used in this investigation, it is not possible to apply the linearized theory because the half-cone angle of 10° is greater than the Mach angle. A comparison of the theoretical and the experimental results is presented in Fig. 10. On the conical portion

and on the rear of the cylindrical portion of the body, the experiment and theory agree, while on the cylindrical surface near the cone-cylinder juncture, the pressures are considerably higher than predicted by theory. This is believed to be largely due to the boundary layer altering the effective body shape at the juncture.

At angles of attack, several approximate theories are available for analyzing the flow about the conical portion of the body. The radial distribution of the pressure ratio $(p_2 - p_1)/p_1$ around the cone measured in degrees from the top of the cone is compared with the available theories in Fig. 11 for an angle of attack of 6.7°. Experimental points at each radial station are presented for several longitudinal stations. The points nearest the leading edge should probably be ignored because they are affected by local conditions such as accuracy of the cone at the point and rapid boundary-layer growth near the leading edge. A first-order theory, shown as the solid line, was developed by Stone[7] and was tabulated by an M.I.T. group under the supervision of Kopal.[8] This work, which will be referred to as the Stone-Kopal theory, is a first-order theory that assumes that the entropy is constant in any meridian plane but varies with position around the cone. In addition to the usual angle-of-attack limitations of a first-order theory, the Stone-Kopal theory is limited to angles of attack less than the half-cone angle, since the coordinate system is based on the wind axis. A more recent theory has been developed by Ferri[9] which uses a coordinate system about the body axis instead of the wind axis and which introduces the concept of a vortical layer next to the cone surface. The entropy is shown by Ferri to be constant on the cone surface except for a singular point at the top of the cone. In the work of Stone, the entropy was allowed to vary around the surface. The change in the axis of the coordinate system allows for solutions of the equations at angles of attack greater than the surface cone angle, although the theory is not expected to be valid at high angles of attack. A third theory, presented in Fig. 11, was developed by Grimminger[10] and is based upon the Newtonian corpuscular concept in which the gas stream maintains its speed and direction unchanged until it strikes the solid surface, whereupon it loses the component of momentum normal to the surface. This approximation of the flow is valid at high supersonic Mach Numbers, particularly when the angle of attack is appreciable. However, this method does not predict the pressures on surfaces shielded from the flow. Refinements of this theory, which include the centrifugal forces of the air as it flows about the body, were also presented by Grimminger. The case included in Fig. 11 assumes the velocity over the surface to be the component of the free-stream velocity parallel to the surface.

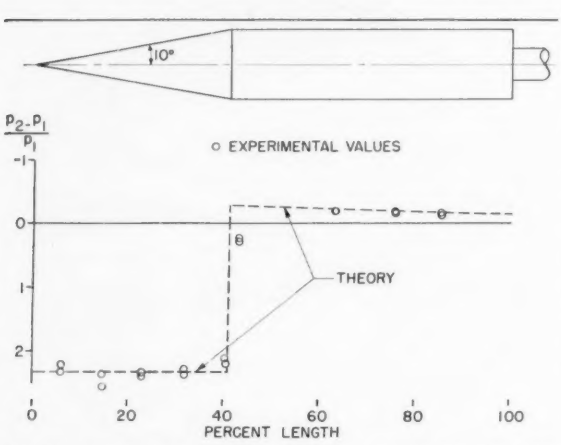

FIG. 10. Pressure distribution on the circular cone-cylinder body at zero angle of attack, $M = 6.9$.

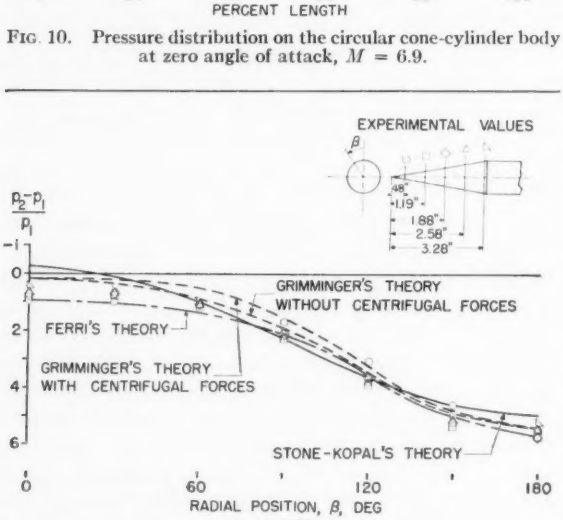

FIG. 11. Pressure distribution around the conical portion of the circular cone-cylinder body at an angle of attack of 6.7°, $M = 6.9$.

At 6.7° angle of attack, the results from Stone's work give approximately the same values as experiment at the sides of the models but appreciably lower values at the top and bottom. The Ferri values are in considerably better agreement; however, they tend to be slightly high near the top of the cone. Grimminger's results, without allowance for centrifugal force, agree reasonably well with the experimental data on the high-pressure portion of the cone but are slightly low on the low-pressure or upper surface. The inclusion of the centrifugal force in Grimminger's theory increases the discrepancy at the test Mach Number. Grimminger[10] also showed that the method used overemphasized the effect of the centrifugal forces and suggested several methods for reducing the calculated centrifugal forces. These reduced values would have given better agreement but not so good as without the centrifugal force corrections.

At an angle of attack of 14°, the results of Stone's work can no longer be applied. Although this angle of attack is beyond the range for which first-order theories in general successfully approximate the physical phenomenon, nevertheless, the application of Ferri's theory

yields good agreement over the high-pressure portion of the cone but gives slightly higher pressures than experiment over the low-pressure surface. However, it should be pointed out that, over the top of the cone, the pressures are probably affected to a considerable extent by boundary-layer flow about the cone. Grimminger's hypersonic approximation without centrifugal force agrees extremely well with the experiment; however, it cannot be applied on the upper 28 per cent of the model. The inclusion of centrifugal force again increases the discrepancy.

Body Force Characteristics

Of the various approximate theoretical methods used in the analysis of the flow about the cone at angle of attack, only Grimminger's method can be readily applied to the flow about a complete body of circular cross section. The work of Ivey[11] can only be applied on the cylindrical portion of the body and must be used in conjunction with other theories for the conical portion of the body. The approximate method of Grimminger applies to both the cylinder and the cone.

Lift coefficients based on the projected area of the circular cone-cylinder body are presented in Fig. 13 as a function of angle of attack. The theoretical values based on Grimminger's approximation are included for the circular cone-cylinder body. To permit a comparison of the lift of the bodies with that of the wings, the theoretical curve of lift versus angle of attack for the 5 per cent diamond profile has been included. The lift predicted by the hypersonic theory is slightly higher than the experimental values for the circular body. It is interesting to note that the circular body has a lift-curve slope of about 60 per cent as great as that for a wing.

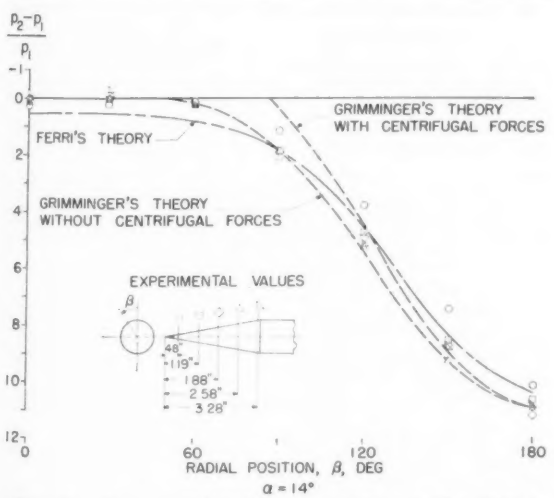

FIG. 12. Pressure distribution around the conical portion of the circular cone-cylinder body at an angle of attack of 14°, $M = 6.9$.

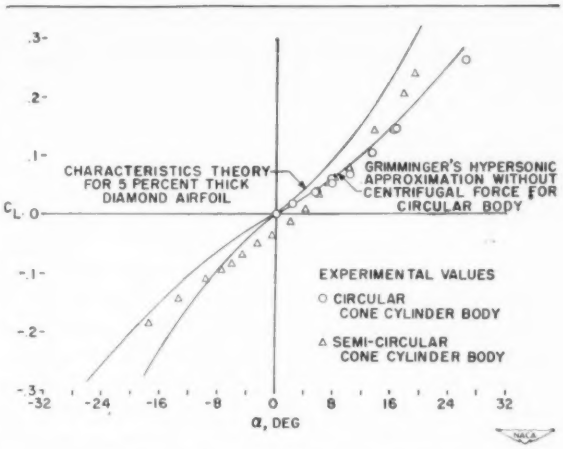
CHARACTERISTICS THEORY FOR 5 PERCENT THICK DIAMOND AIRFOIL
GRIMMINGER'S HYPERSONIC APPROXIMATION WITHOUT CENTRIFUGAL FORCE FOR CIRCULAR BODY
EXPERIMENTAL VALUES
CIRCULAR CONE CYLINDER BODY
SEMI-CIRCULAR CONE CYLINDER BODY
C_L
α, DEG

FIG. 13. Variation of lift coefficient with angle of attack for the two bodies at $M = 6.9$.

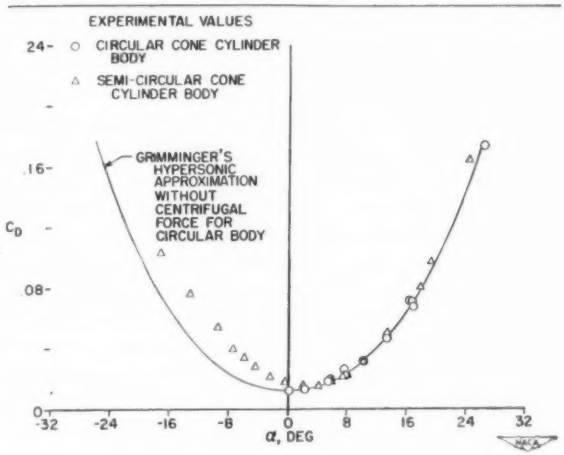

FIG. 14. Variation of drag coefficient with angle of attack for the two bodies at $M = 6.9$.

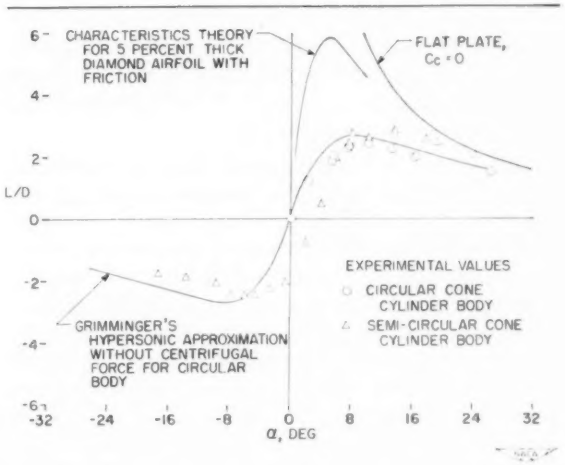
CHARACTERISTICS THEORY FOR 5 PERCENT THICK DIAMOND AIRFOIL WITH FRICTION
FLAT PLATE, $C_c = 0$
L/D
EXPERIMENTAL VALUES
CIRCULAR CONE CYLINDER BODY
SEMI-CIRCULAR CONE CYLINDER BODY
GRIMMINGER'S HYPERSONIC APPROXIMATION WITHOUT CENTRIFUGAL FORCE FOR CIRCULAR BODY
α, DEG

FIG. 15. Variation of lift-drag ratio with angle of attack for the two bodies at $M = 6.9$.

Lift data for the flat-bottomed body with semicircular cross section are also included in Fig. 13. As shown by Sanger,[12] bodies of this type are of interest in hypersonic applications because they have the possibilities of increased lift-curve slope, increased lift at maximum L/D, and higher maximum L/D than comparable round bodies. It can be seen that the body having the semicircular cross section has a lift-curve slope considerably greater than the circular cross-section body; in fact, its slope is about the same as that for a two-dimensional wing. It should also be noted in Fig. 13 that, as expected, the slope of the lift curve at negative angles (the curved portion on the high-pressure side) approaches that of the circular body more nearly than that of the wing.

The drag coefficients based on the plan-form area for the two bodies are plotted against angle of attack in Fig. 14. Comparison of the results of force and pressure measurements on the circular body shows that, for this relatively low fineness ratio circular body, only 15 per cent of the drag at zero angle of attack is due to friction. This compares favorably with the calculated friction drag assuming the flow is entirely laminar. The theoretical values of total drag for the circular body are slightly higher over most of the range than experimental values, even though friction is not included in the theory. At high angles, some of the loss in drag can be accounted for by the lift being lower than predicted. The differences in drag coefficients of the two bodies based on the projected area in this figure are small; however, if the drag coefficients are based on maximum cross-sectional area, the drag coefficient of the semicircular body would be about 40 per cent larger than for the circular body. The higher drag is largely due to the blunter-cone angle of the semicircular body.

The lift-drag ratios of the bodies are presented in Fig. 15. A curve of L/D based on the theory of Grimminger is included for the circular bodies. The experimental lift-drag ratios of the circular body are only slightly lower than those in this nonviscous theory. This is largely the result of the fact that the pressure drag constitutes the major part of the drag because of the low fineness ratio of this body.

Although early data indicated that the maximum lift-drag ratios of the two bodies were essentially the same, the more recent test results of Fig. 15, in which the experimental scatter has been greatly reduced by the use of improved instrumentation and techniques, show that the maximum lift-drag ratio of the flat-bottomed body is about 15 per cent greater than for the circular body. This trend was anticipated from the work of Sanger.[12] The maximum lift-drag ratio also occurs at a higher angle of attack and lift coefficient for the flat-bottomed body than for the circular body.

At high angles of attack, the L/D values approach the values for a flat plate, indicating that at these high angles of attack the bodies will give about the same L/D values as any other good lifting surface. The theoretical L/D curve for the 5 per cent diamond wing section with friction is also included for comparative purposes. It can be seen that, at the test Reynolds Numbers, the maximum L/D of the bodies is about half that of the wing section. The L/D ratios of these bodies will not be affected to nearly the same extent by Reynolds Number as the wings, since the friction is a considerably smaller portion of the overall drag.

Concluding Remarks

From the results of this exploratory investigation, it can be concluded that the aerodynamic characteristics of wings and bodies at a Mach Number of the order of 7 can be predicted by available theoretical methods with the same order of accuracy usually obtainable at lower speeds, at least for cases in which the boundary layer is laminar. Allowance should be made for the effects of the relatively thick boundary layers, which occur at the high test Mach Number, in altering the effective shape of the wing or body, especially near the wing leading edge.

References

[1] McLellan, C. H., Williams, T. W., and Bertram, M. H., *Investigation of a Two-Step Nozzle in the Langley 11-Inch Hypersonic Tunnel*, N.A.C.A. T.N. No. 2171, 1950.

[2] McLellan, C. H., Williams, T. W., and Beckwith, I. E., *Investigation of the Flow through a Single Stage Two-Dimensional Nozzle in the Langley 11-Inch Hypersonic Tunnel*, N.A.C.A. T.N. No. 2223, 1950.

[3] Becker, John V., *Results of Recent Hypersonic and Unsteady Flow Research at the Langley Aeronautical Laboratory*, Journal of Applied Physics, Vol. 21, No. 7, pp. 619–628, July, 1950.

[4] Linnell, Richard D., *Two-Dimensional Airfoils in Hypersonic Flows*, Journal of the Aeronautical Sciences, Vol. 16, No. 1, pp. 22–30, January, 1949.

[5] Taylor, G. I., and Maccoll, J. W., *The Air Pressure on a Cone Moving at High Speeds*, Proc. Roy. Soc. London, Series A, Vol. 139, pp. 278–311, 1933.

[6] Staff of the Computing Section, Center of Analysis (Under Direction of Zdeněk Kopal), *Tables of Supersonic Flow around Cones*, M.I.T., Tech. Report No. 1, 1947.

[7] Stone, A. H., *On Supersonic Flow Past a Slightly Yawing Cone*, Jour. Math. & Phys., Vol. 27, No. 1, pp. 67–81, April, 1948.

[8] Staff of the Computing Section, Center of Analysis (Under Direction of Zdeněk Kopal), *Tables of Supersonic Flow around Yawing Cones*, M.I.T., Tech. Report No. 3, 1947.

[9] Ferri, Antonio, *Supersonic Flow Around Circular Cones at Angles of Attack*, N.A.C.A. T.N. No. 2236, September, 1950.

[10] Grimminger, G., Williams, E. P., and Young, G. B. W., *Lift on Inclined Bodies of Revolution in Hypersonic Flow*, Journal of the Aeronautical Sciences, Vol. 17, No. 11, pp. 675–690, November, 1950.

[11] Ivey, H. Reese, and Morrissette, Robert R., *An Approximate Determination of the Lift of Slender Cylindrical Bodies and Wing-Body Combinations at Very High Supersonic Speeds*, N.A.C.A. T.N. No. 1740, October, 1948.

[12] Sanger, E., and Bredt, J., *A Rocket Drive for Long Range Bombers*, Translation CGD-32, BuAer, Navy Department, August, 1944.

The Evaluation of Theoretical Critical Compression in Sandwich Plates*

J. N. GOODIER† AND I. M. NEOU‡
Stanford University

ABSTRACT

Formulas for the critical compression of sandwich plates, which take into account everything that might influence the buckling load, are extremely complex. When simplicity is achieved by concessions in accuracy, the range of validity is not easily distinguished. The evaluations presented here use check points obtained from an "exact" analysis to test the accuracy of simpler formulas, with the result that one of the latter (proposed in reference 5) is found to be remarkably accurate over a wide range of geometrical and elastic parameters.

(1) INTRODUCTION AND SUMMARY OF RESULTS

THE COMPRESSIVE STRENGTH of thin sheets can be realized only if they are stabilized against buckling. In sandwich construction, two such sheets are bonded to a core slab of different (light) material. The core is sometimes isotropic, sometimes anisotropic. Only the isotropic case is considered here.

Panels of this construction give rise to a set of problems of strength, stiffness, and stability analogous to, but by no means identical with, the well-known problems of the ordinary homogeneous and isotropic elastic plate. One of these is "cylindrical buckling," illustrated in Fig. 1. The panel is so wide that lines such as EF can be taken as uncurved. In the ordinary plate, a unit width is treated as a Euler column, but, since anticlastic curvature is prevented, the Young's modulus E is replaced by $E/(1 - \nu^2)$, ν being Poisson's ratio.**

If it could be assumed that plane sections remained plane, the corresponding sandwich problem would require merely a straightforward modification to take account of the fact that the section is composite rather than homogeneous.†† This assumption will be valid when the modulus of the core (E_c) and the modulus of the face sheets (E_f) are not too far apart. The sandwich constructions of interest to aeronautical engineers have light cores with low moduli—not so low that they leave the sheets practically free to buckle as independent sheets and not so high that plane sections remain plane. The actual buckling is either like column buckling (quasi-Euler buckling) or a short wave "wrinkling" of the face sheets. In the former, the core may exhibit a substantial shearing deformation; in the latter, it acts like an elastic foundation, and the buckling deformation may be confined to the layers adjacent to the face sheets. These statements rest on the numerous investigations published during the past 10 years. (A few of these are cited in the list of references.)

One group of these deals only with the quasi-Euler buckling, the procedure simplest in principle being the introduction of the "correction due to shear" in the elementary bending theory. Another group deals with both quasi-Euler buckling and with wrinkling, treating the core deformation by the methods of the ordinary theory of elasticity. This involves the assumption that the (usually small) compressive load borne by the core does not influence its response to lateral forces. A third group goes further by taking this influence into account. The theory used for the core is an extension of the ordinary theory of elasticity developed in the past 20 years which can deal, in general, with elastic deformations in the presence of initial stress severe enough to exert a destabilizing effect; a simple and well-known instance is the lateral loading of an initially compressed bar.

The solutions of the sandwich problem so obtained are necessarily complicated. Prior to their appear-

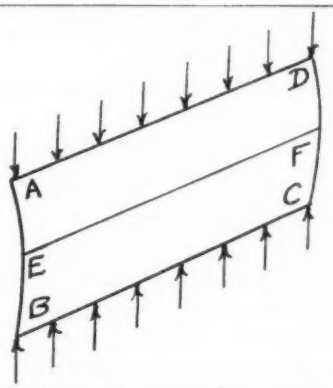

FIG. 1. Cylindrical buckling of a wide plate in compression.

Received February 1, 1951.
* The results reported herein were obtained in the course of research studies supported by the Office of Naval Research (Contract N6-ONR-251-TO-12 with Stanford University).
† Professor of Engineering Mechanics.
‡ Research Assistant.
** Actually a wide strip must *begin* to bend *with* anticlastic curvature, but this curvature does not develop as bending proceeds. There is a transition from E to $E/(1 - \nu^2)$. The critical load for infinitesimal buckling would appear, therefore, not to require the factor $1/(1 - \nu^2)$.
†† See Eq. (11).

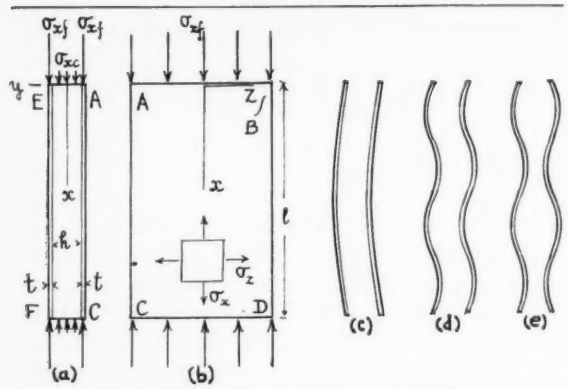

FIG. 2. Sandwich panel in compression. Buckling modes.

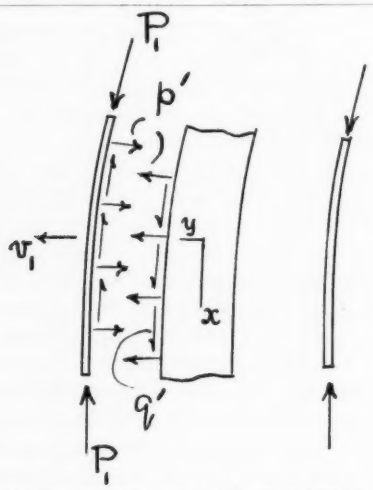

FIG. 3. Reactions between core and faces induced on buckling.

ance, solutions of an approximate character were proposed, having the great advantage of simplicity. However, as with all except the extremely complicated exact theories, the effects of the approximating and simplifying assumptions on the range of validity of the results are not evident, even when attention is entirely confined to the idealized problem of the geometrically and elastically perfect sandwich.

They can be made evident, attention being so confined, by comparison with the exact results. The purpose of this paper is to put forward a conclusion, reached after extensive numerical evaluations of several approximate solutions and one exact solution of the problem. It is that one of the simpler theories, which introduces a simple correction factor to account for the destabilizing effect of the compressive load in the core, is accurate over an extremely wide range of sandwich variables—from extremely thin sheets and extremely deformable cores to thick sheets and cores with moduli comparable to those of the sheets. This range of course includes, but goes far beyond, that of interest in aeronautical construction.

(2) The Corrected Plane-Strain Theory

The simpler theory referred to uses plain-strain equations for the core. It is a modification of the theory of Williams, Leggett, and Hopkins,[5] which in turn is a modification of that of Gough, Elam, and de Bruyne.[1] In both of these papers the core is treated by the equations of plane stress rather than plane strain. Plane stress implies anticlastic curvature in the core when it bends. As indicated previously in this paper, it may not be incorrect to admit such curvature at incipient buckling. However, in the interests of clarity and because the exact theory we use for comparison is in terms of plane strain, it seems preferable to restate concisely the simpler theory in these terms also. The conditions of continuity at the interface between core and face sheets are affected, as well as the equations of the core itself.

We need first an account of the prebuckling state of compression. Let the whole sandwich be compressed vertically, as by a pair of rigid testing machine heads, so that a uniform vertical strain is imposed throughout (Fig. 2, a and b). No forces are applied *horizontally*—on AC or BD—but, if the Poisson's ratios of faces and core are different, the differing tendencies to horizontal expansion will require reconciliation. This is considered to be brought about by some *horizontal* compressive stress in the faces and some tensile stress in the core (or vice versa) in such a ratio that the resultant force per unit run vertically is zero for the faces and core together. Using the subscripts f for the faces and c for the core, this means

$$2t\sigma_{zf} + h\sigma_{zc} = 0, \quad 2t\sigma_{xf} + h\sigma_{xc} = P \tag{1}$$

the notation being indicated on Fig. 2. P is the load per unit run.

Equality of strains in the x- and z-directions means

$$(1/E_f)(\sigma_{xf} - \nu_f\sigma_{zf}) = (1/E_c)(\sigma_{xc} - \nu_c\sigma_{zc}) \tag{2}$$

$$(1/E_f)(\sigma_{zf} - \nu_f\sigma_{xf}) = (1/E_c)(\sigma_{zc} - \nu_c\sigma_{xc}) \tag{3}$$

where E and ν mean Young's modulus and Poisson's ratio, respectively. These four equations determine σ_{xf}, σ_{zf}, σ_{xc}, and σ_{zc}. The ratio of the two vertical stresses is

$$\frac{\sigma_{xf}}{\sigma_{xc}} = \rho\left[\frac{1 - \nu_f\nu_c + 2r\rho(1 - \nu_c^2)}{1 - \nu_f^2 + 2r\rho(1 - \nu_f\nu_c)}\right] \tag{4}$$

where $\rho = E_f/E_c$ and $r = t/h$.

All critical conditions for buckling will be expressed in the form of a critical value for σ_{xf}/E_f. When this is known, σ_{xc} can be found from Eq. (4), and the critical load can be found from Eqs. (1). In the numerical evaluations, we have not attempted to cover a range of values of the Poisson's ratios but have taken $\nu_f = 1/3$ and $\nu_c = 0$ at once.

When buckling occurs, it is assumed that the faces bend into sinusoidal form with one or more half waves in the length (Fig. 2, c, d, and e). For convenience, we suppose at first that the plate is infinitely long vertically and that an arbitrary wave length is imposed. We then inquire what critical stress is required for its maintenance. In an actual panel of finite length, we have to identify the half wave length with the dimension AC, Fig. 2, or with a fraction $1/n$ of it, and select the integer n to give the smallest critical stress. When this integer is 1, the buckling is of the quasi-Euler type. When it exceeds 1, it is usually large, and the buckling is described as wrinkling or crinkling.

The derivation of the "plane-strain formula" for the critical stress in the faces is as follows: The differential equation of the left-hand face sheet in Fig. 3 is

$$D_1 \frac{d^4 v_1}{dx^4} + P_1 \frac{d^2 v_1}{dx^2} + p' - \frac{t}{2}\frac{dq'}{dx} = 0 \qquad (5)$$

which is Eq. (14) of reference 3; v_1 is the deflection, P_1 is the compressive force per unit width in the face only, and p' and q' are core reactions as indicated in Fig. 3.

The sinusoidal plane-strain displacements of appropriate type are

$$\left.\begin{aligned} u &= \{[A_1 + A_2(1/\alpha)(3 - 4\nu_c)] \sinh \alpha y + A_2 y \cosh \alpha y\} \cos \alpha x \\ v &= (A_1 \cosh \alpha y + A_2 y \sinh \alpha y) \sin \alpha y \end{aligned}\right\} \qquad (6)$$

and these are adopted as the displacements in the core. The constants A_1, A_2 have to be related to boundary forces p', q' at $y = \pm h/2$. We find

$$\left.\begin{aligned} p' &= \frac{E_c}{1+\nu_c}\{[\alpha A_1 + (1-2\nu_c)A_2]S + A_2 e_h C\} \sin \alpha x \\ q' &= \frac{E_c}{1+\nu_c}\{[\alpha A_1 + 2(1-\nu_c)A_2]C + A_2 e_h S\} \cos \alpha x \end{aligned}\right\} \qquad (7)$$

where $S = \sinh(\alpha h/2) = \sinh e_h$ and $C = \cosh(\alpha h/2) = \cosh e_h$.

The conditions of continuity between core and face are

$$\left.\begin{aligned} (v)_{y=(h/2)} &= v_1 \\ \frac{t}{2}\frac{d^2 v_1}{dx^2} + \frac{1-\nu_1^2}{E_1}\frac{q'}{\alpha t} &= \left(\frac{\partial u}{\partial x}\right)_{y=(h/2)} \end{aligned}\right\} \qquad (8)$$

corresponding to those adopted and explained in reference 3, Eq. (43). The second equates the tensile strain in the x-direction, in the core and the face, at the junction.

When Eqs. (6) and (7) are inserted in Eq. (5) and the second equation of Eqs. (8), observing the first equation of Eqs. (8), the result is two homogeneous equations in A_1 and A_2, and the condition of consistency yields the critical condition. This reduces to

$$\frac{\sigma_f}{E_f} = \frac{e_t^2}{3(1-\nu_f^2)} + \frac{F + GT + HT^2}{I + JT + KT^2} \qquad (9)$$

where σ_f denotes the critical value of σ_{xf}, and

$$T = \tanh(\alpha h/2) = \tanh e_h = \tanh(e_t/r)$$

(e_h, e_t are defined by $e_h = e_t/r = \alpha h/2$)

$$F = [1 + (1-\nu_c)r]e_t - \frac{1-\nu_f^2}{4(1+\nu_c)\rho e_t}$$

$$G = (1-2\nu_c)r + \frac{(1-\nu_f^2)r}{4(1+\nu_c)\rho e_t^2}$$

$$H = (1-\nu_c)\frac{r}{e_t} - e_t + \frac{1-\nu_f^2}{4(1+\nu_c)\rho e_t}$$

$$I = (1+\nu_c)\rho e_t + (1-\nu_c)(1-\nu_f^2)(r/e_t)$$

$$J = (1+\nu_c)(3-4\nu_c)\rho r$$

$$K = -(1+\nu_c)\rho e_t$$

Eq. (9) is an explicit formula for the critical stress. It is the plane-strain analog of one given by Williams, Leggett, and Hopkins. When r (i.e., t/h), ρ (i.e., E_f/E_c), ν_f, and ν_c are given, Eq. (9) yields σ_f/E_f as a function of e_t, which is $\alpha t/2$ or $\pi t/\lambda$, t being face thickness and λ wave length of buckles.

Curves representing Eq. (9) (with $\nu_f = 1/3$, $\nu_c = 0$) in this manner are shown in Figs. 4a–4g. In Fig. 4f, *two* curves are shown for $r = 0.002$. Eq. (9) is repre-

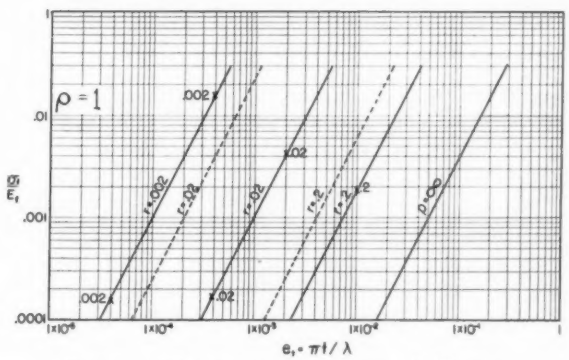

FIG. 4a. Critical stress curves for $\rho = E_f/E_c = 1$.

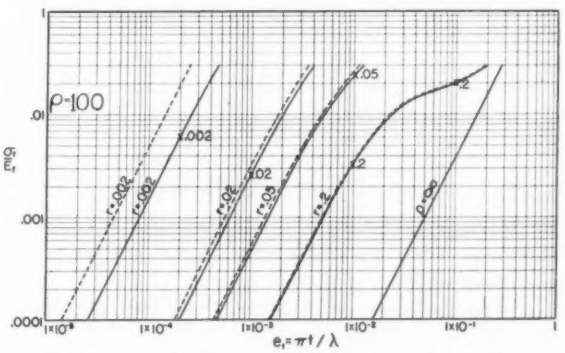

FIG. 4b. Critical stress curves for $\rho = E_f/E_c = 100$.

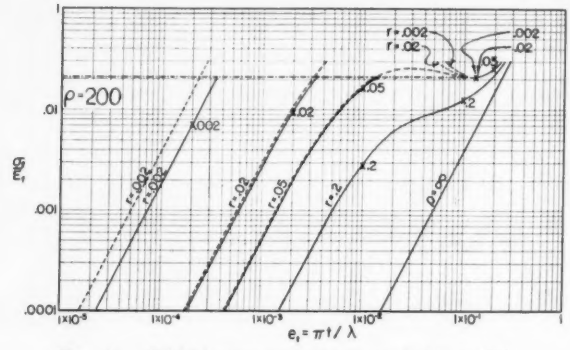

FIG. 4c. Critical stress curves for $\rho = E_f/E_c = 200$.

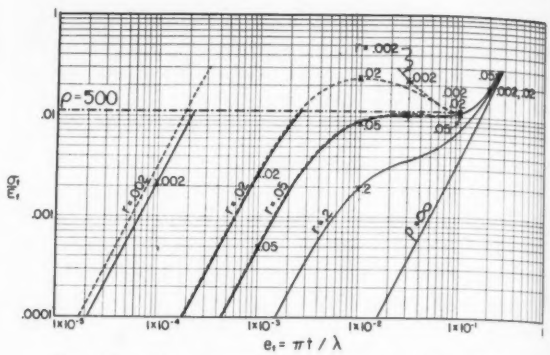

FIG. 4e. Critical stress curves for $\rho = E_f/E_c = 500$.

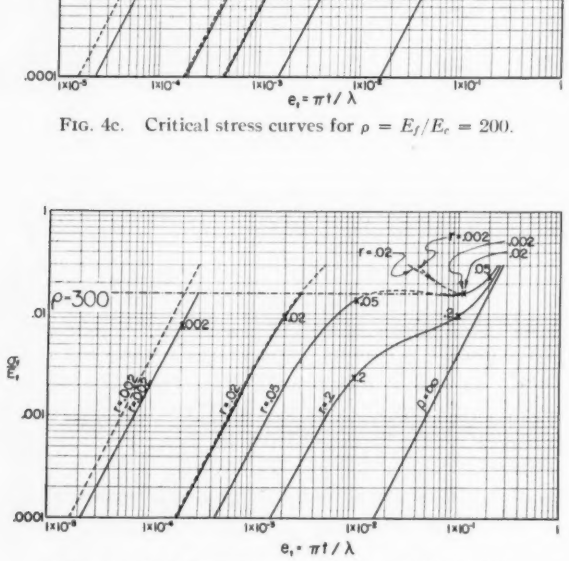

FIG. 4d. Critical stress curves for $\rho = E_f/E_c = 300$.

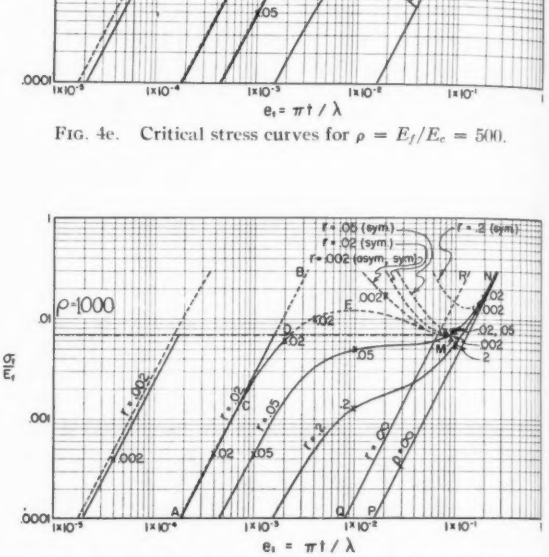

FIG. 4f. Critical stress curves for $\rho = E_f/E_c = 1{,}000$.

sented by the broken line. This prevails wherever two curves (one broken, one solid) appear for one value of r. Otherwise, the solid curve corresponds to Eq. (9).

The crosses appearing on these figures are points calculated from the exact formula specified below. They serve as checks on the accuracy of Eq. (9). It will be observed that these check points lie on the solid curves, not on the broken ones. Thus, the theory just given, resulting in Eq. (9), is found correct only where the broken and solid curves coincide, so that only the latter appears.

The solid curves in Figs. 4a–4g are obtained by applying to Eq. (9) a correcting factor proposed by Williams, Leggett, and Hopkins (reference 5, page 12) to express approximately the destabilizing effect of the compressive stress in the core. This factor, to be applied to the right-hand side of Eq. (9), is

$$1/[1 + (\sigma_{xc}/\sigma_{xf})(h/2t)] \qquad (10)$$

where σ_{xc}, σ_{xf} are the prebuckling stresses in core and faces and their ratio is given by Eq. (4) independently of the stability calculation.

The factor is obtained by considering the compressive force $P_1 = \sigma_{xf}t$ (per unit width) in one face and the compressive force $\sigma_{xc}h/2$ in the half core thickness $h/2$, as indicated in Fig. 5. The effect of the former on the deflection of the face appears in Eq. (5) as the term $P_1(d^2v_1/dx^2)$. The suggestion of Williams, Leggett, and Hopkins was to include the core force with P_1 so that Eq. (5) is changed to

$$D_1 \frac{d^4v_1}{dx^2} + \left(\sigma_{xf}t + \sigma_{xc}\frac{h}{2}\right)\frac{d^2v_1}{dx^2} + p' - \frac{t}{2}\frac{dq'}{dx} = 0 \qquad (5')$$

Since this is the only equation affected and is the only place where P_1 or $\sigma_{xf}t$ appears in the set of Eqs. (5)–(8), the outcome is simply the replacement of σ_{xf} by $\sigma_{xf}[1 + (\sigma_{xc}/\sigma_{xf})(h/2t)]$ in the critical condition (9), where the subscript x in σ_{xf} has been dropped. Thus, the corrected value of σ_f is obtained from Eq. (9) by multiplying the right-hand side by the factor (10).

This procedure implies two assumptions:

(1) The core stress σ_{xc} may be considered to act on the curvature d^2v_1/dx^2 of the face throughout the core thickness. This would be correct for the Euler type of buckling which prevails for long wave lengths.

(2) The corresponding transverse force $\sigma_{xc}(h/2) \times (d^2v_1/dx^2)$ is communicated directly to the face. Actually there will be shear forces in the core which will partially balance this force.

The factor therefore represents an approximation and probably, in view of Eqs. (1) and (2), gives an overcorrection to Eq. (9). In reference 5, the core force $\sigma_{xc}(h/2)$ [see Eq. (5′) above] was multiplied by a coefficient K less than 1 and, of course, not known precisely. We have not included this coefficient—that is, we have taken it as unity—because the curves given by applying (10) to Eq. (9)—the solid curves in Figs. 4a to 4g—show remarkable agreement with the exact check points indicated by the crosses. The crosses lie almost exactly on the curves. This accuracy prevails even for the low values of ρ (= E_f/E_c) of 1, 100, 200, 300 (Figs. 4a–4d), where the correction due to the factor (10) may be several hundred per cent. Thus, Eq. (9) corrected by (10) yields remarkably accurate results over the wide range of ρ from 1 to 10,000 and r from 0.002 to 0.2—that is, ρr between 0.002 and 2,000.

It may be observed that, where the correction is significant, the curves are either straight, indicating Euler buckling with plane sections remaining plane, or nearly straight so that a shear correction is adequate. In particular, the correction factor (10) is not needed for any of the minimum points, such as M in Fig. 4f. It is indicated below that these points give the critical stress for the wrinkling form of buckling. Thus, critical wrinkling stress is not affected by compressive stress in the core.

The factor is merely the ratio of thrust in the faces to the total thrust in the unbuckled state. It is therefore unity and superfluous when the core takes only an insignificant part of the thrust.

With the help of Eq. (4), the factor (10) may be transformed into

$$\frac{2r\rho[1 - \nu_f\nu_c + 2r\rho(1 - \nu_c^2)]}{1 - \nu_f^2 + 4r\rho(1 - \nu_f\nu_c) + 4r^2\rho^2(1 - \nu_c^2)} \qquad (10')$$

and further, with $\nu_c = 0$, $\nu_f = 1/3$, into

$$2r\rho(1 + 2r\rho)/[(1 + 2r\rho)^2 - (1/9)] \qquad (10'')$$

This differs from unity by less than 5 per cent so long as ρr exceeds 10. Thus, the thrust taken by the core and the correction factor can be neglected (with errors less than 5 per cent) if ρr—that is, tE_f/hE_c—exceeds 10.

(3) Interpretation of a Typical Curve

To explain in greater detail the significance of the curves presented, we select as an example the curve marked $r = 0.02$ in Fig. 4f. The plotting is double logarithmic. The sandwich plate to which this curve applies has, since $r = t/h = 0.02$, a core thickness 50 times the face thickness. On Fig. 4f we see that $\rho = 1{,}000$—that is, the Young's modulus of the faces is 1,000 times that of the core. The different curves have different values of r.

The horizontal coordinate e_t, or $\pi t/\lambda$, is π times the ratio of face thickness to wave length of the buckling deformation. Concerning ourselves with the one curve $r = 0.02$, the *left*-hand (small e_t) end of the horizontal axis means *long* wave length; the right-hand end means short wave length. The ordinate σ_f/E_f gives the ratio of the critical compressive stress in the faces, in the direction of load, to the Young's modulus of the faces. Thus, the curve gives the critical stress when the wave length is assigned. The wave length λ for a given length l of plate (Fig. 2b) is $2l$ if the plate buckles in the quasi-Euler manner (Fig. 2c) in one half wave length. If there are several half wave lengths in the length l as in Fig. 2d, λ is $2\ l/n$ where n is the integer number of half wave lengths in l. The appropriate value of n is that which gives the smallest ordinate.

Beginning at the left-hand end of the curve for $r = 0.02$ in Fig. 4f, we observe that the curve rises for a while following a straight line ACB. This corresponds to a simple Euler buckling for long wave lengths, plane sections remaining plane in the bending. The equation for this line (the Euler formula for the composite plate) is

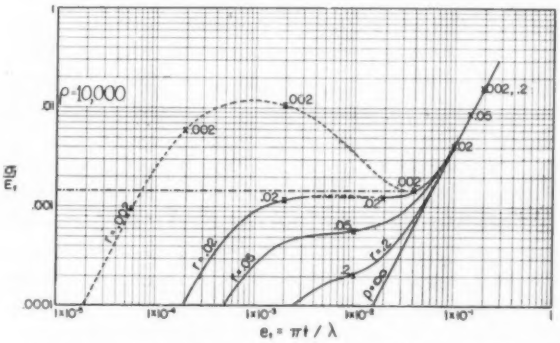

FIG. 4g. Critical stress curves for $\rho = E_f/E_c = 10{,}000$.

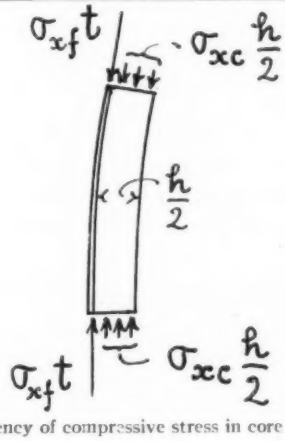

FIG. 5. Tendency of compressive stress in core to deflect face.

$$\frac{\sigma_f}{E_f} = \frac{1 + [2\rho/(1 - \nu_f^2)](3 + 6r + 4r^2)}{1 + 2r\rho[(1 + 2r\rho)/(1 - \nu_f^2 + 2r\rho)]} \left(\frac{1}{3r\rho}\right)(e_t^2) \tag{11}$$

which on log-log paper gives a straight line with slope 2.

Proceeding to the right along the curve, we observe that it begins to droop away from the straight line at C at a wave length corresponding to e_t about 6×10^{-4}. This, at first, can be attributed to additional deformation due to a shear and can be accounted for by a corresponding correction* to the Euler formula [Eq. (11)]. Going further along the curve in Fig. 4f, we find it becomes horizontal (point E). Plots of the shear correction, not reproduced here, show that the range of validity of such a correction reaches but ends at point E, in this instance. Passing the maximum point E, the curve dips to a minimum at M. This occurs at about $e_t = 8 \times 10^{-2}$, or when the half wave length $\lambda/2$ is about 20 times the face thickness t, which would be "wrinkling" or "corrugation" with a considerable number of waves in the length of a plate or panel of practical proportions. A fairly fine adjustment of wave length is then effected by addition or subtraction of one half wave, and, therefore, the wave length of the minimum point can always be closely approached when it is small compared with the plate length l. Accordingly, the part of the curve which lies above the minimum, the broken portion DEM, must be discarded for practical evaluations. This leaves us with the minimum point M itself, corresponding to the wrinkling stress and wave length, together with the left-hand part ACD of the curve, which in this case could be adequately represented by a shear correction to the Euler formula, Eq. (11).

Returning to the minimum point and proceeding to the right, we find the curve rising toward an asymptote. This asymptote, marked PN, represents Euler buckling of the two faces as independent sheets without a core. The approach of our curve, therefore, means that at extremely short wave lengths the core ceases to influence the faces.

The amount that the curve stands above the asymptote PN shows how much the presence of the core increases the critical stress in the faces. On the other hand, the amount that the curve falls below the initial asymptote ABC shows how much the core falls short of compelling the sandwich to bend in the desirable "plane-sections-remain-plane" manner. These comparisons presuppose a common wave length. Two face sheets of length l, without core, will have $\lambda = 2l$. With the core we shall have either $\lambda = 2l$ or a much shorter wave length $\lambda = 2l/n$ corresponding to wrinkling at the minimum point M.

* Several such corrected theories for this "quasi-Euler" range have been proposed (see, for example, references 4–8, 10, and 11). These are based on various simplifying assumptions. and the ranges of validity are not easily defined.

The line QR on Fig. 4f represents the Euler buckling of a monolithic plate of thickness $2t$—that is, the single plate formed by combining the faces with no core between. The critical stress is then four times that of the plate of thickness t represented by PN. Thus, the difference between the curve ACDEMN and QR shows the net effect of using the metal in the form of two faces (plates) separated by a core 50 times as thick as one face ($r = 0.02$). To the left of QR the ordinates of the curve are greater and show the advantage of the core for the corresponding wave lengths.

Again, this immediate comparison is only valid when the sandwich has the same wave length as the monolithic plate—i.e., $\lambda = 2l$—and not when the sandwich wave length is that of wrinkling.

It will be observed that several other curves on Fig. 4f come close to the minimum point M of the curve ACDEMN for $r = 0.02$. One of these other curves (marked ".02 sym.") is valid for the same sandwich but buckling in the symmetrical mode of Fig. 2e. Another is marked ".002 sym. + asym." to indicate that it is valid for both modes for a sandwich having $r = 0.002$. The merging of these curves at point M can be explained by considering first the sandwich with $r = 0.02$—that is, $h/t = 50$—and then an increase in core thickness by a factor of 10, resulting in $r = 0.002$, other things remaining unchanged. The merging shows that this change has not altered the critical stress for wrinkling. The interpretation is that the short wave length results in a deformation in the core which dies out rapidly going in from either face, leaving a middle zone unaffected by the buckling deformation. Increase of core thickness then merely increases this idle zone and makes no difference to the critical stress in the faces. Whether the deformation is asymmetrical as in Fig. 2d or symmetrical as in Fig. 2e is of no consequence, since the two active zones are rendered essentially independent by the idle middle zone. Under these conditions, the wrinkling stress can be found by considering a single face on a semi-infinite core.

Next, examining the curve marked ".05 sym.," we find its minimum a little higher. The value 0.05 for r would represent a thinner core, other things being unchanged, and the higher minimum means that the core deformation in the wrinkling is no longer in two separated layers close to the faces but affects the whole thickness. Each face and the core close to it can no longer be considered as independent and equivalent to a single face on a semi-infinite core. The curve higher up, marked ".2 sym.," shows the same thing to a greater extent. The curve ".2 asym." lies below and has no minimum; therefore, any sandwich for which $r = 0.2$ and $\rho = 1{,}000$ will have no wrinkling mode. It indicates buckling with one half wave in the length l. The same applies to the curve marked ".05" below ACDEMN.

(4) Exact Results

The theory relied on for "exact" results is that of reference 3. This takes into account the destabilizing effect of compressive stress in the core. The paper of reference 2 proceeds from essentially the same basic equations but is more complex in not accepting ordinary plate theory for the faces.

Following Eqs. (26) and (27) on page A-256 of reference 3, it is indicated that the critical stress may be found by solving a transcendental equation. Since this equation is intractable, a different procedure is followed in reference 3, resulting in an explicit but complicated formula for the critical stress. This is Eq. (46c) on page A-260 of reference 3 and is obtained only by neglecting certain terms expected to be small. On evaluation of this formula, indications were encountered that the neglected terms were not, in fact, insignificant over the whole range of practical values. It was therefore necessary to resort to the transcendental equation for exact results. This equation is

$$\frac{\sigma_f}{E_f} = \frac{e_t^2}{3(1-\nu_f^2)} + \frac{e_t^2 + G_1 T + G_2 T_k + kTT_k}{1 - \nu_f^2 + J_1 T + J_2 T_k} \qquad (12)$$

where

$$\left.\begin{aligned} G_1 &= -\frac{(1-\nu_f^2)[1+(1-2\nu_c)s^2]}{4(1-\nu_c^2)\rho s e_t} + \left[\frac{(1-2\nu_c)(1+s)}{2(1-\nu_c)} + \frac{1}{1-\nu_c}\left(\frac{1}{s}\right)\right] e_t \\ G_2 &= \frac{(1-\nu_f^2)k(1+s)^2}{4(1-\nu_c^2)\rho s e_t} + \left\{\frac{(1-2\nu_c)k(1+s)}{2(1-\nu_c)} - \frac{1}{1-\nu_c}\left[\frac{k(1+s)}{s}\right]\right\} e_t \\ T &= \tanh(\pi h/\lambda) \\ T_k &= \tanh k(\pi h/\lambda) \\ J_1 &= \rho e_t \frac{1+\nu_c}{1-\nu_c}\left(\frac{1}{s} + 1 - 2\nu_c\right) \\ J_2 &= -k\rho e_t \frac{1+\nu_c}{1-\nu_c}\left(\frac{1}{s} - 1 + 2\nu_c\right) \\ k &= \sqrt{(1-s)/(1+s)} \end{aligned}\right\} \qquad (13)$$

and s is related to σ_f/E_f by

$$\frac{\sigma_f}{E_f} = \left[\frac{1 - \nu_f\nu_c + 2r\rho(1-\nu_c^2)}{1 - \nu_f^2 + 2r\rho(1-\nu_f\nu_c)}\right]\left(\frac{s}{1+\nu_c}\right) \qquad (14)$$

Here, the special values for ν_f and ν_c ($^1/_3$ and 0) have not yet been inserted, and the notation follows reference 3. The value of σ_f/E_f corresponding to a chosen e_t can be found by trial when ρ and r are given. The "exact" points obtained are shown as crosses (x) on the figures, each labeled with the value of r it belongs to. These crosses are thus check points that serve to show the correctness or incorrectness of curves obtained from less complete but simpler theories. The calculations required for these check points were too heavy to permit the plotting of complete "exact" curves.

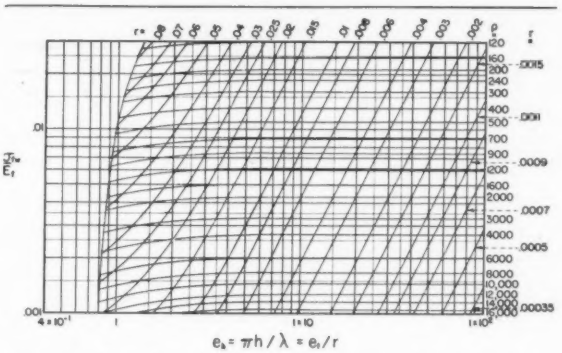

Fig. 6. Chart for critical wrinkling stress and wave length.

(5) A Wrinkling Chart

The wrinkling stress given by a minimum point such as M in Fig. 4f depends on ρ and sometimes also on r. It will be designated by σ_{fw}. It occurs at a definite value of e_t, the abscissa in Figs. 4a–4g. Such a point can be transferred to a diagram such as Fig. 6 with σ_{fw}/E_f as ordinate and $e_h = \pi h/\lambda = re_t$ as abscissa. If other minimum points for the same ρ but different values of r are also obtained and recorded on Fig. 6, the locus of the points is a curve for this value of ρ, along which are points with different values of r attached. We then have one of the curves in Fig. 6 which appear as almost horizontal straight lines, the value of ρ being indicated at its right-hand terminus. The intersecting curves are curves of fixed r, and the values of r are indicated along the top and along the right-hand edge of the diagram. Fig. 6 contains all wrinkling (minimum) points shown in Figs. 4a to 4g with others added (from computations for the minimum only) to complete and refine the chart. Its purpose is to show, by inspection of this one chart, whether wrinkling can occur or not and, if it can, at what stress and wave length. Thus, being given ρ and r, we look for the corresponding curves in Fig. 6 and read off from their intersection point, on the left-hand and base axes, the values of σ_{fw}/E_f and e_h. If there is no intersection—e.g., $\rho = 1{,}000$, $r = 0.05$—no wrinkling (minimum) point exists. This corresponds to the form of the curve for $r = 0.05$ in Fig. 4f; it shows no minimum point. When no wrinkling can occur, the curve of σ_f/E_f versus e_t—that is, the curve of the type shown in Figs. 4a–4g—must be of the general form of those in Fig. 4b or that in Fig. 4g marked $r = 0.05$.

The "horizontal" curves for given ρ in Fig. 6 are truly horizontal except for the slight droop at the left-hand end. Except here, therefore, a change in the value of r moves the wrinkling point horizontally, changing the wave-length-thickness ratio but not the wrinkling stress ratio σ_{fw}/E_f. This corresponds to the

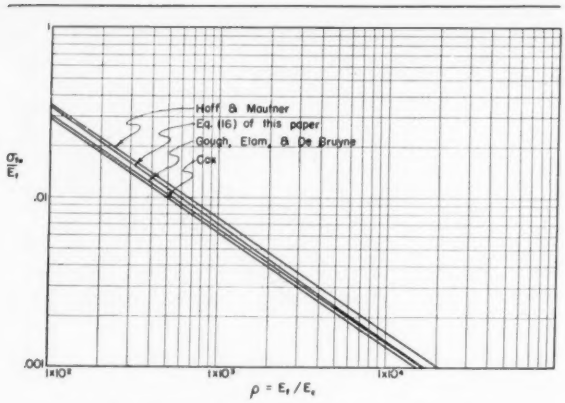

FIG. 7. Several simple wrinkling stress formulas.

independent wrinkling of the two faces on a relatively thick core discussed above. The droop at the left-hand end indicates that, for the corresponding range of r values on any one "horizontal" curve, the core is not so thick that each face can be regarded as a sheet on a core of infinite thickness. For $\rho = 1{,}000$, for instance, the wrinkling of the faces is independent, as though the core were infinitely thick, only when r is less than about 0.025. For larger values of r, the wrinkling stress can fall short of the infinite core value by as much as 15 per cent.

(6) Wrinkling Stress Formulas

On the straight parts of the "horizontal" curves in Fig. 6, the ordinate is independent of e_h and r and, hence, of e_t and r. Thus, for the region covered by these straight parts, σ_{fw}/E_f is dependent on ρ only. A simple formula can be found to cover this region.

Regarding σ_{fu}/E_f, in general, as a function of e_t and r, independence of r means that the core is sufficiently thick to behave as a semi-infinite foundation. This corresponds to putting $T = \tanh e_h = 1$ in Eq. (9). As noticed at the end of Section (2), it is not necessary to consider the correction factor (10). We have then

$$\frac{\sigma_f}{E_f} = \frac{e_t^2}{3(1-\nu_f^2)} + \left[\frac{1 + \dfrac{1-2\nu_c}{1-\nu_c}e_t + e_t^2 + \dfrac{1-\nu_f^2}{4(1-\nu_c)\rho e_t}}{(1-\nu_f^2) + \dfrac{(3-4\nu_c)(1+\nu_c)}{1-\nu_c}\rho e_t}\right] \quad (15)$$

To find the wrinkling stress, we have to minimize this with respect to λ—that is, with respect to e_t. It may first be simplified, however, since examination of the minimum points in Figs. 4a to 4g shows that they occur for ρe_t greater than 50, except where the minimum point is above the practical range for σ_f/E_f (0 to 0.08). This justifies neglect of the last term in the numerator of Eq. (15) and the first term in the second denominator, leaving

$$\frac{\sigma_f}{E_f} = \frac{e_t^2}{3(1-\nu_f^2)} + \left[\frac{1 + \dfrac{1-2\nu_c}{1-\nu_c}e_t + e_t^2}{(3-4\nu_c)\dfrac{1+\nu_c}{1-\nu_c}\rho e_t}\right]$$

or, with $\nu_c = 0$, $\nu_f = 1/3$

$$\frac{\sigma_f}{E_f} = \frac{3}{8}e_t^2 + \frac{1 + e_t + e_t^2}{3\rho e_t}$$

This has a minimum at $e_t = 0.726\rho^{-1/3}$, yielding

$$\frac{\sigma_{fw}}{E_f} = 0.655\rho^{-2/3}\left(1 + \frac{0.51\rho^{1/3} + 0.32}{\rho^{2/3} + 0.39}\right) \quad (16)$$

which can be replaced to a good approximation by

$$\sigma_{fw}/E_f = 0.815\rho^{-0.69}$$

This is shown on Fig. 7.

Several other formulas of this kind, obtained by other approximations and other basic methods, have been proposed. They are as follows, changed from the original notation to the notation of this paper (the distinction between plane strain and plane stress for the core vanishes since we take $\nu_c = 0$):

Gough, Elam, and de Bruyne[1]—

$$\sigma_{fw}/E_f = 0.65\rho^{-2/3}$$

Hoff and Mautner[11]—

$$\sigma_{fw}/E_f = 0.75\rho^{-2/3}$$

(adapted from $\sigma_{cr} = 0.91\sqrt[3]{E_f E_c G_c}$)

Cox[9]—

$$\sigma_{fw}/E_f = 0.62\rho^{-2/3}$$

[adapted from $\sigma_{fw}/E_f = 0.6\rho\sqrt[6]{E_x E_y^3/E_f^4}$ corresponding to Eq. (33d) of reference 9]

All of these formulas are plotted in Fig. 7.

References

[1] Gough, G. S., Elam, C. F., and de Bruyne, N. A., *The Stabilization of a Thin Sheet by a Continuous Supporting Medium*, Journal of The Royal Aeronautical Society, Vol. 44, pp. 12–43 June, 1940.

[2] Neuber, H., *Stablitaetstheorie der Druckbeanspruchten Verbundplatte*, English Translation, Report No. T-TS-964-RE, Wright Field, Ohio, March, 1948.

[3] Goodier, J. N., *Cylindrical Buckling of Sandwich Plates*, Journal of Applied Mechanics, Vol. 13, No. 4, pA-253, December, 1946.

[4] Hoff, N. J., and Mautner, S. F., *Bending and Buckling of Sandwich Beams*, Journal of the Aeronautical Sciences, Vol. 15, No. 12, p. 707, December, 1948.

[5] Williams, D., Leggett, D. M. A., and Hopkins, H. G., *Flat Sandwich Panel Under Compressive End Loads*, A.R.C. Technical Report R. and M., No. 1987, June, 1941.

(*Continued on page 664*)

Allowable Compressive Stresses in Aircraft Structures

B. E. GATEWOOD* AND E. L. WILLIAMS†

U.S.A.F. Institute of Technology and Curtiss-Wright Corporation

SUMMARY

This paper shows procedures for determining the allowable buckling and maximum compressive stresses in both the elastic and plastic regions for structural materials for which compressive stress-strain curves are known. In particular, curves are shown that are applicable for the aluminum and magnesium alloys.

Detail procedures for obtaining the allowable compressive stresses in both the elastic and plastic regions are indicated for the following types of aircraft structure under compressive loads: (1) compressive buckling of flat plates; (2) compressive maximum of flat plates; (3) shear buckling of flat plates; (4) bending buckling of flat plates; (5) column stress for structural elements with stable cross sections (no local buckling); (6) interrivet buckling of flat plates; (7) compressive buckling of formed and extruded sections with local instability; (8) compressive maximum or crippling of formed and extruded sections with local instability; (9) column stress of formed and extruded sections with local instability; (10) bending buckling of formed and extruded sections with local instability; (11) bending maximum of formed and extruded sections with local instability; (12) compressive buckling of flat plates with stiffeners; (13) compressive maximum of flat plates with stiffeners; and (14) column stress of flat plates with stiffeners.

INTRODUCTION

COZZONE AND MELCON[2] discussed the use of nondimensional buckling curves to determine allowable buckling and column stresses for plate elements in aircraft structures. It is the purpose of this paper to extend and modify the procedures of reference 2 to include the latest results on the buckling and failure of plates, formed or extruded sections, and stiffened plates in both the elastic and plastic regions. If the method of reference 3 is extended to stiffened panels and incorporated into the procedure of reference 2, then the maximum stresses (crippling) of many formed and extruded sections, as well as many stiffened panels, can be read directly from curves without having to compute laboriously the stress for each element and take the average of all the elements. For the stiffened panels it is not necessary to compute the effective skin.

To determine the suitability of the curves resulting from the above procedure for analysis of component parts of the aircraft structure, the results of approximately 1,700 tests were compared with values predicted by the curves. The scatter appears to be less than that usually encountered in compression tests of aircraft components.

NONDIMENSIONAL STRESS-STRAIN CURVES

References 6 to 10 show nondimensional stress-strain curves for a large number of stress-strain tests. The curves are made nondimensional by plotting σ/σ_{cy} against eE/σ_{cy}, where σ_{cy} is the yield stress defined by the secant line of slope $0.7E$. There is little variation in the nondimensional curves, even though the dimensional curves vary widely. In fact, if the nondimensional compressive stress-strain curves for 75ST, 24ST, and R301T in references 6 to 10 are plotted together, there is little variation between the alloys.

References 11 and 12 show that these nondimensional stress-strain curves, as well as those for other materials such as steel and magnesium, can be represented by the equation

$$\frac{1}{B^2} = \frac{eE}{\sigma_{cy}} = \frac{\sigma}{\sigma_{cy}}\left[1 + \frac{3}{7}\left(\frac{\sigma}{\sigma_{cy}}\right)^{n-1}\right] \qquad (1)$$

where n is the stress-strain shape parameter given in references 2, 11, and 12 and where B is a parameter for constructing curves. Fig. 6 of reference 11 and Fig. 14 of reference 12 show graphs of Eq. (1) for selected n from 2 to ∞. A study of the average stress strain curves in references 6 to 10 and of Table 1 in reference 2 indicates that almost all of the aluminum alloys ordinarily used in aircraft structures can be approximated by one stress-strain curve: $n = 10$ in Eq. (1). References 13 and 14 also indicate that the magnesium alloy extrusion of J-1 and O-1HTA can be approximated by the same curve, $n = 10$. Some of the extrusions with a high yield point, such as 75ST, have a value of n greater than 10. However, if $n = 10$ is used for them, the results will be conservative up to the yield point; since these materials do not reach much beyond the yield point in elongation, the stress-strain is usually cut off at, or slightly above, the yield point. Fig. 1 shows Eq. (1) for $n = 10$ with the cutoffs marked for alloys with high yield points. For design, the σ_{cy} defined by $0.7E$ is close enough to the usual σ_{cy} defined by the 0.2 per cent offset line so that either can be used. However, in the nondimensional plot, the strain associated with $0.7E$ must be used.

Presented at the Structures Session, Nineteenth Annual Meeting, I.A.S., New York, January 29–February 1, 1951.

* Head, Department of Mechanics, U.S.A.F. Institute of Technology.

† Now, Structures Technologist, Fairchild Aircraft Division, Fairchild Engine and Airplane Corporation.

Nondimensional Buckling Curves

Reference 15 gives a method of calculating the buckling stress of columns and plates in the plastic range by introducing a factor η so that ηE is the effective modulus of elasticity. η depends upon the cross section and length of the section and upon the tangent modulus $E_{\tan}$ and the secant modulus $E_{\sec}$. Since the stress-strain curve as represented by Eq. (1) corresponds to $\eta = E_{\sec}/E$, then the nondimensional buckling equation for any η can be written as

$$\frac{1}{B^2} = \frac{\sigma_{cr}}{\eta\sigma_{cy}} = \frac{E\epsilon_{cr}}{\sigma_{cy}} = \frac{(\sigma_{cr}/\sigma_{cy})[1 + (3/7)(\sigma_{cr}/\sigma_{cy})^{n-1}]}{\eta E/E_{\sec}} \tag{2}$$

where σ_{cr} is the buckling stress. Note that the buckling curve can be obtained for any stress-strain curve, whether the equation is known or not, by dividing the strain by $\eta E/E_{\sec}$.

Reference 15 gives equations for η for plates, flanges, and columns in compression; reference 16 gives η for shear buckling; reference 17 gives η for composite sections; reference 18 gives a comparison of the method of calculating η in reference 15 to other methods of obtaining the buckling curves. Reference 49 gives a method of calculating η different from reference 15, but it does not check tests for plates as well as that of reference 15. It appears from these references that one value of η can be chosen for most plates, formed and extruded sections, and stiffened plates provided they fail by local instability or crippling, while another value can be chosen for columns. These values are approximations, but the theory itself is also an approximation so that the assumption of two values of η for aircraft structures seems justified. In fact, reference 2 uses one value only, $\eta = E_{\tan}/E$, for plates as well as columns; reference 4 uses $\eta = E_{\sec}/E$ for plates. The approximate values selected are

$$\left.\begin{aligned} \eta &= \frac{E_{\sec}}{E}\left(\frac{1}{2} + \frac{1}{2}\sqrt{\frac{1}{4} + \frac{3}{4}\frac{E_{\tan}}{E_{\sec}}}\right) \quad \text{(for plates)} \\ \eta &= E_{\tan}/E \quad \text{(for columns)} \end{aligned}\right\} \tag{3}$$

Reference 48 shows that this value for columns with $n = 10$ is accurate enough for design.

If Eq. (3) be substituted into Eq. (2), then

$$\frac{1}{B^2} = \frac{\sigma_{cr}}{\eta\sigma_{cy}} = \frac{\sigma_{cr}}{\sigma_{cy}}\left[\frac{1 + \frac{3}{7}\left(\frac{\sigma_{cr}}{\sigma_{cy}}\right)^{n-1}}{\frac{1}{2} + \frac{1}{4}\sqrt{1 + 3\frac{E_{\tan}}{E_{\sec}}}}\right] \tag{4}$$

for plates and sections in compression and plates in shear and

$$\frac{1}{B^2} = \frac{\sigma_{cr}}{\eta\sigma_{cy}} = \frac{\sigma_{cr}}{\sigma_{cy}}\left[1 + \frac{3}{7}n\left(\frac{\sigma_{cr}}{\sigma_{cy}}\right)^{n-1}\right] \tag{5}$$

for columns, where

$$\frac{E_{\tan}}{E_{\sec}} = \frac{1 + (3/7)(\sigma_{cr}/\sigma_{cy})^{n-1}}{1 + (3/7)n(\sigma_{cr}/\sigma_{cy})^{n-1}} \tag{6}$$

Eqs. (4) and (5) are plotted on Fig. 1 for $n = 10$.

By using Eqs. (4) and (5), the standard buckling and column equations can be extended to the plastic range

$$\frac{\sigma_{cr}}{\eta\sigma_{cy}} = \left(\frac{KE}{\sigma_{cy}}\right)\left(\frac{t}{b}\right)^2 = \frac{1}{B^2} \tag{7}$$

$$\frac{\sigma_c}{\eta\sigma_{cy}} = \left(\frac{\pi^2 E}{\sigma_{cy}}\right)\left(\frac{\rho}{L'}\right)^2 = \frac{1}{B^2} \tag{8}$$

Thus, the buckling stress, Eq. (7), for any plate, formed or extruded section, or stiffened plate can be read from Fig. 1 provided σ_{cy} of the material is known and K can be obtained. Any column stress can be read if σ_{cy} and L' are known [Eq. (8)]. It should be noted that Johnson's parabola for short columns differs little from the column curve, Eq. (8). In fact, from Eq. (8),

$$\frac{\sigma_c}{\eta\sigma_{cc}} = \frac{1}{4[1 - (\sigma_c/\sigma_{cc})]} = \frac{1}{B^2} \tag{9}$$

For sections that do not fail by local instability (crippling), $\sigma_{cc} = \sigma_{cy}$; otherwise, σ_{cc} is the crippling stress of plates, formed or extruded sections, or stiffened plates. Eq. (9) is shown on Fig. 1.

Paragraph 14.9 of reference 5 discusses the effect of eccentricities on columns for a stress-strain curve with $n = \infty$—that is, the stress is elastic up to a maximum stress at which failure occurs. By use of Eq. (14.39) in reference 5 and Eq. (8) above, one can write

$$\frac{1}{B^2} = \frac{\sigma_c}{\eta\sigma_{cc}} = \frac{\pi^2}{4}\frac{\sigma_c/\sigma_{cc}}{\left\{\cos^{-1}\left[\frac{e}{(\sigma_{cc}/\sigma_c) - 1}\right]\right\}^2} \tag{10}$$

where σ_{cc} is the yield stress σ_{cy}, or the crippling stress σ_{cc}, or some cut-off stress; where e is the eccentricity; and where $a = I/Ac$ with I/c section modulus and A section area. Fig. 1 shows Eq. (10) for several values of e/a.

From reference 2, the formula for interrivet buckling can be written as

$$\frac{\sigma_c}{\eta\sigma_{cy}} = \frac{4\pi^2 E}{\sigma_{cy}}\left(\frac{0.29t}{s}\right)^2 = \frac{1}{B^2} \tag{11}$$

with s as rivet spacing. σ_c/σ_{cy} can be read on Fig. 1 from either Eq. (8) or (9).

It should be noted that the sheet must be formed in the O-condition and heat-treated so that it will have the same σ_{cy} throughout. On basis of references 3, 19, and 20, extrusions have practically the same σ_{cy} throughout. If formed in the T-condition, σ_{cy} will vary, giving a higher stress in the corners than on the flats. The most satisfactory procedure for forming in

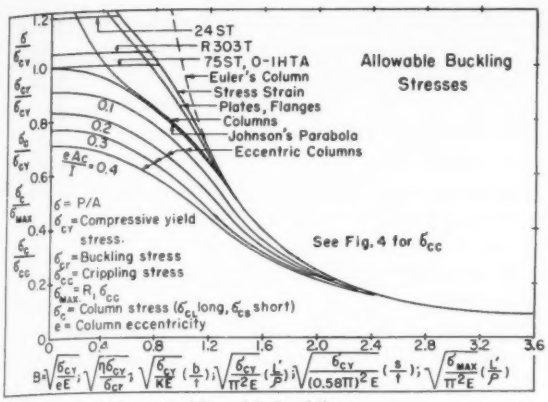

FIG. 1. Allowable buckling stresses.

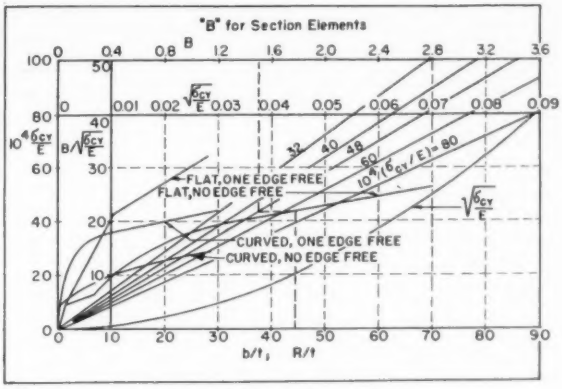

FIG. 3. *B* for section elements.

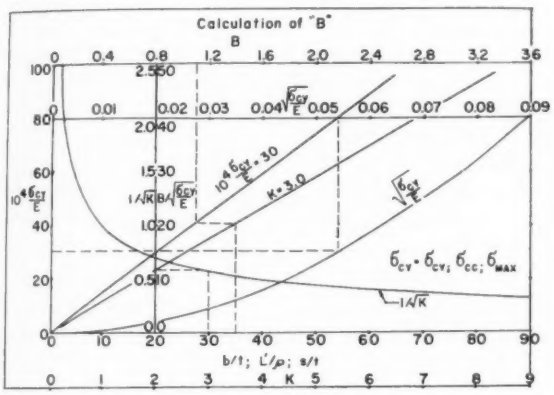

FIG. 2. Calculation of *B*.

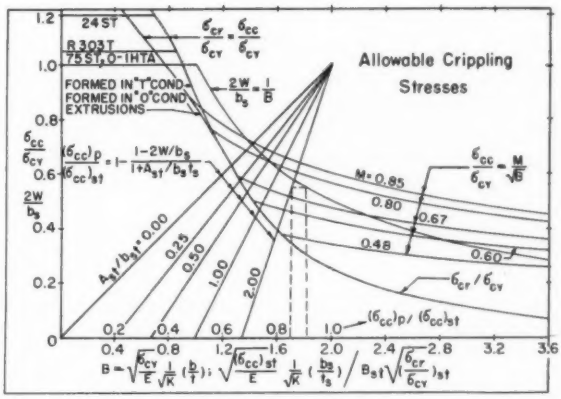

FIG. 4. Allowable crippling stresses.

T-condition is to use the test buckling curve from Fig. 14 of reference 21 for sections formed in the T-condition (see Fig. 4).

K Values for Buckling Stresses

The N.A.C.A. has shown that Eq. (7) can be used for the buckling of formed sections, extruded sections, and stiffened plates. It is only necessary to determine the correct *K* for the section. Then Fig. 1 can be used to obtain the buckling stress. *K* values for different sections can be calculated from data and procedures in references 23, 24, and 25. *K* values for flat plates are given in Fig. 14.25 of reference 5. *K* values for compression of channels and zees are in references 19 and 26. Reference 19 shows *K* for compression for rectangular tubes. *K* for H-sections in compression is in references 19 and 26. Fig. 5 shows *K* for compression of angles as calculated from references 23 and 25. Fig. 6 shows *K* for bending of channels and zees as calculated from references 24 and 25. *K* for buckling of compression panels with Z or T stiffeners is in reference 28.

The N.A.C.A. has made many tests for buckling stresses on formed and extruded sections and for stiffened plates. If these test values are compared with the plate buckling curve in Fig. 1, agreement within the test scatter is obtained. Test buckling values are given in references 13, 19, 20, 21, 31, 32, 33, 27, 35, 36, and 18 for most of the aluminum and magnesium alloys used in aircraft structure.

Maximum Allowable Stresses

The maximum allowable stress or ultimate allowable stress is the allowable crippling stress for local failure of a section and is the allowable column stress for column failure in either the long or short column range. In most cases the allowable crippling stress, which may be higher than the buckling stress because of the fact that the edges and corners of the section may be able to carry higher stresses than the flat elements and which may involve yielding in the corner, must be determined from empirical formulas or curves obtained from tests. Reference 29 gives a theory for flanges which checks test data with little scatter.

On the basis of tests, several procedures have been set up to determine curves that may be used to obtain crippling stresses for design of any type section. Reference 2 gives a procedure of constructing the design

TABLE 1
M Values

b/t of Web	*M* — Formed in T-condition	*M* — Extrusion or formed in O-condition
0–25	0.85	0.80
40	0.75	0.67
75	0.67	0.60

value for any section and material by use of a combination of loads carried by the flat and curved elements of the section. The structures manuals of many aircraft companies give curves based on tests to build up the design values from flat elements only. Reference 3 sets up curves from tests on zees and channels[19,21] for crippling or maximum stress based upon the yield stress and the buckling stress. Reference 4 gives a procedure for the effective area to use on stiffened panels.

The method of reference 3 can be modified and extended by the use of Eqs. (4) and (7) above to give the maximum stress for any section for which K can be obtained. Reference 3 shows that for a certain range of values of σ_{cr} the maximum stress $\sigma_{max.}$ can be expressed in the form

$$\frac{\sigma_{cc}}{\sigma_{cy}} = \frac{\sigma_{max}}{\sigma_{cy}} = M\sqrt[4]{\frac{\sigma_{cr}}{\eta\sigma_{cy}}} = \frac{M}{\sqrt{B}} \qquad (12)$$

where M depends upon the geometry of the section. Fig. 4 shows a plot of Eq. (12) for selected M values. The maximum stress is taken as equal to the buckling stress to the left of the intersection of Eqs. (12) and (4). For zees, channels, and H-sections, the M values as correlated with b/t were taken from Fig. 11 of reference 3 (see Table 1).

For plates use $M = 0.48$. These values may be interpolated on Fig. 4. For other sections, M can be evaluated from several tests or from analogy to the zee and channel sections. For angles in compression, M as correlated to the longer leg of the angle should correspond to about one-third of the b/t for channels or zees (see Fig. 5). For bending of channels and zees, it appears that b/t of the compressed leg should be used, with M being that for a channel or zee with the same b/t. For stiffened panels in compression, the test data of reference 27 indicate that $M = 0.80$ gives suitable results regardless of b/t of the skin (for stiffener sizes used).

For sections for which K is not available, the maximum or crippling stress may be obtained from the elements of the sections as in reference 2. Fig. 3 shows curves for obtaining B for the elements of the section for any alloy. This B is to be used for buckling of the elements on the curve for sections in Figs. 1 or 4. Fig. 3 is constructed from the curves for 24SRT of reference 2 except that buckling for sections in Fig. 1 is used instead of the tangent modulus. A comparison of Figs. 2 and 3 shows that there is no fixed value of K for the elements of the sections as there is for the

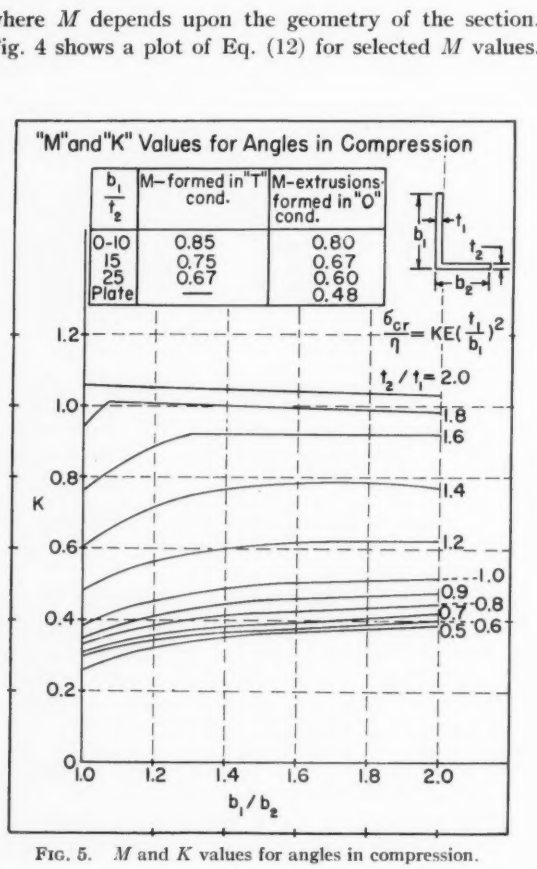

FIG. 5. *M* and *K* values for angles in compression.

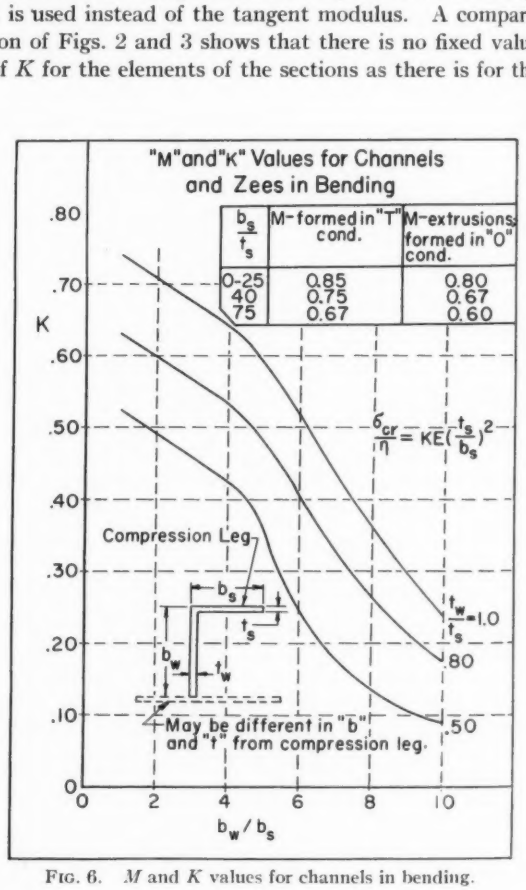

FIG. 6. *M* and *K* values for channels in bending.

section as a whole. This would seem to indicate that Fig. 3 should not be used for sections that differ appreciably from those tested to obtain Fig. 6 of reference 2. Note that any set of test curves for elements of a section for a given alloy may be converted to a form similar to Fig. 3 by using Fig. 1.

Section 14.14 of reference 5 points out that columns subjected to local crippling failure follow approximately Johnson's parabola [Eq. (9)], where σ_{cc} is the crippling stress. Thus, when σ_{cc} is obtained as the maximum stress in Fig. 4 or as the average stress from the elements in Figs. 3 and 1, then it is used to obtain a B for reading the column stress from Johnson's parabola in Fig. 1.

Allowable Maximum Stresses for Stiffened Plates

Because of riveted joints, different σ_{cy} for stiffeners and plates, and eccentricities, the allowable maximum stress for a stiffened panel is more difficult to determine than that for a formed or extruded section. Reference 47 shows the large scatter present in panel tests and shows the effects of the size and spacing of the rivets in reducing the maximum average stress for the panel. Although the curve of reference 47 for the reduction in stress is for stiffened panels that fail by crippling, a few tests at Curtiss-Wright Corporation show a reduction in strength in the column range for stiffened panels. For local instability or crippling of stiffened panels use

$$\sigma_{max.} = R_1\sigma_{cc} \tag{13}$$

with σ_{cc} from Fig. 4 or Eq. (12) and with $M = 0.80$ and R_1 from reference 47. For column action of stiffened panels use the above $\sigma_{max.}$ in place of σ_{cy} in Figs. 1 or 4 and for long column use

$$\frac{\sigma_{cL}}{\sigma_{max.}} = \frac{R_2\pi^2E}{\sigma_{max.}(L'/\rho)^2} = \frac{1}{B^2} \tag{14}$$

For short columns use Johnson's parabola

$$\frac{\sigma_{cS}}{\sigma_{max.}} = 1 - \frac{B^2}{4} = 1 - \frac{1}{4(\sigma_{cL}/\sigma_{max.})} \tag{15}$$

where B is defined in Eq. (14). A few tests indicate R_2 may be about 0.75 for flush rivets and close to 1.00 for round-head rivets closely spaced. It also appears that R_2 depends upon the location of the neutral axis of the panel. If the neutral axis is near the joint of stiffeners to skin, then R_2 is larger than when the neutral axis is near the center of the stiffeners. Let R_{21} be the value of R_2 for neutral axis at skin stiffener joint and let R_{22} be the maximum value of R_2 for the neutral axis near the center of the stiffeners. For the variation from R_{21} to R_{22} use I as calculated for the stiffener about the skin stiffener joint until σ_{cL} reaches the cutoff value given by R_{22}.

There is a further complication in using Eqs. (14) and (15) on stiffened panels tested in a test machine. For panels with large deep unsymmetrical stiffeners closely spaced the neutral axis is not parallel to the plate. This introduces eccentric loading on the end stiffeners. This eccentric loading will cause the panel to fail at stresses below those given by Eqs. (14) and (15) [see Fig. 1 and Eq. (10)].

To obtain σ_{cc} for stiffened panels when K is not known, use can be made of an effective skin area acting with the stiffener. Reference 4 gives the effective width $2w$ in terms of the stiffener crippling stress as

$$\sigma_{st} = KE(t/2w)^2 \tag{16}$$

where K is for the panel. This does not help when K is unknown. Reference 5 recommends the effective width as

$$\sigma_{st} = 2.89E(t/2w)^2 \tag{17}$$

Note that both Eqs. (21) and (22) can be extended to the plastic range by using ηE for E. With η for the effective skin the same as η for the stiffeners Eqs. (16) and (17) can be written as

$$\frac{2w}{b_s} = \sqrt{K}\left(\frac{t_s}{b_s}\right)B_{st}\sqrt{\left(\frac{E}{\sigma_{cy}}\right)_{st}\left(\frac{\sigma_{cr}}{\sigma_{cc}}\right)_{st}} \tag{18}$$

with $B_{st} \geq B_{\text{cutoff}}$ at intersection of σ_{cc} curve and cutoff line in Fig. 4; for $B_{st} \leq B_{\text{cutoff}}$, use B_{cutoff}. Eq. (18) is shown in Fig. 4 against

$$B = \frac{\sqrt{(\sigma_{cc})_{st}/KE}(b_s/t_s)}{B_{st}\sqrt{(\sigma_{cr}/\sigma_{cy})_{st}}}$$

Note that

$$B_{st}\sqrt{(\sigma_{cr}/\sigma_{cy})_{st}} = 1$$

in elastic range and that any stiffener σ_{cc} may be put on Fig. 4 to obtain $(\sigma_{cr})_{st}$ and B_{st}.

To compare values given by Eq. (18) to test values and to values obtained from Eq. (12) or Fig. 4 use

$$\frac{2w}{b_s} = \frac{(\sigma_{cc})_p}{\sigma_{st}}\left(1 + \frac{A_{st}}{b_st_s}\right) - \frac{A_{st}}{b_st_s} \tag{19}$$

where $(\sigma_{cc})_p$ is test value or value from Fig. 4, and A_{st} is stiffener area. Comparisons of values of $2w/b_s$ for several stiffened plates (Z stiffeners in reference 35) as given by Eq. (18) with $K = 2.89$ (Eq. 17), K from reference 4 and K from reference 28, and as given by Eq. (19) with $(\sigma_{cc})_p$ from Fig. 4 and from tests show that Fig. 4 checks the tests better than the other methods. Eq. (18) with K from reference 4 is high [Eq. (16) is also high]; Eq. (18) with $K = 2.89$ is usually low, but, along with Eq. (17), checks well in the elastic region; Eq. (18) with K from reference 28 checks for certain stiffened plates with large b_s/t_s. Hence, use Fig. 4 when K is known, and use Eq. (18) with $K = 2.89$ when K is not known.

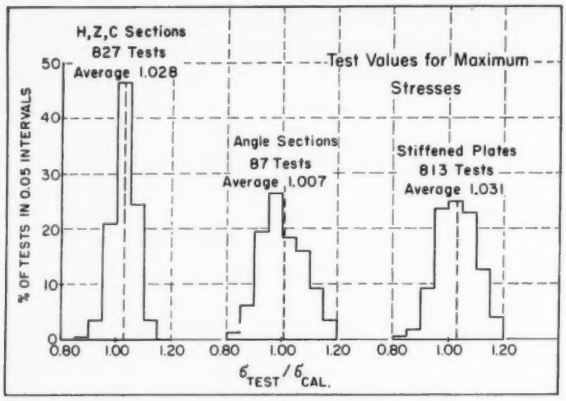

FIG. 7. Test values for maximum stresses.

TEST VALUES FOR MAXIMUM STRESSES

If the K and M be obtained for the section and if the yield stress σ_{cy} is specified, then the buckling stress and maximum local failing stress can be read from Figs. 1 and 4. If the structural element is a long column, use Fig. 1; if the structural element is a short column, use Fig. 1 with σ_{cc} from above in place of σ_{cy}. For stiffened panels use Fig. 4.

Using the above procedure, allowable maximum stresses were calculated for about 1,700 test specimens and were compared to the actual test stresses. Fig. 7 shows the frequency of tests in intervals of 0.05 of $\sigma_{test}/\sigma_{cal.}$ as plotted against $\sigma_{test}/\sigma_{cal.}$. Included in Fig. 7 are the crippling stresses of 827 extruded H-sections, extruded and formed Z-sections, extruded and formed C-sections of 75ST, 24ST, R-303T, O-1HTA magnesium, 14ST, 17ST; [13,19–21,31–33,38,51] the crippling stresses of 87 angle sections of 75ST; [38,39] the maximum stresses of 813 stiffened plates (stiffened by Z's, T's, C's, and angles) of 75ST, 24ST, 14ST, and ZK60A mg.[18,27,34–36,44,50] For the stiffened plates, in Eqs. (13), (14), (15), $R_1 = R_2 = 1.00$ except for the 24ST panels of reference 35; in reference 35, $R_1 = 1.00$, $R_{21} = 0.75$, and $R_{22} = 0.95$. Also, for the panels of reference 36 with deep stiffeners closely spaced, the eccentricity on the end stiffener was used in Fig. 4 for the panels with large L/ρ; for low L/ρ, the amount of eccentricity used was reduced. It should be noted that this problem of eccentricity arises because of the method of testing and ordinarily will not occur on the actual airplane panels.

SUMMARY OF PROCEDURES FOR ANALYSIS

In conclusion, the procedures for compressive allowables for different types of aircraft structure that have been discussed above may be summarized as follows:

(*1*) *Compressive Buckling of Flat Plates.*—Use plate curve in Fig. 1 with

$$B = \sqrt{\sigma_{cy}/KE}(b/t)$$

(K on page 372 of reference 5). For $L/b > 2$, $K = 0.385$ for one edge free, 3.62 for simple support, and 6.35 for clamped edges.

(*2*) *Compressive Maximum of Flat Plates.*—Use Fig. 4 with $M = 0.48$; B and K as for compressive buckling.

(*3*) *Shear Buckling of Flat Plates.*—Use σ_{sy} instead of σ_{cy} (for aluminum alloys can approximate σ_{sy} as $0.6\ \sigma_{cy}$) in procedure for compressive buckling (b being smaller dimension of the plate) with K for shear on page 394 of reference 5. For $L/b > 4$, $K = 4.9$ for simple support and 8.0 for clamped edges.

(*4*) *Bending Buckling of Flat Plates.*—Use same procedure as for compressive buckling with K for bending on page 395 of reference 5. For $L/b > 0.6$, $K = 21.6$.

(*5*) *Column Stress for Sections with Stable Cross Sections.*—Use Euler's column and Johnson's parabola, or eAc/I curves for eccentric loading, in Fig. 1 with

$$B = \sqrt{\sigma_{cy}/E}(1/\pi)(L'/\rho)$$

(*6*) *Interrivet Buckling of Flat Plates.*—Use Euler's column and Johnson's parabola in Fig. 1 with

$$B = \sqrt{\sigma_{cy}/E}(1.72/\pi)(s/t)$$

(*7*) *Compressive Buckling of Sections with Local Instability.*—Use plate curve in Fig. 1 with

$$B = \sqrt{\sigma_{cy}/KE}(b/t)$$

K in Fig. 5 and references 19 and 26.

(*8*) *Compressive Maximum or Crippling of Sections with Local Instability.*—Use Fig. 4 with M from Fig. 5 and from Table 1. If K is not known, use Fig. 3 to obtain B for each element of the section; use each B on the plate curve of Fig. 1 to obtain the stress for the element; average all elements ($\sum \sigma A/A$) to obtain σ_{cc} for the section.

(*9*) *Column Stress of Sections with Local Instability.*—Use Euler's column and Johnson's parabola, or eAc/I curves for eccentric loading, in Fig. 1 with

$$B = \sqrt{\sigma_{cc}/E}(1/\pi)(L'/\rho)$$

σ_{cc} = crippling stress from item (8) above.

(*10*) *Bending Buckling of Sections with Local Instability.*—Use plate curve in Fig. 1 with

$$B = \sqrt{\sigma_{cy}/KE}(b/t)$$

K in Fig. 6.

(*11*) *Bending Maximum or Crippling of Sections with Local Instability.*—Use Fig. 4 with M from Fig. 6. If K is not known, use Fig. 3 on selected (?) elements of the section and proceed as for compressive crippling in item (8) above. If the section has lateral instability then the above value must be reduced.

(12) *Compressive Buckling of Stiffened Plates.*—Use plate curve in Fig. 1 with

$$B = \sqrt{\sigma_{cy}/KE}(b/t)$$

K in reference 28.

(13) *Compressive Maximum of Stiffened Plates.*—Use Fig. 4 with $M = 0.80$. If K for stiffened plate is not known or is not applicable, obtain σ_{cc} for the stiffeners as described in items (7) and (8) above and read the effective skin $2w/b_s$ acting with the stiffener from Fig. 4 with

$$B = \frac{\sqrt{(\sigma_{cc})_{st}/KE}(b_s/t_s)}{B_{st}\sqrt{(\sigma_{cr}/\sigma_{cy})_{st}}}$$

where $K = 2.89$ for middle stiffener* and $K = 1.44$ for end stiffener (pages 374 and 375 of reference 5). Then

$$\frac{(\sigma_{cc})_p}{(\sigma_{cc})_{st}} = 1 - \frac{1 - (2w/b_s)}{1 + (A_{st}/b_s t_s)}$$

which is shown in Fig. 4 with $A_{st}/b_s t_s$ as parameter. $\sigma_{max.}$ for panel is $R_1\sigma_{cc}$, where R_1 is rivet factor.

(14) *Column Stress of Stiffened Plates.*—Use Euler's column and Johnson's parabola, or eAc/I curves for eccentric loading, in Fig. 1 with

$$B = \sqrt{\frac{\sigma_{max.}}{R_2 E}}\frac{1}{\pi}\left(\frac{L'}{\rho}\right)$$

R_2 = rivet factor.

References

[1] ANC-5a, *Strength of Aircraft Elements*, Army-Navy-Civil Committee on Aircraft Design Criteria, U.S. Government Printing Office, Washington, D.C.

[2] Cozzone, F. P., and Melcon, M. A., *Nondimensional Buckling Curves—Their Development and Application*, Journal of the Aeronautical Sciences, Vol. 13, No. 10, pp. 511–517, October, 1946.

[3] Schuette, E. H., *Observations on the Maximum Average Stress of Flat Plates Buckled in Edge Compression*, N.A.C.A. T.N. No. 1625, February, 1949.

[4] Gerard, G. *Effective Width of Elastically Supported Flat Plates*, Journal of the Aeronautical Sciences, Vol. 13, No. 10, pp. 518–524, October, 1946.

[5] Peery, D. J., *Aircraft Structures*, Chapt. 14; McGraw-Hill Book Company, Inc., New York, 1950.

[6] Miller, James A., *Stress-Strain and Elongation Graphs for Aluminum Alloy R301 Sheet*, N.A.C.A. T.N. No. 1010, February, 1946.

[7] Miller, J. A., *Stress-Strain and Elongation Graphs for Alclad Aluminum Alloy 75ST Sheet*, N.A.C.A. T.N. No. 1385, November, 1947.

[8] Miller, J. A., *Stress-Strain and Elongation Graphs for Alclad Aluminum Alloy 24ST Sheet*, N.A.C.A. T.N. No. 1512, May, 1948.

[9] Miller, James A., *Stress-Strain and Elongation Graphs for Alclad Aluminum Alloy 24S-T81 Sheet*, N.A.C.A. T.N No. 1513, May, 1948.

[10] Miller, James A., *Stress-Strain and Elongation Graphs for Aluminum-Alloy 75S-T6 Sheet*, N.A.C.A. T.N. No. 2085, April, 1950.

[11] Ramberg, Walter, and Osgood, W. R., *Description of Stress-Strain Curves by Three Parameters*, N.A.C.A. T.N. No. 902, July, 1943.

[12] Ramberg, Walter, and Miller, J. A., *Determination and Presentation of Compressive Stress-Strain Data for Thin Sheet Metal*, Journal of the Aeronautical Sciences, Vol. 13, No. 11, pp. 569–580, November, 1946.

[13] Heimerl, G. J., and Niles, D. E., *Column and Plate Compressive Strengths of Aircraft Structural Materials—Extruded O-1HTA Magnesium Alloy*, N.A.C.A. T.N. No. 1156, January, 1947.

[14] Atchison, C. S., and Miller, J. A., *Tensile and Compressive Tests of Magnesium Alloy J-1 Sheet*, N.A.C.A. T.N. No. 913, December, 1943.

[15] Stowell, E. Z., *A Unified Theory of Plastic Buckling of Columns and Plates*, N.A.C.A. T.R. No. 898, April, 1948.

[16] Stowell, E. Z., *Critical Shear Stress of an Infinitely Long Plate in the Plastic Region*, N.A.C.A. T.N. No. 1681, August, 1948.

[17] Stowell, E. Z., and Pride, R. A., *Plastic Buckling of Extruded Composite Sections in Compression*, N.A.C.A. T.N. No. 1971, October, 1949.

[18] Heimerl, G. J., and Pride, R. A., *Plastic Buckling of Simply Supported Compressed Plates*, N.A.C.A. T.N. No. 1817, April, 1949.

[19] Heimerl, G. J., and Roy, J. A., *Column and Plate Compressive Strengths of Aircraft Structural Materials, Extruded 75ST Aluminum Alloy*, N.A.C.A. A.R.R. L5F08a, July, 1945 (W.R. L-173).

[20] Heimerl, G. J., and Fay, D. P., *Column and Plate Compressive Strengths of Aircraft Structural Materials, Extruded R303T Aluminum Alloy*, N.A.C.A. A.R.R. L5H04, October, 1945 (W.R. L-33).

[21] Lundquist, E. E., Schuette, E. H., Heimerl, G. J., and Roy, J. A., *Column and Plate Compressive Strengths of Aircraft Structural Materials, 24ST Aluminum Alloy Sheet*, N.A.C.A. A.R.R. L5F01, June, 1945 (W.R. L-190).

[22] Heimerl, G. J., and Woods, W., *Effect of Brake Forming on the Strength of 24ST Aluminum Alloy Sheet*, N.A.C.A. T.N. No. 1072, May, 1946.

[23] Lundquist, E. E., Stowell, E. Z., and Schuette, E. H., *Principles of Moment Distribution Applied to Stability of Structures Composed of Bars and Plates*, N.A.C.A. Report No. 809, 1945 (A.R.R. 3K06, W.R. L-326).

[24] Schuette, E. H., and McCulloch, J. C., *Charts for Minimum Weight Design of Multiweb Wings in Bending*, N.A.C.A. T.N. No. 1323, June, 1947.

[25] Kroll, W. D., *Tables of Stiffness and Carry-Over Factor for Flat Rectangular Plates Under Compression*, N.A.C.A. A.R.R. No. 3K27, November, 1943 (W.R. L-398).

[26] Kroll, W. D., Fisher, G. P., and Heimerl, G. J, *Charts for Calculation of the Critical Stress for Local Instability of Columns with I-, Z-, Channel, and Rectangular-Tube Section*, N.A.C.A. A.R.R. 3K04, November, 1943.

[27] Gallaher, G. L., and Boughan, R. B., *A Method of Calculating the Compressive Strength of Z-Stiffened Panels that Develop Local Instability*, N.A.C.A. T.N. No. 1482, November, 1947.

[28] Boughan, R. B., and Baab, G. W., *Charts for Calculation of the Critical Compressive Stress for Local Instability of Idealized Web- and T-Stiffened Panels*, N.A.C.A. A.R.R. L4H29, August, 1944 (W.R. L-204).

[29] Stowell, E. Z., *Compressive Strength of Flanges*, N.A.C.A. T.N. No. 2020, January, 1950.

[30] Heimerl, G. J., *Determination of Plate Compressive Strengths*, N.A.C.A. T.N. No. 1480, December, 1947.

* Note that $B_{st}\sqrt{(\sigma_{cr}/\sigma_{cy})_{st}} = 1$ in elastic range and that any stiffener σ_{cc}/σ_{cy} may be put in Fig. 4 to obtain stiffener σ_{cr}/σ_{cy} and stiffener B

[31] Heimerl, G. J., and Roy, J. A., *Column and Plate Compressive Strengths of Aircraft Structural Materials—17ST Aluminum Alloy Sheet*, N.A.C.A. A.R.R. L5F08, 1945 (W.R. L-20).

[32] Heimerl, G. J., and Roy, J. A., *Column and Plate Compressive Strengths of Aircraft Structural Materials—Extruded 24ST Aluminum Alloy*, N.A.C.A. A.R.R. L5F08b, 1945 (W.R. L-32).

[33] Heimerl, G. J., and Niles, D. E., *Column and Plate Compressive Strengths of Aircraft Structural Materials—Extruded 14ST Aluminum Alloy*, N.A.C.A. A.R.R. L6C19, 1946 (W.R. L-284).

[34] Dow, N. F., and Hickman, W. A., *Structural Evaluation of an Extruded Magnesium Alloy T-Stiffened Panel*, N.A.C.A. T.N. No. 1518, February, 1948.

[35] Rossman, C. A., Bartone, L. M., and Dobrowski, C. V., *Compressive Strengths of Flat Panels with Z-Section Stiffeners*, N.A.C.A. A.R.R. 4B03, February, 1944 (W.R. L-499).

[36] Hickman, W. A., and Dow, N. F., *Data on the Compressive Strength of 75S-T6 Aluminum Alloy Flat Panels with Longitudinal Extruded Z-Section Stiffeners*, N.A.C.A. T.N. No. 1829, March, 1949.

[37] Kotanchik, J. N., Weinberger, R. A., Zender, G. W., and Neff, J., *Compressive Strength of Flat Panels with Z- and Hat-Section Stiffeners*, N.A.C.A. A.R.R. L4F01, June, 1944 (W.R. L-62).

[38] Kinne, G. B., *Compressive Tests on XB75ST Formed and Extruded Shapes*, McDonnell Aircraft Corporation, Report T-53, June, 1945.

[39] Unpublished tests made by Curtiss-Wright Corporation, Columbus, Ohio.

[40] Newton, R. E., *Bending Strength of Formed Sheet Metal Channels*, Curtiss-Wright (St. Louis) Report No. R-162, February, 1945.

[41] Charleville, J., *Bending Tests of 0.032 24ST Alclad Formed Channels*, Curtiss-Wright (St. Louis) Report No. T-19, December, 1944.

[42] Heimerl, G. J. and Roy, J. A., *Determination of Desirable Lengths of Zee and Channel Section Columns for Local Instability Tests*, N.A.C.A. R.B. L4H10, October, 1944 (W.R. L-180).

[43] Heimerl, G. J., and Roy, J. A., *The Effect of Angle of Bend Between Plate Elements on the Local Instability of Formed Z-Sections*, N.A.C.A. R.B. L4126, September, 1944 (W.R. L-268).

[44] Schuette, E. H., *Charts for the Minimum-Weight Design of 24S-T Aluminum Alloy Flat Compression Panels with Longitudinal Z-Section Stiffeners*, N.A.C.A. A.R.R. L5F15, August, 1945 (W.R. L-197).

[45] Dow, N. F. and Keevil, A. S., *Direct-Reading Design Charts for 24S-T Aluminum Alloy Flat Compression Panels Having Longitudinal Formed Z-Section Stiffeners*, N.A.C.A. T.N. No. 1778, January, 1949.

[46] Schuette, E. H., *Column Curves for Magnesium Alloy Sheet*, Journal of the Aeronautical Sciences, Vol. 16, No. 5, pp. 301–305, May, 1949.

[47] Dow, N. F., and Hickman, W. H., *Effect of Variation in Rivet Diameter and Pitch on the Average Stress at Maximum Load for 24S-T3 and 75S-T6 Aluminum Alloy, Flat, Z-Stiffened Panels That Fail by Local Instability*, N.A.C.A. T.N. No. 2139, July, 1950.

[48] Duberg, J. E., and Wilder III, T. W., *Column Behavior in the Plastic Stress Range*, Journal of the Aeronautical Sciences, Vol. 17, No. 6, pp. 323–327, June, 1950.

[49] Pearson, C. E., *Bifurcation Criteria and Plastic Buckling of Plates and Columns*, Journal of the Aeronautical Sciences, Vol. 17, No. 7, pp. 417–424, July, 1950.

[50] Goran, L. A., *A Comparison of Available Methods for Predicting Crippling Stresses with Test Data*, McDonnell Aircraft Corporation Report No. 697, October, 1947.

[51] Unpublished tests made in U.S.A.F.I.T. materials testing laboratory.

The Evaluation of Theoretical Critical Compression in Sandwich Plates

(*Continued from page 656*)

[6] Troxell, W. W., and Engel, H. C., *Column Characteristics of Sandwich Panels Having Honeycomb Cores*, Journal of the Aeronautical Sciences, Vol. 14, No. 7, p. 413, July, 1947.

[7] March, H. W., *Effects of Shear Deformation in the Core of a Flat Rectangular Sandwich Panel*, Forest Products Laboratory, Publication No. 1583, May, 1948.

[8] Bijlaard, P. P., *On the Elastic Stability of Sandwich Plates I and II*, Proc. Royal Netherlands Academy of Science, Vol. L., 1947.

[9] Cox, H. L., and Riddell, J. R., *Sandwich Construction and Core Materials III. Instability of Sandwich Struts and Beams*, A.R.C. Technical Report R. and M. No. 2125, December, 1945.

[10] Flügge, W., and Marguerre, K., *Théorie de la Stabilité en Compression de la Plaque Sandwich*, Rapp. No. 421-R1-01/10-OR de l'O.N.E.R.A., October, 1947.

[11] Hoff, N. J., and Mautner, S. F., *The Buckling of Sandwich Type Panels*, Journal of the Aeronautical Sciences, Vol. 12, No. 3, p. 285, July, 1945.

Summary of Recent Experimental Investigations in the N.O.L. Hyperballistics Wind Tunnel*

PETER P. WEGENER†

U.S. Naval Ordnance Laboratory

SUMMARY

The N.O.L. 12- by 12-cm. continuous blow-down hyperballistics wind tunnel is briefly described. Limitations of present supersonic wind-tunnel techniques as applied to hypersonic wind tunnels are discussed. Measurements of pressures in the nozzle show that air condensation occurs if flow pressure and temperature fall below the saturation line of air. This condensation can be eliminated by preheating the supply air of the wind tunnel. Tentative experimental criteria on minimum supply temperatures to minimize air-condensation effects on the flow in the test section are given. The highest Mach Number achieved to date at N.O.L. on this basis is 8.25. The effects of air condensation on various standard measurement methods for the determination of Mach Number are given. It is found that only static-pressure and shock-angle measurements are sensitive to air liquefaction effects. Results of a thermodynamic treatment of the condensation process are presented. Finally, some measurements on boundary layers and possible flow separation at high Mach Numbers are given.

INTRODUCTION

RECENT YEARS HAVE WITNESSED a rapid increase in speed of supersonic aircraft, missiles, and projectiles. In order to stay one step ahead of these developments, research and development facilities to provide basic aerodynamic information on bodies moving at hypersonic Mach Numbers are required. One such facility is the hypersonic wind tunnel, where the word "hypersonic" is used here loosely to describe the Mach Number range above 5. Producing hypersonic flows suitable for model testing entails difficulties uncommon to conventional supersonic wind tunnels. To explore these new problems, a 12- by 12-cm. hyperballistics tunnel to study hypersonic flows under a wide range of Mach Numbers, temperatures, and pressures was designed and put into operation in May, 1950, at the Naval Ordnance Laboratory. The research program presently being carried out in this facility primarily concerns physical problems such as air condensation, Mach Number determination, effect of temperature on tunnel operation, boundary layers, and instrumentation.

This paper summarizes some of the observations made so far; sample data characteristic of particular phenomena occurring in the tunnel are given.

APPARATUS AND OPERATIONAL PROBLEMS

The N.O.L. 12- by 12-cm. hyperballistics tunnel and some of its auxiliary components are shown in Fig. 1. Filtered dry air (dew point −50°C. or better) is stored in tanks at 3,000 lbs. per sq.in. pressure. This air is bled via pressure-reducing valves into a settling tank on top of the vertical working section. The supply pressure of the tunnel (up to 8 atmospheres for the investigations to be described) is held constant during

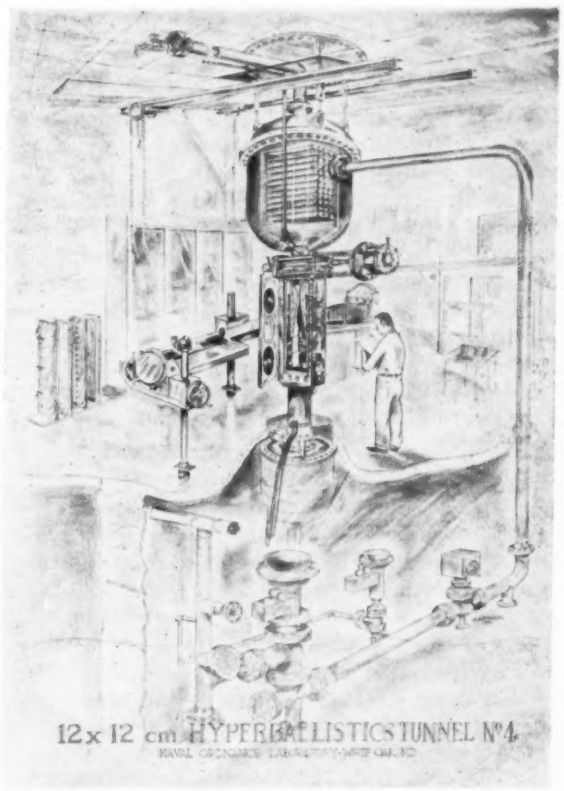

FIG. 1. Artist's sketch of the N.O.L. 12- by 12-cm. hyperballistic wind tunnel.

Presented at the Hypersonic Aerodynamics Session, Nineteenth Annual Meeting, I.A.S., New York, January 29–February 1, 1951.

* The work presented here represents the joint effort of Messrs. E. Stollenwerk, S. Reed, G. Lundquist, and H. Staab of this laboratory.

† Chief, Hyperballistics, Subdivision III.

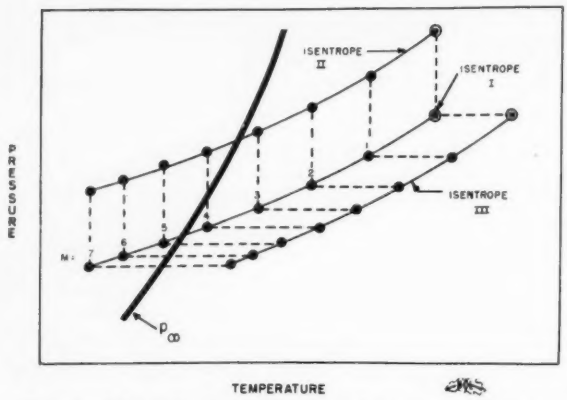

FIG. 2. Schematic expansions beyond air saturation line.

the run. The supply air also passes through an electric heater (80 kw.) located in the settling tank. Automatic power regulation controls the heating of the supply air at any value from room temperature to 500°C. during the run. Then the air flows from top to bottom through the vertical working section into vacuum pumps via a 2,000 cu.m. vacuum sphere common to all the N.O.L. tunnels. The opening of a fast-acting slide valve between settling tank and working section initiates the runs. Pressure ratios up to 50,000 across this valve are available. The hypersonic flow is established in a simple nozzle with arbitrary curvature at the throat and two 50-cm. long plane diverging walls, ending in a square area of 12 by 12 cm. By means of setscrews the area ratio of this nozzle can be adjusted before the run to an arbitrary Mach Number setting M_s. The useful operating range is $M_s = 4$ to 11. After a short parallel-wall section, the air enters a simple diffuser. Since supply air-mass available and vacuum capacity exceed the tunnel requirements, the operation of the tunnel is continuous.

Some of the operational problems occurring with this tunnel are the following: If the tunnel operates at high supply temperatures, the nozzle throat gradually closes because of the heating of the nozzle walls. M_s is extremely sensitive to small throat-area changes at high Mach Numbers. Before and after each run the throat distance is measured with feeler gages, and M_s is interpolated linearly with respect to time between these two points. Knowing the time at which a particular measurement is made in the test section, it can then be approximately related to the actual M_s. Glass windows are also heated gradually from the inside out, causing distortion of optical images. In addition, the schlieren system is pushed to its limit of sensitivity because of the low density in the test section at high Mach Numbers. The same is true for conventional pressure instrumentation, and oil, as well as McLeod, manometers must be used. All tunnel components must resist high temperatures, necessitating the use of copper tubing instead of rubber, silicone rubber gaskets, and heat-resistant paints. Since the working section has no cooling system, the time history of data taking becomes important in contrast to supersonic wind-tunnel techniques.

On Air Condensation

Fig. 2 shows schematic wind-tunnel isentropes of air. Pressure and temperature drop with increasing Mach Number. Isentrope I of this figure intersects the vapor-pressure curve of air[1] at some point; we will call the Mach Number at this intersection "M_c, the Mach Number of equilibrium condensation." Here the danger of air liquefaction commences. An increase in supply pressure (isentrope II) decreases M_c, and an increase in supply temperature (isentrope III) increases M_c. We will call that supply temperature that maintains the air in the test section just at M_c, or saturation, T_{0c}. For example, at $M_c = 10$ and $p_0 = 100$ atmospheres, $T_{0c} = 700$°C. Tunnel operation at such temperatures and pressures results in a number of technical difficulties. On the other hand, calculations based on Becker, Doering, and Volmer's theory of nucleation[2] predicted extensive supersaturations of air, thus lowering the minimum supply temperature for successful tunnel operation at high Mach Numbers. This conclusion was in agreement with experimental experience on water vapor in the air of supersonic wind tunnels, where large supercoolings can be observed. In fact, if the temperature gradient in the nozzle is high, as is the case in hypersonic tunnels, water vapor could be supercooled up to 100°C. before condensing spontaneously.[3] However, experiments with air do not show this supersaturation. C. H. McLellan demonstrated first that air condensation in hypersonic tunnels begins near the saturation point.[4] This fact was also borne out by the investigation described here, as well as those by Stever[5] and by Nagamatsu.[6]

Pressure Measurements with and Without Air Condensation

Table 1 gives a collection of data for different M_s measured at the nozzle exit at supply temperatures of the order of room temperature, called "cold runs." Pitot pressure (p_0') and static pressure (p) are measured and divided by the supply pressure (p_0). The corresponding Mach Numbers are found in an isentropic flow table;[7] they are also determined directly from the Rayleigh pitot-tube formula[8] (p_0'/p). These measured "cold run" Mach Numbers are in disagreement. The pitot Mach Number is somewhat lower than M_s, as expected from the presence of the boundary layer. However, the static-pressure Mach Numbers and, in particular, those from the Rayleigh formula are considerably lower. This conventional evaluation assumes the isentropic expansion of a perfect gas in the nozzle, an assumption that is not true if a part of the air liquefies. Therefore, the discrepancy in formal M

evaluations from pitot and static pressure measurements may be regarded as an arbitrary measure of the magnitude of the air-condensation effects. The latter increase with increasing M_s. These cold-run data are in agreement with those given by Nagamatsu for the C.I.T. hypersonic tunnel, which is nearly the same size as the one at N.O.L.[6]

Fig. 3 shows dimensionless static pressure measured at various distances on the centerline of the nozzle wall. Such data are given for a "cold run" and for a "hot run." In the latter case the supply temperature was raised to the order T_{0c}. Cold-run and hot-run static pressures diverge in the vicinity of the air saturation point in the nozzle of the cold run, with the hot-run static pressures being lower at the nozzle end. The triangles in Fig. 3 show the results for a cold run, where the ratio of supply density to atmospheric density ($\rho_0/\rho_{atm.}$) is equal to that for the hot run in order to minimize Reynolds effects. (Reynolds Number itself is a dubious parameter if liquefaction sets in.) Because both the low- and high-density cold-run static pressures are nearly equal, the discrepancy between cold runs and hot runs cannot be attributed to a difference in boundary-layer thicknesses for the cold and hot case.

Fig. 4 shows "formal" Mach Number determinations by use of isentropic-flow tables from pitot and static pressure measurements at the nozzle exit as a function of supply temperature. Four different Mach Number settings are shown. Only when T_0 nears T_{0c}, does agreement of the Mach Number derivation from pitot and static pressure measurements become apparent. The pitot pressure is nearly insensitive to liquefaction effects throughout the range of test temperatures, while static pressure changes considerably with supply temperature, as shown by the derived M on Fig. 4. The change of M_s during the runs due to throat closure by heating and the saturation line of air are also indicated on Fig. 4.

TABLE 1

Formal Mach Number Determinations from Pressure Measurements at Nozzle Exit for Low Supply Temperature

$M(A/A^*)$ AREA RATIO	$M(p_{t_2}/p_0)$ PITOT PRESSURE	$M(p/p_0)$ STATIC PRESSURE	$M(p_{t_2}/p)$ RAYLEIGH FORMULA	APPROXIMATE SUPPLY PRESSURE IN ATM
6	5.60	5.53	5.39	3
7	6.65	6.10	5.07	5
7.6	7.10	6.44	5.20	7
9	8.07	7.12	5.37	8
10	APPR. 9.4	—	—	8
11	APPR. 9.8–10.4	—	—	8

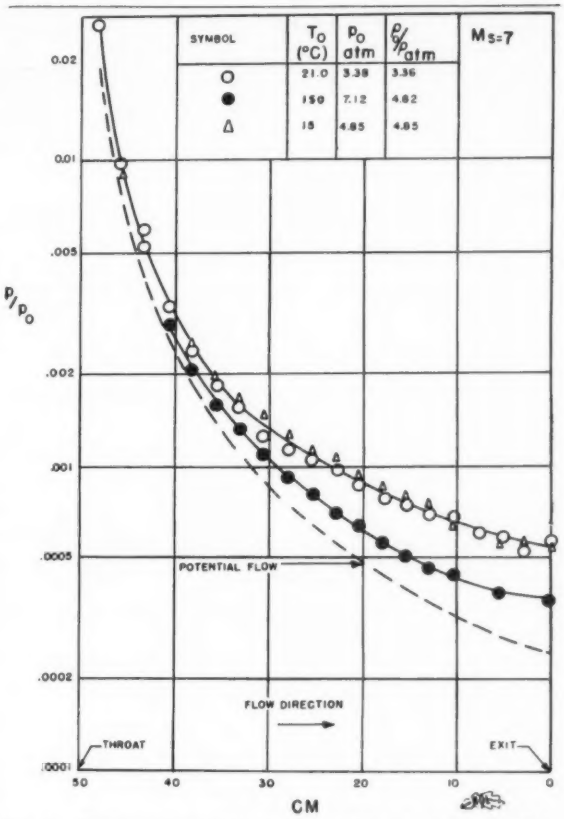

FIG. 3. Static pressure measurements on nozzle-wall centerline.

THERMODYNAMICS OF THE CONDENSATION PROCESS

Scrutiny of Fig. 3 shows that the expansion with air condensation is characterized by a *gradual* deviation of static pressure from that obtained for the hot run without condensation. It can be shown that this deviation begins about the time that M_c is reached in the nozzle. The exact location of beginning condensation is difficult to determine because of the inaccuracy of static pressure measurements. At M_c, flow pressure and temperature are equal to equilibrium saturation pressure and temperature of air. Our seemingly gradual air condensation would be unlikely to occur without a sufficient number of condensation nuclei available at or near the air saturation point. These nuclei provide surfaces for the air to condense on. It was estimated that these nuclei are, in fact, available in large numbers because of the previous condensation of the rest of unavoidable water vapor and of carbon dioxide in the air, upstream of the air saturation point. With this assumption we suppose that the condensation process is the following: The air follows a perfect-gas isentrope up to the saturation line. The air then enters the region of coexistence of liquid and vapor phase and follows there an isentropic *saturated* expansion. With the knowledge of the vapor-pressure

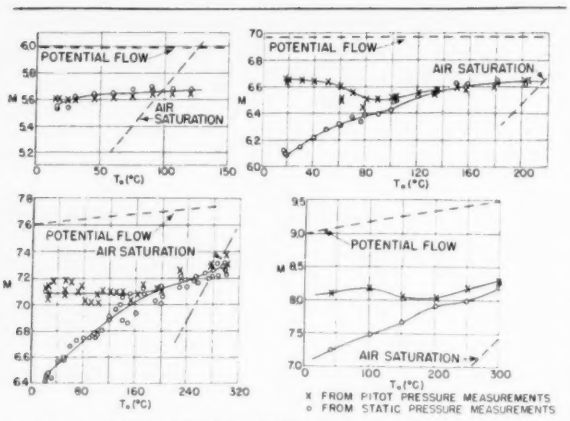

FIG. 4. Mach Number determined from pitot and static pressure measurements at nozzle exit as a function of wind-tunnel supply temperature.

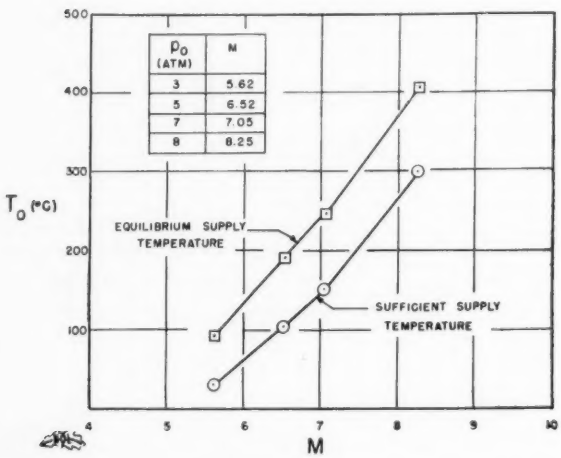

FIG. 5. Preliminary experimental criteria for supply temperatures to minimize air-condensation effects in the test section.

equation, equation of state, and experimental data on the static pressure with condensation (cold runs in Fig. 3), all other flow quantities of interest can be computed by use of the thermodynamics of flow systems.[9] The list below summarizes the effects of condensation on flow parameters. All parameters are made dimensionless relative to conditions upstream of the saturation point—e.g., conditions in the settling tank. Each parameter for condensed flow is then compared to that obtained at the same M_s with the supply temperature raised to T_{0c} so that no condensation occurs. Then one finds, for the dimensionless parameters, that:

(a) Pitot pressure remains nearly unchanged.

(b) Static pressure does not drop to low values.

(c) Average density (liquid plus vapor) remains nearly unchanged.

(d) Temperature does not drop to low values.

(e) Velocity remains nearly unchanged.

(f) Actual-flow Mach Number does not increase to high values.

(g) The amount of air liquefied at the nozzle end is about 10 to 20 per cent of the total air mass for the N.O.L. pressures, temperatures, and Mach Numbers.

(h) Evaluating M from isentropic-flow tables is a formal procedure leading to incorrect results.

The above list provides a tentative guide to the selection of proper methods of investigation of condensation effects. Quantitative data, computed from this thermodynamic condensation model, however, depend in their accuracy on the measured expansion and, in particular, on available vapor-pressure data.[1] The latter are obtained by extrapolation from measurements made of pressures and temperatures that are higher than those found in the wind tunnel, thus introducing considerable uncertainty.[9]

Preliminary Criteria for Flows Practically Free of Air Condensation

Examination of Fig. 4 shows that general agreement of Mach Numbers derived from pitot pressure and static pressure measurements with an isentropic-flow table occurs before T_0 reaches T_{0c}. An investigation of this apparent agreement reveals four factors. (1) Any increase in T_0 increases M_c (Fig. 2). (2) If the expansion is started at larger specific volumes, as is the case for higher T_0, inspection of a p-v diagram shows that the rate of liquefaction during the expansion is smaller.[10] (3) The existing measuring accuracy does not permit detection of small amounts (order of 5 per cent or less) of liquid air in the flow. Therefore, it is assumed that supply temperatures sufficient to result in agreement of Mach Number determinations by different measurement methods on the basis of perfect-gas expansions, are sufficient to permit survey model testing. (4) Because of the inability to locate the beginning of condensation exactly, some supersaturation is not impossible. The resulting saving in supply temperature is shown in Fig. 5 which is applicable only to a tunnel of the size of the N.O.L. tunnel and a measuring accuracy and p_0-range like that of our tests. The supply temperatures that minimize air condensation effects are then about 100°C. below T_{0c}.

Observations on Simple Bodies

Only small changes in Mach angle and shock-wave angle on bodies take place if the Mach Number of the flow changes from, say, 8 to 10. In general, the shock-wave pattern around bodies is rather insensitive to M changes in the hypersonic range. However, qualitative data can be obtained from shock angles as shown on Fig. 6. Three schlieren pictures of a 10° wedge are shown at $M_s = 7$. The supply temperature ranges from low temperatures to T_{0c}, while the supply density is kept constant to minimize changes of the

refractive index in the test section. The increase in M due to elimination of condensation by preheating can now be seen directly as a decrease in shock angle on the 10° wedge by noting the wave position with respect to the (accidental) bubble in the glass wall. The top curve of Fig. 7 gives these shock angles determined by two observers for both sides of the wedge from several such pictures. No further decrease in shock angle or corresponding increase in Mach Number can be noted above about $T_0 = 150$°C.—the temperature that was termed sufficient to minimize liquefaction effects at this M_s (Fig. 5). The Mach Numbers determined from the shock angle for a theoretical 5° flow deflection[11] at high supply temperature without liquefaction are lower than those given for example by static pressure (Fig. 4). This is due to the boundary layer on the wedge which increases the "effective" flow deflection angle. The lower curve in Fig. 7 presents an attempt to eliminate this boundary-layer influence. The wedge-surface pressure is measured by one pressure tap on each side, halfway between tip and end of the wedge. Since the static pressure ahead of the wedge is also known, the pressure ratio across the oblique shock can be determined. From the relationship of this pressure ratio to Mach Number and shock angle for plane flow deflections,[8] M can be determined without knowing the deflection angle. Since both wedge sides show systematically different shock angles, a $^1/_2$° correction is applied to compensate for either flow inclination or misalignment of the model. Again, this is a "formal" evaluation (bottom, Fig. 7) which is correct only at the high supply temperatures. That the Mach Number at high supply temperatures is still lower than that found by static pressure (dashed line) may be attributed to the fact that the pressure on other points of the wedge surface is different from that measured at the center-point. This fact points out the need of detailed studies of viscous effects at hypersonic Mach Numbers. Shock angles on blunter bodies (above about 40° nose angle) were found to be rather insensitive to condensation or M changes. In particular, no difference in the shock pattern about spheres could be noted with or without condensation. It is suspected that strong shocks with their considerable increases in pressure and temperature cause a vaporization of some of the liquefied air. This phenomenon has previously been observed for condensed water vapor by the method of light scattering by Head.[12] In the N.O.L. air case, light scattering is also visible if a strong beam of collimated light traverses the condensed flow. This light scattering disappears behind strong shocks on bodies, as well as in the boundary layer. (It also disappears if the air is heated.)

Fig. 8 shows a 40° cone-cylinder body at $M = 8.25$. Air-condensation effects are negligible at $T_0 = 300$°C. (Figs. 4 and 5), and this is the highest Mach Number achieved to date at N.O.L. The schlieren system

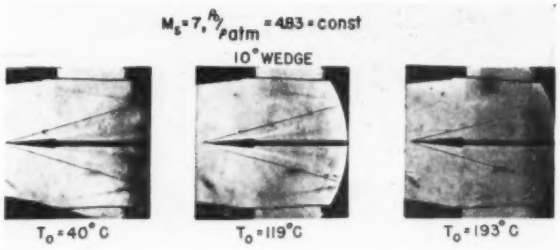

FIG. 6. Schlieren picture of head shock wave on a 10° wedge as a function of supply temperature.

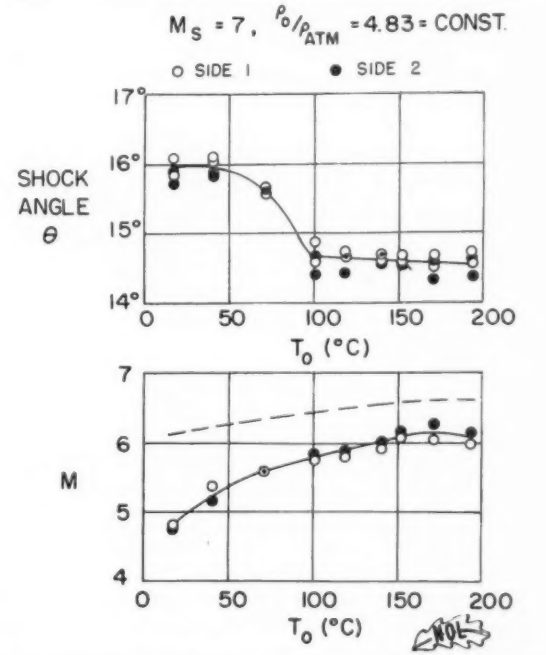

FIG. 7. Shock angle on 10° wedge as a function of supply temperature (*top*) and M-evaluation from shock angle and wedge-surface pressure in comparison to that from static pressure (*bottom*).

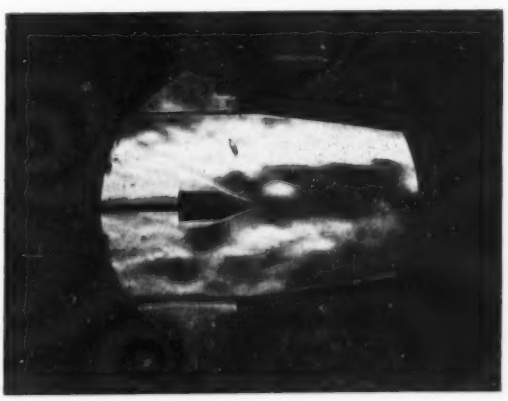

FIG. 8. Schlieren picture of 40° cone-cylinder body at $M = 8.25$ ($p_0 = 7.8$ atmospheres, $T_0 = 300$°C.).

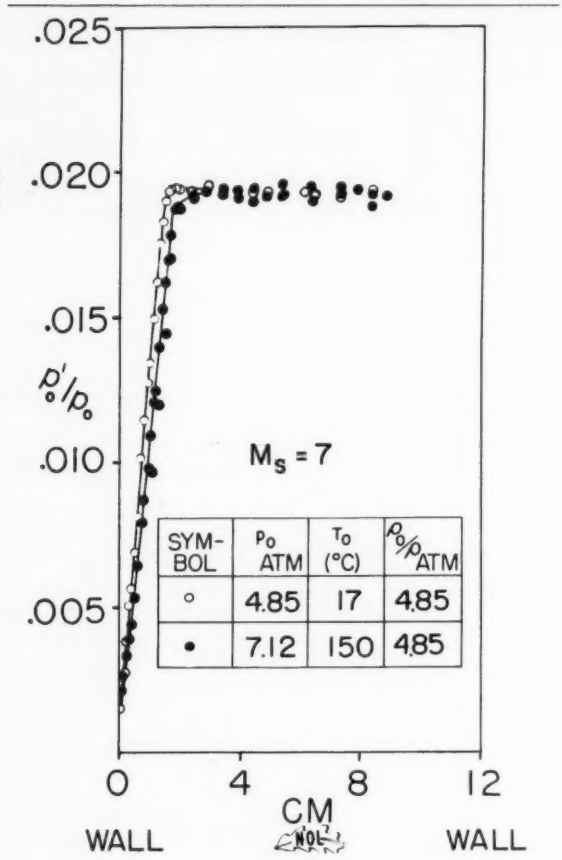

FIG. 9. Pitot-pressure profiles at right angle to nozzle wall at the nozzle-exit center for flow with and without air condensation.

shows only the head wave (static pressure in the test section is about $^1/_2$ mm. mercury), and the picture is further obscured by air convection on the outside of the "hot" tunnel. New methods of flow visualization must be developed for such cases. However, it can be seen that all changes in flow conditions due to the presence of the body are confined to a narrow zone near the body.

OBSERVATIONS OF BOUNDARY LAYERS AND FLOW SEPARATION

Fig. 9 shows two pitot-pressure profiles taken from nozzle wall to centerline at right angles to the flow at the nozzle exit center. In both cases the supply density is the same. One case is with, the other without, air condensation. That condensation does not affect pitot pressure in the center of the flow was shown on Fig. 4. However, in the boundary layer the pitot profiles also show no marked difference. On the other hand, tentative stagnation temperature profiles, measured with a shielded total head temperature probe traversing the flow like the pitot tube, are different with and without liquefaction. For hot runs, the ratio of stagnation to supply temperature reaches a maximum at the edge of the boundary layer, as also observed by McLellan at about the same Mach Number.[13] With condensation, this maximum of the ratio reaches higher values and is moved into the middle of the boundary layer. Before quantitative data can be given, more development and calibration work on such shielded probes is required, since they must operate free of errors because of radiation in the immediate vicinity of the heated nozzle walls.

Some observations tentatively identified as flow separation might be of further interest. Fig. 10 shows boundary-layer profiles taken as the ones shown before. Only hot runs (to eliminate condensation) are given for various Reynolds Numbers, where Reynolds Number is based on centerline free-stream conditions at the nozzle exit for the 12-cm. width of the nozzle. With decreasing Reynolds Number the flow apparently detaches from the nozzle wall, as evidenced by the increased peak size in the pitot profiles. The effect can also be observed with the schlieren system. On the nozzle-wall side of the profiles near the maximum, the pitot pressure fluctuates pointing to an unsteady back-and-forth motion of the separation point. The same

(Continued on page 682)

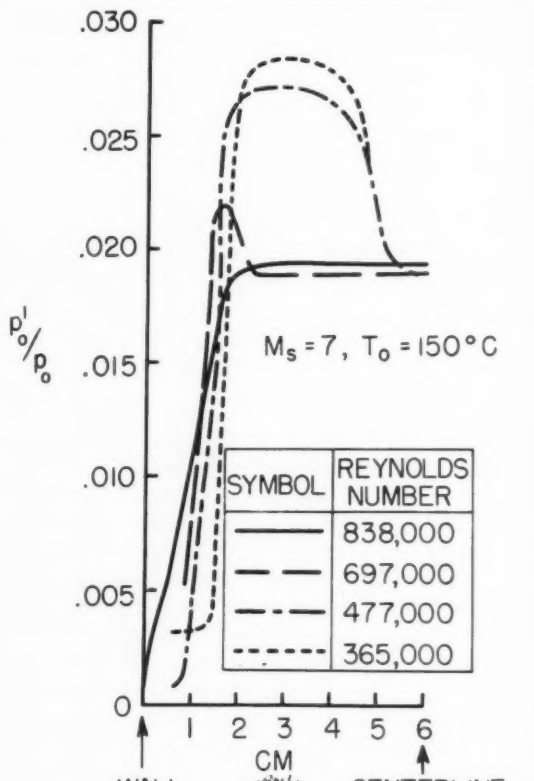

FIG. 10. Pitot profiles at right angle to nozzle wall at nozzle-exit center for different Reynolds Numbers.

Skin-Friction and Heat-Transfer Characteristics of a Laminar Boundary Layer on a Cylinder in Axial Incompressible Flow*

R. A. SEBAN† AND R. BOND‡
University of California at Berkeley

ABSTRACT

A solution is given for the case of the laminar boundary layer of an incompressible fluid of constant properties on the exterior of a cylinder with flow parallel to the cylinder axis. This case differs from the Blasius solution for flow along a flat plate by considering the effect of the curvature in a plane transverse to the flow direction. The local skin-friction and heat-transfer coefficients for a Prandtl Number of 0.715 are evaluated and compared to the similar magnitudes for flat plate flow, and the effect of the curvature is shown to be significant in some practical cases. Recovery factors are evaluated, and this quantity is found to be insensitive to the effect of curvature of the boundary.

NOMENCLATURE

- a = cylinder radius, ft.
- c_p = heat capacity at constant pressure, B.t.u./slug °F.
- H = enthalpy, B.t.u./slug.
- k = thermal conductivity, B.t.u./(hr. °F. ft.)
- q = heat flux, B.t.u./(ft.² hr.)
- r = radial coordinate, ft.
- T = temperature, °F.
- u = axial velocity component, ft. per sec.
- v = radial velocity component, ft. per sec.
- x = axial coordinate, ft.
- ν = kinematic viscosity, sq.ft. per sec.
- ρ = fluid density, slugs per cu.ft.
- σ = Prandtl Number, $\mu c_p/k$
- τ = shear stress, lbs. per sq.ft.
- μ = absolute viscosity, lb. sec./ft.²
- ψ = stream function
- ξ = modulus giving relative thickness of boundary layer, $4(x/a)\sqrt{\nu/u_0 x}$
- $u_0 x/\nu$ = Reynolds Number
- c_f = skin-friction coefficient

Subscripts

- 0 = free-stream condition
- w = wall condition
- F.P. = flat plate value for same Reynolds Number

Received March 10, 1951.
* This paper is based on research conducted under Air Force Contract W33-038-ac-15229, and this support is gratefully acknowledged.
† Associate Professor of Mechanical Engineering.
‡ Research Engineer.

INTRODUCTION

WITH THE INCREASED FREQUENCY of prototype flight and model tests under low-pressure conditions, the characteristics of a boundary layer, the significant dimension of which is comparable to the model dimension, have become of significance. It can be noted superficially that, for the case of a boundary-layer flow over a slender body, the momentum and energy rates within the boundary layer will be increased over the corresponding magnitudes for a flat surface because of the curvature of the boundary layer in a plane transverse to the flow. If the boundary-layer thickness becomes comparable to the thickness of the body, it is to be expected that this effect will become significant.

The simplest model upon which an analytical investigation of this effect can be carried out is that of a laminar boundary layer of a fluid of constant properties on a slender circular cylinder with axis parallel to the flow. To make the analysis possible, it is necessary to postulate the beginning of the boundary layer with zero thickness at the leading edge of the cylinder. While this is an abnormal requirement, assuming a suction flow through the interior of the cylinder of such magnitude as to make the stagnation stream lines of the flow coincident with the cylinder generators, it will be noted later that the applicability of the solution may not be essentially restricted by the necessity of this assumption.

This problem, which differs from the Blasius solution for a laminar boundary layer on a flat plate only in the curvature of the surface transverse to the direction of flow, has been noted by Young,[1] Jakob and Dow,[2] and others. Their considerations involved the assumption that the velocity distribution within the boundary layer and the growth of the boundary layer upon the cylindrical surface were the same as upon a flat plate. Application of the integral form of the momentum equation under these assumptions yielded an expression for the local skin-friction coefficient, the magnitude thereof being greater than that for the flat plate because of the proportionately greater cross section of the boundary layer on the curved surface. Young found that the local skin-

friction coefficient for the cylindrical surface could be related to that for the flat plate for the same length Reynolds Number by the expression

$$c_f/c_{f_{\text{F.P.}}} = 1 + \xi$$

where

$$\xi = 4(x/a)\sqrt{\nu/u_0 x}$$

In the present investigation the problem is considered more exactly, without requiring assumptions of the type used by Young. In addition, the solution of the momentum equation has been applied to the energy equation to specify the rate of heat transfer and the effect of frictional heating for a fluid such as air, having a Prandtl Number of 0.715.

Analysis

For the case of an incompressible fluid of constant properties flowing with uniform free-stream velocity parallel to the axis of a right circular cylinder, the boundary-layer forms of the equations of continuity, momentum, and energy can be written as follows:

$$\frac{\partial u}{\partial x} + \frac{1}{r}\frac{\partial (rv)}{\partial r} = 0 \tag{1}$$

$$\rho\left[u\frac{\partial u}{\partial x} + v\frac{\partial u}{\partial r}\right] = \frac{1}{r}\frac{\partial (r\tau)}{\partial r} \tag{2}$$

$$\rho\left[u\frac{\partial H}{\partial x} + v\frac{\partial H}{\partial r}\right] = \tau\frac{\partial u}{\partial r} + \frac{1}{r}\frac{\partial (rq)}{\partial r} \tag{3}$$

with

$$\tau = \mu(\partial u/\partial r) \tag{4}$$

$$q = k(\partial H/\partial r) \tag{5}$$

Eq. (1) is satisfied by the introduction of a stream function, such that

$$u = (1/r)(\partial\psi/\partial r) \tag{6}$$

$$v = -(1/r)(\partial\psi/\partial x) \tag{7}$$

The remaining equations, Eqs. (2) to (5), are transformed by a change of variables—the independent variables (x, r) to (ξ, η) and the dependent variables (ψ, H) to (f, g). The transformation is defined by

$$\xi = (4/a)\sqrt{\nu x/u_0} \tag{8}$$

$$\eta = \sqrt{u_0/\nu x}[(r^2 - a^2)/4a] \tag{9}$$

$$\psi = a\sqrt{\nu x u_0}f \tag{10}$$

$$H = H_0 + u_0^2 g \tag{11}$$

Eqs. (6) and (7) then become

$$u = (u_0/2)(\partial f/\partial\eta) \tag{12}$$

$$v = \frac{1}{2}\frac{a}{r}\sqrt{\frac{\nu u_0}{x}}\left(\eta\frac{\partial f}{\partial\eta} - f\right) - \frac{2\nu}{r}\frac{\partial f}{\partial\xi} \tag{13}$$

Eqs. (2) to (5), for momentum and energy, become

$$\frac{\partial}{\partial\eta}\left[(1 + \eta\xi)\frac{\partial^2 f}{\partial\eta^2}\right] + f\frac{\partial^2 f}{\partial\eta^2} + \xi\left(\frac{\partial f}{\partial\xi}\frac{\partial^2 f}{\partial\eta^2} - \frac{\partial f}{\partial\eta}\frac{\partial^2 f}{\partial\eta\partial\xi}\right) = 0 \tag{14}$$

$$\frac{1}{\sigma}\frac{\partial}{\partial\eta}\left[(1 + \eta\xi)\frac{\partial g}{\partial\eta}\right] + f\frac{\partial g}{\partial\eta} + \frac{1}{4}(1 + \eta\xi)\left(\frac{\partial^2 f}{\partial\eta^2}\right)^2 + \xi\left(\frac{\partial f}{\partial\xi}\frac{\partial g}{\partial\eta} - \frac{\partial f}{\partial\eta}\frac{\partial g}{\partial\xi}\right) = 0 \tag{15}$$

$$\tau = \frac{1}{4}\frac{r}{a}\mu u_0\sqrt{\frac{u_0}{\nu x}}\frac{\partial^2 f}{\partial\eta^2} \tag{16}$$

$$q = \frac{1}{2}\frac{r}{a}\frac{k}{c_p}u_0^2\sqrt{\frac{u_0}{\nu x}}\frac{\partial g}{\partial\eta} \tag{17}$$

The boundary conditions considered are $u = 0$ and $v = 0$ for $r = a$ and $u = u_0$ and $H = H_0$ for $r = \infty$ or $x = 0$. In the new variables these boundary conditions become

$$f = 0, \quad \frac{\partial f}{\partial\eta} = 0, \quad \frac{\partial f}{\partial\xi} = 0 \quad (\text{for } \eta = 0) \tag{18}$$

$$\partial f/\partial\eta = 2, \quad g = 0 \quad (\text{for } \eta = \infty) \tag{19}$$

Taking the wall value in Eq. (16), the local skin-friction coefficient is

$$c_f = \frac{\tau_{r=a}}{(\rho/2)u_0^2} = \frac{1}{2}\sqrt{\frac{\nu}{x u_0}}\left(\frac{\partial^2 f}{\partial\eta^2}\right)_{\eta=0} \tag{20}$$

A boundary-layer displacement thickness is defined as

$$\delta_1 = \int_a^\infty\left(1 - \frac{u}{u_0}\right)\frac{r}{a}\,dr = \sqrt{\frac{\nu x}{u_0}}\lim_{\eta\to\infty}(2\eta - f) \tag{21}$$

The method of solution adopted for the determination of f and g from Eqs. (14) and (15) is based on expansion in a series of functions of η with each function multiplied by a power of ξ. The functions thus become

$$f(\xi, \eta) = f_0(\eta) + \xi f_1(\eta) + \xi^2 f_2(\eta)\ldots \tag{22}$$

$$g(\xi, \eta) = g_0(\eta) + \xi g_1(\eta) + \ldots \tag{23}$$

Substitution of these functions in Eqs. (14) and (15) and equation of the coefficients of like powers of ξ to zero yield a series of differential equations as follows:

$$f_0''' + f_0 f_0'' = 0 \tag{24}$$

$$f_1''' + f_0 f_1'' - f_0' f_1' + 2f_0'' f_1 + \eta f_0''' + f_0'' = 0 \tag{25}$$

$$f_2''' + f_0 f_2'' - 2f_0' f_2' + 3f_0''' f_2 + \eta f_1''' + f_1'' + 2f_1 f_1'' - f_1'^2 = 0 \quad (26)$$

.....

$$(1/\sigma) g_0'' + f_0 g_0' + (1/4) f_0''^2 = 0 \quad (27)$$

$$\frac{1}{\sigma} g_1'' + f_0 g_1' - f_0' g_1 + \frac{1}{\sigma}(\eta g_0'' + g_0') + 2f_1 g_0' - \frac{\eta}{4} f_0''^2 + \frac{1}{2} f_0'' f_1'' = 0 \quad (28)$$

The boundary conditions associated with f_0, f_1, f_2 are

$$\begin{array}{ll} f_0(0) = f_0'(0) = 0 & f_0'(\infty) = 2 \\ f_1(0) = f_1'(0) = 0 & f_1'(\infty) = 0 \\ f_2(0) = f_2'(0) = 0 & f_2'(\infty) = 0 \\ \cdots & \cdots \end{array}$$

For the functions g_0, g_1, ..., the only prescribed boundary conditions are

$$g_0(\infty) = 0, \; g_1(\infty) = 0, \; \ldots$$

while the values of the function and its derivatives at $\eta = 0$ are adjustable to accommodate a choice of thermal boundary conditions at the wall.

Eq. (24) is the well-known Blasius equation, and its solution has been taken from the calculations of Cope and Hartree.[3] Approximate solutions of Eqs. (25) and (26) were then obtained by numerical integration using first-order approximations with finite intervals of 0.1 in the independent variable. Curves of the functions f_1' and f_2' so determined are shown on Fig. 1, and these functions specify the velocity distribution. The most important results are in the values of the functions at the extreme values of η. These are

$$f_0''(0) = 1.328, \; f_1''(0) = 0.704, \; f_2''(0) = -0.095 \quad (29)$$

$$\lim_{\eta \to \infty} (2\eta - f_0) = 1.721, \; f_1(\infty) = 0.051, \; f_2(\infty) = -0.093 \quad (30)$$

The availability of the functions f_1 and f_2 enables the solution of the energy equations, Eqs. (27) and (28), in a similar way. This has been done for a Prandtl Number of 0.715, leading to the following results:

$$g_0'(0) = 0.249 - 0.590 g_0(0) \quad (31)$$

$$g_1'(0) = 0.1457 - 0.339 g_0(0) - 0.7824 g_1(0) \quad (32)$$

The skin-friction coefficient and boundary-layer displacement thickness as defined by Eqs. (20) and (21) can be evaluated from the known functions. The skin-friction coefficient is

$$c_f = 0.664 \sqrt{\nu / x u_0} (1 + 0.53\xi - 0.071\xi^2 \ldots) \quad (33)$$

The first factor on the right of Eq. (33) is the skin-friction coefficient for a flat plate as given by the Blasius solution. Designating this by $c_{f\,\text{F.P.}}$, the result given by Eq. (33) can also be written as

$$c_f / c_{f\,\text{F.P.}} = 1 + 0.53\xi - 0.071\xi^2 \ldots$$

The displacement thickness is

$$\left.\begin{array}{l} \delta_1 = \sqrt{\nu x / u_0} \left[\lim_{\eta \to \infty} (2\eta - f_0) - \xi f_1(\infty) - \xi^2 f_2(\infty) \ldots \right] \\ \delta_1 = 1.721 \sqrt{\nu x / u_0} (1 - 0.029\xi + 0.054\xi^2 \ldots) \end{array}\right\} \quad (34)$$

and this can be written in reference to flat plate values as

$$\delta_1 / \delta_{1\,\text{F.P.}} = 1 - 0.029\xi + 0.054\xi^2 \ldots$$

The expressions of Eqs. (33) and (34) are approximations permissible only if ξ is small. An estimate of this approximation can be gained from Fig. 2, where the representation of Eq. (33) reveals that the use of the first two terms of that equation expresses the skin-friction coefficient within 10 per cent at values of ξ large enough to make $c_f / c_{f\,\text{F.P.}}$ equal to 1.50.

The boundary-layer thickness as given by Eq. (34) is seen to be initially less than that for a flat plate. Its subsequent behavior is not clearly defined because of the poor convergence and limited number of terms in the series as obtained.

The heat-transfer rate at the wall is given by Eq. (17) and the results as given by Eqs. (31) and (32). This is

$$q = (1/2)(k/c_p) u_0^2 \sqrt{u_0 / \nu x} \{0.249 - 0.59 g_0(0) + [0.1457 - 0.34 g_0(0) - 0.782 g_1(0)]\xi + \ldots\} \quad (35)$$

This result is unwieldy and simple results are obtained only for some special cases.

For an insulated wall, $q = 0$ for all ξ, and two equations result from Eq. (35), from which $g_0(0)$ and $g_1(0)$ can be calculated. Then

$$g(\xi, 0) = 0.422 + 0.0034\xi \ldots \tag{36}$$

and the surface temperature is (with $H = c_pT$)

$$T(\xi, 0) = T_0 + (u_0^2/2c_p)(0.844 + 0.007\xi \ldots) \tag{37}$$

The last terms, which give the recovery factor, are seen to depend but slightly on ξ and are practically equivalent to the recovery factor of 0.844 resulting from the Pohlhausen solution for the flat plate for the Prandtl Number of 0.715 as considered.

For the case of low-velocity flow, in which the frictional heating effect may be neglected, Eq. (35) assumes the simpler form

$$q = (1/2)(k/c_p)u_0^2\sqrt{u_0/\nu x}\{-0.59g_0(0) + [-0.34g_0(0) - 0.782g_1(0)]\xi \ldots\} \tag{38}$$

If, in addition, the temperature is uniform along the wall, then

$$g_0(0) = (c_p/u_0^2)(T_w - T_0)$$

and $g_1(0)$ must be zero. A heat-transfer coefficient can then be defined as

$$h = -q/(T_w - T_0) = 0.295k\sqrt{u_0/\nu x}(1 + 0.575\xi + \ldots) \tag{39}$$

and the Nusselt Number is given by the equation

$$hx/k = 0.295\sqrt{xu_0/\nu}(1 + 0.575\xi + \ldots) \tag{40}$$

In this equation the first factor on the right side is the expression of the Nusselt Number for the case of flow over an isothermal flat plate.

If the velocity is large enough so that frictional heating must be taken into account, it is not possible to express rigorously the heat-transfer coefficient in terms of an effective temperature difference. For the case of uniform wall temperature, $g_1(0) = 0$, and the heat rate is given as

$$q = (1/2)(k/c_p)u_0^2\sqrt{u_0/\nu x}[-0.59(1 + 0.575\xi)(c_p/u_0^2)(T_w - T_0) + 0.249(1 + 0.585\xi)]$$

This is, approximately,

$$\begin{aligned} q &= k\sqrt{\frac{u_0}{\nu x}}\left[-0.295(T_w - T_0) + 0.1245\frac{u_0^2}{2c_p}\right](1 + 0.58\xi) \\ &= -0.295k\sqrt{\frac{u_0}{\nu x}}\left[T_w - \left(T_0 + 0.844\frac{u_0^2}{2c_p}\right)\right](1 + 0.58\xi) \end{aligned} \tag{41}$$

Since $[T_0 + 0.844(u_0^2/2c_p)]$ is approximately the adiabatic wall temperature, the definition of the effective temperature difference in the usual way, as the difference between the wall temperature and the adiabatic wall temperature, will give, from Eq. (41), a heat-transfer coefficient and Nusselt Number similar to that given by Eqs. (39) and (40) for the case of nondissipative flow over an isothermal plate.

It is of further interest to note that the combination of Eqs. (40) and (33) yields the expression

$$\frac{hx/k}{(u_0x/\nu)\sigma^{(1/3)}} = \frac{c_f}{2}\frac{1 + 0.575\xi}{1 + 0.53\xi}; \qquad \sigma = 0.715 \tag{42}$$

It is seen from this expression that the ratio of the heat-transfer to skin-friction coefficients is but slightly affected by the curvature of the wall.

Discussion

The results of the present theoretical investigation reveal that, while the effect of curvature on the skin-friction coefficient for the case of laminar boundary-layer flow parallel to a cylinder is not so great as estimated by Young, it is still significant in many possible cases. The solution has been extended to give wall temperatures and heat rates for the cases of an adiabatic and isothermal wall, with and without frictional heating. In the case of the energy equation, the results, given for $\sigma = 0.715$, were not carried out to so good an approximation as for the momentum equation, but they are of sufficient accuracy up to the point at which the heat-transfer coefficient is increased, by the effect of curvature, to one and one-half times its flat plate value.

The effects of curvature on the skin-friction and heat-transfer coefficients are similar, so that the ratio

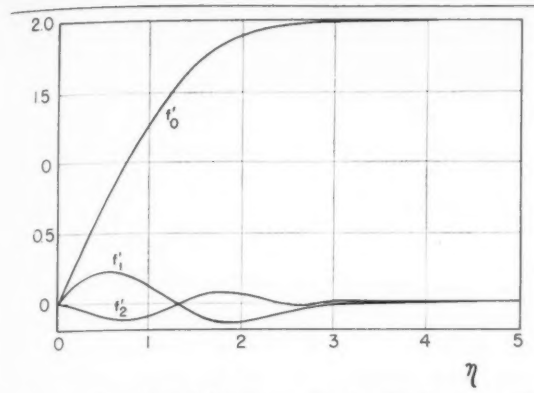

FIG. 1. Functions defining the velocity distribution. The function $f_0'(\eta)$ defines the flat plate velocity distribution, and the velocity distribution on the cylinder is given by

$$u/u_0 = {}^1/_2[f_0'(\eta) + \xi f_1'(\eta) + \xi^2 f_2'(\eta) \ldots .]$$

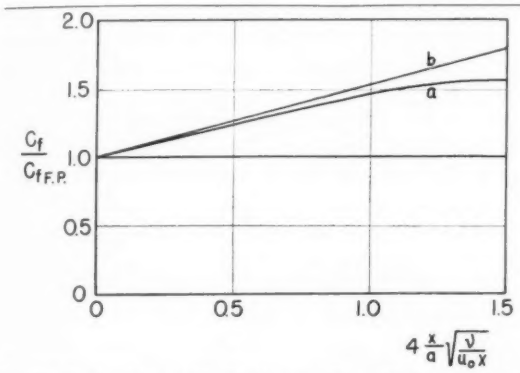

FIG. 2. Ratio of local skin friction on the cylinder to that on plate at same Reynolds Number.

(a) $c_f/c_{f_{F.P.}} = 1 + 0.53\xi - 0.071\xi^2$

(b) $c_f/c_{f_{F.P.}} = 1 + 0.53\xi$

of these coefficients remains almost unaltered from its flat plate value. The recovery factor is relatively unaffected by the curvature, and this lack of sensitivity is probably due to the almost equal increase in the heat-transfer and skin-friction coefficients.

The relative magnitude of the effect of curvature can be demonstrated by the consideration of some typical cases. If the circumstances under which the local skin friction is increased by 10 per cent over the value that would obtain on a flat plate at the same Reynolds Number are considered, then at this point, from Eq. (33), $\xi = 0.19$ and

$$\frac{x}{a} = \frac{0.19}{4}\sqrt{\frac{u_0 x}{\nu}} \approx 0.05\sqrt{\frac{u_0 x}{\nu}}$$

or

$$x/a = 25 \times 10^{-4}(u_0 a/\nu)$$

For a 1-in. diameter cylinder, with $u_0 = 100$ ft. per sec. and $\nu = 1.8 \times 10^{-4}$ sq.ft. per sec., typical of air conditions near ground level, this gives $x/a = 580$, so that for most practical cases the effect would be insignificant. If, however, with all other conditions remaining the same, the pressure is reduced to 1/100 of an atmosphere, the skin-friction coefficient (and the heat-transfer coefficient) would be 10 per cent above the flat plate magnitude at $x/a = 5.80$.

For a cylinder 4 ft. in diameter, in flight under standard atmosphere conditions, the local skin-friction coefficient exceeds the flat plate magnitude, $c_f = 1.10 c_{f\,F.P.}$, at a point 20 ft. from the leading edge when the Mach Number is 1.3 at an altitude of 200,000 ft. and when the Mach Number is 3.5 at 240,000 ft.

It was noted initially that the determination of the solution required the assumption of zero boundary-layer thickness at the leading edge of the cylinder, a condition impossible to fulfillment in practical cases. While little is known in general of the development of a laminar boundary layer on an arbitrary body of revolution, the development of a laminar boundary layer on a half body has been studied by Scholkemeier.[4] He demonstrated that on this body the boundary layer assumes the characteristics of a boundary layer of a flat plate at a distance of $1^1/_2$ diameters from the stagnation point, the Reynolds Number for a flat plate case being taken on the basis of the meridianal distance from the stagnation point. The similarity of the half body to a cylinder with a hemispherical nose suggests that this type of evaluation, combined with the methods outlined herein, will correctly establish the boundary-layer characteristics on a cylinder of this type.

REFERENCES

[1] Young, A. D., *The Calculations of the Total and Skin Friction Drags of Bodies of Revolution at Zero Incidence*, R&M 1874, British A.R.C., 1939.

[2] Jakob, M., and Dow, W. M., *Heat Transfer from a Cylindrical Surface to Air in Parallel Flow with and Without an Unheated Starting Section*, Trans. A.S.M.E., Vol. 68, No. 2, 1946.

[3] Cope, W., and Hartree, D., *The Laminar Boundary Layer in a Compressible Flow*, Phil. Trans. of the Roy. Soc. of London, *A* No. 827, Vol. 241, June, 1948.

[4] Scholkemeier, T., *The Laminar Friction Layer on Rotationally Symmetrical Bodies*, Braunschweig, Technische Hochschule, no date.

Analysis of a Friction Damper for Clutch-Type Servomechanisms

HERBERT K. WEISS*

Aberdeen Proving Ground

SUMMARY

The stabilizing action of a flywheel, coupled by coulomb friction to the output shaft of a clutch-type servomechanism is analyzed. It is shown that such a damping device is capable of partly compensating for the undesirable effects of time lag in the control. Methods are presented for quickly determining the transient and steady state of both servomechanism and damper for any set of initial conditions. The analysis of the damper-servo system, which has two degrees of freedom, is accomplished by tracing pairs of trajectories in the phase plane. It is shown that for a given design of damper, the amplitude of the steady-state oscillation is proportional to the square of time lag in control functioning, while the period of the oscillation is proportional to the time lag.

Graphs are presented to show the optimum ratio of friction torque to clutch torque for minimum amplitude of steady-state oscillation. The greater the flywheel inertia, the smaller the amplitude of steady-state oscillation can be made for a given time lag in the control. Such damping is always obtained, however, at the expense of maximum servo acceleration, although maximum servo velocity is not reduced by the friction-coupled flywheel.

INTRODUCTION

ONE OF THE SIMPLEST and most useful types of damping devices for suppressing hunting of a servomechanism is a flywheel, coupled to the output shaft of the servo by coulomb friction. Known as a "Lanchester damper," such a device is also used as a vibration damper.[1,2] The analysis offered earlier[2] for the vibration damper is not, however, directly applicable to the servomechanism case, since it assumes that the motion of the oscillating shaft is a sine wave, regardless of the damper's action.

When coupled to the usual torque-producing element of a servomechanism, the friction damper affects the response in such a manner that linear methods of analysis are no longer strictly applicable. In the present study, advantage is taken of phase-plane representation to obtain analyses of the transient and steady-state motion of a clutch-type servomechanism coupled by coulomb friction to an inertia element. This approach permits a graphical solution to be readily obtained for the motion, even though nonlinearities are introduced by the abrupt changes in driving and damping torques.

Received March 12, 1951.

* Chief, Weapons Effectiveness Branch, Ballistic Research Laboratories.

CLUTCH-TYPE SERVOMECHANISM

Descriptions of a clutch-type servo are available in the literature.[3,4] This type of servomechanism has been found useful in applications where the position of a shaft is to be determined accurately but where high-frequency oscillations of small amplitude about the desired position are not undesirable. A constant-speed motor constitutes a source of power to which the output shaft is coupled by friction clutches for rotation in either direction. When a clutch is closed, it is assumed that a constant torque is transmitted across the clutch faces until the output comes up to drive speed—i.e., until relative motion between the clutch faces ceases. For present purposes, the simplest representation of the servo elements will be employed, as indicated in Fig. 1, according to the symbolism originated by Hazen.[5] It is assumed that when servo output differs from input, the proper clutch is closed to apply a torque in a direction tending to reduce the difference to zero. Constant delay time t_d in the action of the clutch is assumed. The load is assumed to consist of inertia alone, the only damping being supplied by the friction-coupled flywheel. Finite size of the inactive zone between the clutch-actuating contacts is neglected. The frictional torque exerted across the friction coupling is assumed to be independent of the magnitude of relative velocity across the coupling faces and to depend only upon the sign of the relative velocity.

The methods to be used are an adaptation of those developed in an earlier study of relay servomechanisms by the author.[6]

SYMBOLS

The parameters associated with the components of the servomechanism in Fig. 1 are identified by the following symbols.

I_m = moment of inertia of the servo plus load, referred to the output shaft

I_d = moment of inertia of the flywheel damper, referred to the output shaft

T_m = torque applied by the driving clutch, referred to the output shaft

T_d = friction torque applied by the damper, referred to the output shaft

θ_m = angular position of servo output shaft

θ_d = angular position of damper

θ_i = angular position of servo input shaft

t = time

t_d = constant time delay in clutch operation

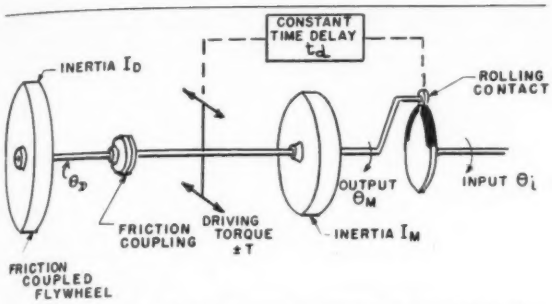

FIG. 1. Schematic of clutch-type servomechanism with friction damper.

The following parameters are derived from those above.

$r_i = I_d/I_m$ = ratio of moments of inertia of damper to servo plus load (1)

$r_t = |T_d/T_m|$ = ratio of damping torque to driving torque (2)

$\delta_m = \theta_m - \theta_i$ = servo error (3)

$\delta_d = \theta_d - \theta_i$ (4)

$\alpha = |T_m/I_m|$ = servo acceleration without damper (5)

τ = time required for the servo without damper to move $1/4$ radian from a rest position—i.e., $1 = 2\alpha\tau^2$ (6)

$s = t/\tau$ = dimensionless measure of elapsed time (7)

$s_d = t_d/\tau$ = dimensionless measure of delay time (8)

Equations of Motion

Summing torques on the servo output shaft

$$I_m\theta_m'' = -T_m \operatorname{sgn}(\theta_m - \theta_i) - T_d \operatorname{sgn}(\theta_m' - \theta_d') \quad (9)$$

where "sgn" means "sign of." Assuming constant input velocity θ_i' and using Eqs. (2), (3), and (4), Eq. (9) is reduced to

$$\delta_m'' = -\alpha \operatorname{sgn} \delta_m - r_t\, \alpha \operatorname{sgn}(\delta_m' - \delta_d') \quad (10)$$

For the damper

$$I_d\theta_d'' = T_d \operatorname{sgn}(\theta_m' - \theta_d') \quad (11)$$

whence

$$\delta_d'' = (r_t/r_i)\alpha \operatorname{sgn}(\delta_m' - \delta_d') \quad (12)$$

The time scale is now changed from t to s by introducing Eq. (7) and noting that

$$\ddot{\sigma}_m = d^2\delta_m/ds^2 = \delta_m''(ds/dt)^2 = \delta_m''\tau^2 \quad (13)$$

Similarly

$$\ddot{\sigma}_d = \delta_d''\tau^2 \quad (14)$$

and also

$$\dot{\sigma}_m = \delta_m'\tau; \qquad \dot{\sigma}_d = \delta_d'\tau \quad (15)$$

$$\sigma_m = \delta_m; \qquad \sigma_d = \delta_d \quad (16)$$

Then the equations of motion for servo and damper become

$$2\ddot{\sigma}_m = -\operatorname{sgn}\sigma_m - r_t \operatorname{sgn}(\dot{\sigma}_m - \sigma_d) \quad (17)$$

$$2\ddot{\sigma}_d = (r_t/r_i) \operatorname{sgn}(\dot{\sigma}_m - \dot{\sigma}_d) \quad (18)$$

Slip-Stick Criterion

Consider the behavior of the servo with damper, when both servo and damper are initially at rest and a control contact is suddenly closed. The driving torque T_m is suddenly applied. A maximum torque T_d can be transferred across the friction coupling to the damper flywheel. Hence, the maximum acceleration of the flywheel is T_d/I_d. If this is greater than the servo acceleration $\ddot{\theta}_m$, the damper "sticks" to the servo, which acts as if it had a total inertia $I_d + I_m$. In this case there is no damping action. In order to obtain damping, the damper flywheel must slip, relative to the servo shaft. It is therefore required, for slipping, that $T_d/I_d < \ddot{\theta}_m$. But if the damper slips

$$\ddot{\theta}_m = (T_m - T_d)/I_m \quad (19)$$

whence the requirement that the damper slip is established by

$$T_d/I_d < (T_m - T_d)/I_m \quad (20)$$

or

$$S < 1.00 \quad (21)$$

where

$$S = r_t/[r_i(1 - r_t)] \quad (22)$$

For the simple servo assumed, if the damper is adjusted according to Eq. (21) so that it slips, it slips as long as the servo is in motion.

Phase Plane and Trajectories

From Eqs. (17) and (18), the motion of damper and servo can be solved simply as long as the signs of σ_m and $(\dot{\sigma}_m - \dot{\sigma}_d)$ do not change. By plotting the "trajectories" of the motion of servo and damper in the "phase," or position-velocity plane, the changes in sign of these quantities can be easily monitored. The phase-plane approach has been extensively studied by Minorsky[7] for problems in nonlinear mechanics, and its application to the analysis of servomechanisms has been made earlier by the writer,[6] and others.[8]

In the present problem, the motion of *two* relatively moving shafts—the shafts of servo and damper—must be simultaneously monitored in order to observe the sign of the difference in velocities. This is accomplished by plotting both $\dot{\sigma}_m$ and $\dot{\sigma}_d$ against σ_m, the latter serving in place of a coordinating time reference. Eqs. (17) and (18) may be written

$$\ddot{\sigma}_m = k_1/2 \quad (23)$$

$$\ddot{\sigma}_d = k_2/2 \quad (24)$$

where k_1, k_2 depend upon the signs of σ_m, and the relative velocity of servo and damper. As long as σ_m and $(\dot{\sigma}_m - \dot{\sigma}_d)$ do not change sign, Eqs. (23) and (24) may be integrated to give

$$\dot{\sigma}_m - \dot{\sigma}_{m0} = k_1 s/2 \quad (25)$$

$$\dot{\sigma}_d - \dot{\sigma}_{d0} = k_2 s/2 \tag{26}$$

$$\sigma_m - \sigma_{m0} = \dot{\sigma}_{m0}\, s + (1/4)k_1 s^2 \tag{27}$$

where σ_{m0}, $\dot{\sigma}_{m0}$, and $\dot{\sigma}_{d0}$ are values at time $s = 0$.

Combining Eqs. (25) and (27),

$$\sigma_m - \sigma_{m0} = (\dot{\sigma}_m{}^2 - \dot{\sigma}_{m0}{}^2)/k_1 \tag{28}$$

Combining Eqs. (26) and (27)

$$\sigma_m - \sigma_{m0} = (k_1/k_2{}^2)\,\{\dot{\sigma}_d - [\dot{\sigma}_{d0} - \dot{\sigma}_{m0}(k_2/k_1)]\}^2 - \dot{\sigma}_{m0}{}^2/k_1 \tag{29}$$

and from Eqs. (25) and (26)

$$\dot{\sigma}_m - \dot{\sigma}_{m0} = k_1/k_2(\dot{\sigma}_d - \dot{\sigma}_{d0}) \tag{30}$$

From Eq. (28), the trajectory of the servo in the phase plane will be identified as a parabola with its axis horizontal, and its vertex at

$$\sigma_m = \sigma_{m0} - \dot{\sigma}_{m0}{}^2/k_1;\ \dot{\sigma}_m = 0 \tag{31}$$

Similarly, the trajectory of the damper in the phase plane is recognized from Eq. (29) to be a parabola with axis horizontal and vertex at

$$\begin{aligned} \sigma_m &= \sigma_{m0} - \dot{\sigma}_{m0}{}^2/k_1 \\ \dot{\sigma}_d &= \dot{\sigma}_{d0} - \dot{\sigma}_{m0}k_2/k_1 \end{aligned} \tag{32}$$

It appears, therefore, that all of the necessary trajectories are parabolas of the form

$$\begin{aligned} \sigma_m &= \dot{\sigma}_m{}^2/k_1 \\ \sigma_m &= \dot{\sigma}_d{}^2\,(k_1/k_2{}^2) \end{aligned} \tag{33}$$

which are shifted in the phase plane to satisfy initial conditions, but which always keep their axes horizontal. The values of k to be used depend upon σ_m, upon the relative velocity of servo and damper, and upon the constants r_t and r_i.

Suppose that servo and damper are initially at rest when a constant velocity of input is applied. Assume also that the damper has been adjusted to slip. Both servo and damper accelerate in a direction to follow the changing input, but since the damper slips, its velocity lags the servo velocity by an increasing amount. When the servo has reduced the difference between output and input to zero, the driving contact opens and the opposing contact closes. After a delay time t_d, the driving torque changes sign. The servo then decelerates, the damper torque aiding the deceleration.

The servo velocity decreases, and the damper velocity increases, until the relative velocity is zero. The relative velocity then changes sign, and the servo continues to decelerate, but less rapidly, since the damper is now opposing the change in velocity. This sequence of events continues to repeat.

Fig. 2 shows a typical steady-state set of trajectories (limit cycles) for servo and damper. The values of k_1, k_2 for each trajectory segment are indicated in Table 1.

Because of the symmetry of the phase-plane picture given for r_t and r_i, only four trajectories are needed to construct a graphical representation of the motion, following any initial conditions. However, before the phase-plane plot can be constructed, it is necessary to establish the contour of torque interchange for constant time lag.

TABLE 1

Segment	k_1	k_2
1–2; 1–2′	$1 - r_t$	r_t/r_i
2–3; 2′–3	$-1 - r_t$	r_t/r_i
3–4; 3–4′	$-1 + r_t$	$-r_t/r_i$
4–1; 4′–1	$1 + r_t$	$-r_t/r_i$

TIME LAG

Let subscript a refer to the instant the servo trajectory crosses the σ_m axis and subscript 2 refer to the point on the trajectory s_d later, at which torque change occurs. From Eq. (25)

$$\dot{\sigma}_{m2} - \dot{\sigma}_{ma} = k_1 s_d/2 \tag{34}$$

and from Eq. (27) with $\sigma_{ma} = 0$

$$\dot{\sigma}_{m2} = \dot{\sigma}_{ma} s_d + (1/4)k_1 s_d{}^2 \tag{35}$$

whence the contour of torque interchange is determined to be the straight line described by

$$\sigma_{m2} = \dot{\sigma}_{m2} s_d - (1/4)k_1 s_d{}^2 \tag{36}$$

CONSTRUCTION OF PHASE-PLANE GRAPHS

Sufficient information is now available to construct phase-plane plots of the transient and steady-state

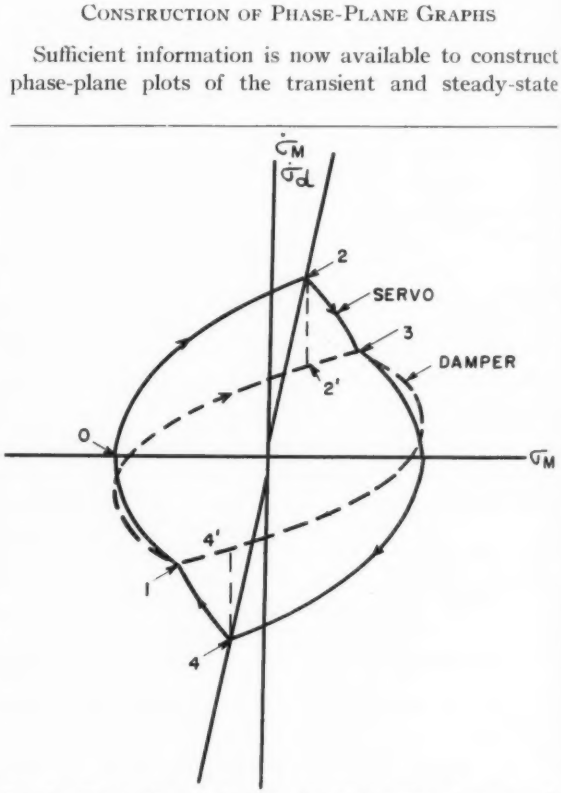

FIG. 2. Phase plane trajectories for limit cycles of servo and damper.

motion of servo and damper for any desired values of the system parameters and initial conditions.

The transient motion of a clutch-type servo with friction damper and the steady-state "limit cycles" eventually attained are shown in Figs. 3, 4, and 5. For all three graphs, constant values of dimensionless delay time s_d and inertia ratio r_t were assumed. The coefficient of friction coupling r_f between servo and damper was, however, progressively increased.

It will be observed that the amplitude of steady-state oscillation is least for the intermediate value of r_t, shown in Fig. 4. It is to be expected that there will be a "best" value of r_t, since there is no damping action if $r_t = 0$ or if $r_t = 0.50$. In the latter case, the damper "sticks," and there is no relative motion and, hence, no damping.

The phase-plane solutions show that there is a limit cycle of steady-state oscillation which the servo attains and in which it hunts endlessly at a definite amplitude and period. It is of interest to obtain a mathematical solution for the amplitude and period.

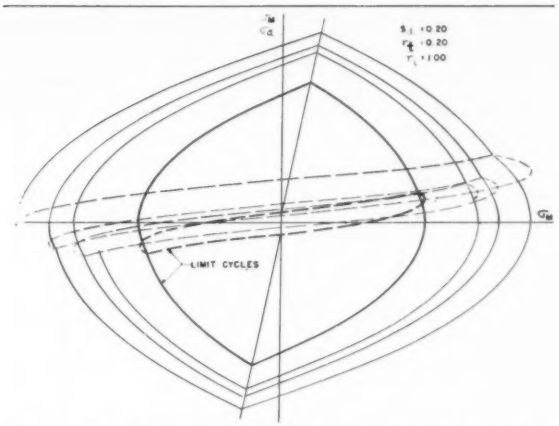

FIG. 3. Phase plane trajectories for servo with light friction coupling.

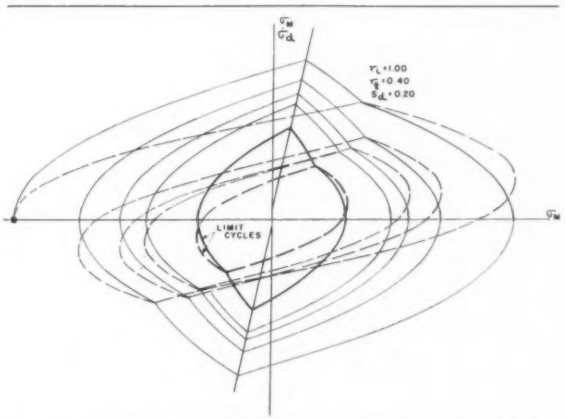

FIG. 4. Phase plane trajectories for servo with medium friction coupling.

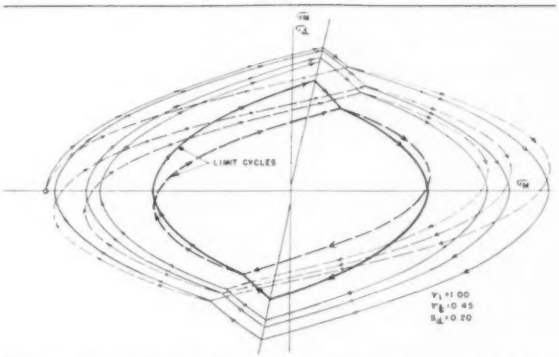

FIG. 5. Phase plane trajectories for servo with heavy friction coupling.

MATHEMATICAL SOLUTION FOR STEADY STATE

The procedure will be to establish the equations for trajectory segments, determine end relations between trajectory segments, including the effect of time lag, and finally eliminate from the system of equations those phase-plane coordinates that are not desired. The result is to yield amplitude and period relations in terms of time delay, damper inertia, and friction.

The notation of Fig. 2 will be used. By symmetry

$$\sigma_{m3} = -\sigma_{m1} \tag{37}$$

$$\dot{\sigma}_{m3} = -\dot{\sigma}_{m1} \tag{38}$$

$$\dot{\sigma}_{d3} = \dot{\sigma}_{m3} = -\dot{\sigma}_{m1} = -\dot{\sigma}_{d1} \tag{39}$$

Between points (*1*) and (*2*), by Eq. (28)

$$\sigma_{m2} - \sigma_{m1} = (\dot{\sigma}_{m2}^2 - \dot{\sigma}_{m1}^2)/(1 - r_t) \tag{40}$$

Between points (*2*) and (*3*)

$$\sigma_{m3} - \sigma_{m2} = (\dot{\sigma}_{m3}^2 - \dot{\sigma}_{m2}^2)/(-1 - r_t) \tag{41}$$

Combining Eqs. (40) and (41).

$$2\sigma_{m2} = (\dot{\sigma}_{m2}^2 - \dot{\sigma}_{m1}^2)\,(1 - \eta)/(1 - r_t) \tag{42}$$

where

$$\eta = (1 - r_t)/(1 + r_t) \tag{43}$$

Writing Eq. (36) in the form

$$2(1 - r_t)\,\sigma_{m2} = 4\dot{\sigma}_{m2}s_{dx} - 2s_{dx}^2 \tag{44}$$

where

$$s_{dx} = (1/2)s_d(1 - r_t) \tag{45}$$

Then employing Eq. (30) for the damper, and introducing the end conditions from Eq. (39),

$$\dot{\sigma}_{m2} - \dot{\sigma}_{m1} = (1/S)(\dot{\sigma}_{d2} - \dot{\sigma}_{m1}) \tag{46}$$

$$\dot{\sigma}_{m2} + \dot{\sigma}_{m1} = -1/(\eta S)\,(\dot{\sigma}_{d2} + \dot{\sigma}_{m1}) \tag{47}$$

and eliminating $\dot{\sigma}_{d2}$ from these expressions

$$\dot{\sigma}_{m1}/\dot{\sigma}_{m2} = -S(1 + \eta)/(2 + \eta S - S) \tag{48}$$

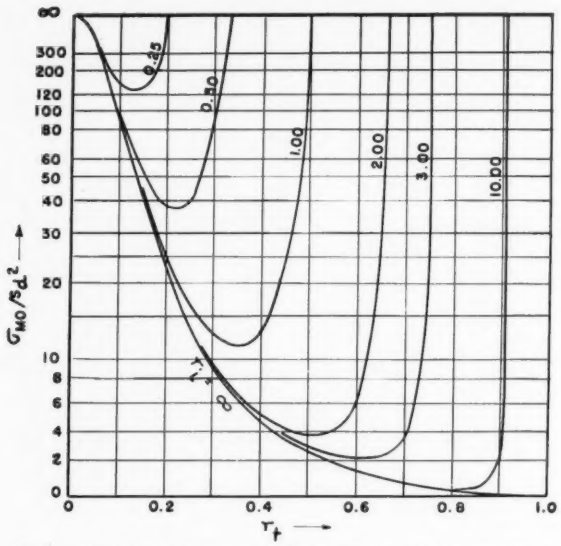

FIG. 6. Variation of amplitude of limit cycle with friction torque and inertia ratios.

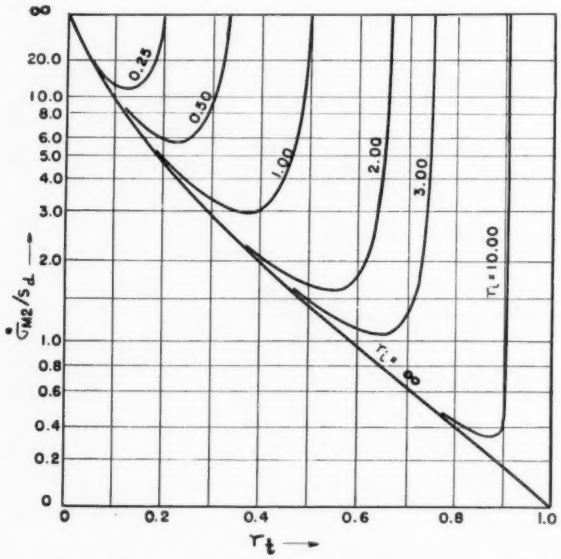

FIG. 7. Variation of maximum velocity in limit cycle with friction torque and inertia ratios.

Let

$$b = -S(1 + \eta)/(2 + \eta S - S) \tag{49}$$

It is now possible to solve for $\dot{\sigma}_{m2}$ by combining Eqs. (42), (44), and (48). The result can be expressed as

$$ax^2 - 4x + 2 = 0 \tag{50}$$

where

$$x = \dot{\sigma}_{m2}/s_{dx} \tag{51}$$

$$a = (1 - \eta)(1 - b^2) \tag{52}$$

From Eq (50)

$$x = 2/a \pm [(2/a)^2 - (2/a)]^{1/2} \tag{53}$$

It can be shown that in Eq. (53) only the root obtained by taking the positive sign in the sum is of physical significance.

Amplitude and Period of Oscillation

The maximum velocity reached by the servo in steady-state oscillation is given by Eq. (53). The maximum amplitude is attained at point 0, indicated in Fig. 2. Between points *2* and *0*, from Eq. (28),

$$\sigma_{m2} - \sigma_{m0} = \dot{\sigma}_{m2}^2/(1 - r_t) \tag{54}$$

Substituting Eq. (44) into Eq. (54)

$$-y = (x - 1)^2 \tag{55}$$

where

$$\left.\begin{aligned} x &= \dot{\sigma}_{m2}/s_{dx} \\ y &= \sigma_{m0}(1 - r_t)/s_{dx}^2 \end{aligned}\right\} \tag{56}$$

To obtain the period P, note that

$$P/2 = s_{12} + s_{23} \tag{57}$$

Applying Eq. (25)

$$\dot{\sigma}_{m2} - \dot{\sigma}_{m1} = (1/2)(1 - r_t)s_{12} \tag{58}$$

$$\dot{\sigma}_{m3} - \dot{\sigma}_{m2} = -(1/2)(1 + r_t)s_{32} \tag{59}$$

and combining Eqs. (58), (59), and (48),

$$P/s_d = 2x[(1 + \eta) - b(1 - \eta)] \tag{60}$$

or also

$$P/s_d = 4x(1 - br_t)/(1 + r_t) \tag{61}$$

Choice of Optimum r_t

For a given r_t and r_t, therefore, the amplitude of oscillation is proportional to the square of the time lag, while the period and maximum velocity are both proportional to the time lag. In order to show how these characteristics depend upon r_t and r_t, Figs. 6 to 8 have been prepared, giving the amplitude, maximum velocity, and period of steady-state oscillation as functions of r_t and r_t.

Fig. 6 shows clearly that there is a value of r_t for any given r_t for which the amplitude of steady-state oscillation is a minimum. It is interesting to note that this optimum value depends only upon r_t and not upon the value of the time lag.

The curves for $r_t = \infty$ are the same as those that would be obtained if the input to the servo were stationary and a friction damping torque were obtained by locking the flywheel of Fig. 1 to ground. This case was treated by Hazen,[5] who commented that "from the point of view of making the amplitude of oscillation small, a servo with Coulomb friction acting on the output is preferable to one with viscous friction," but that this applied "only to the condition with a substantially stationary input."

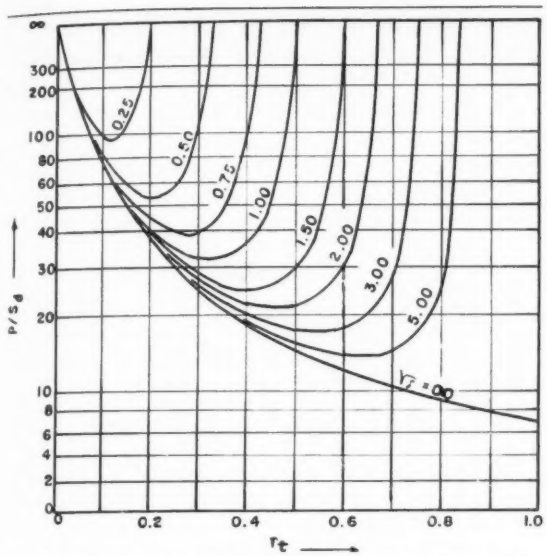

FIG. 8. Variation of period of limit cycle with friction torque and inertia ratios.

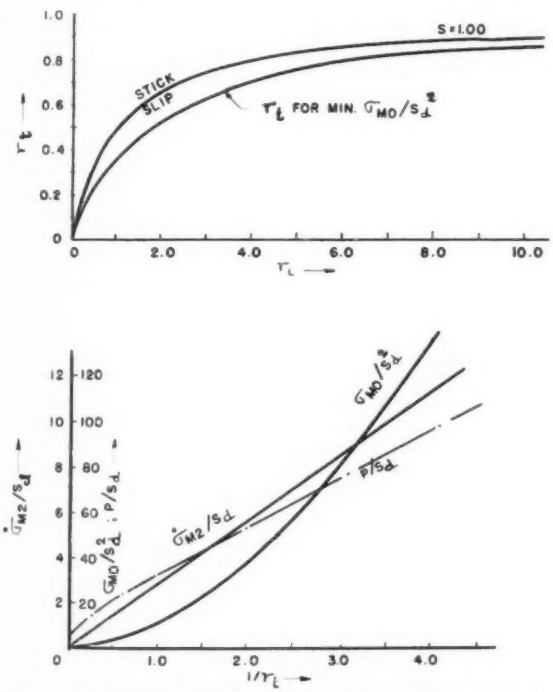

FIG. 9. Optimum relationship between friction torque, inertia ratios, and corresponding amplitudes and periods of limit cycles.

The use of the flywheel coupled to the servo by coulomb friction preserves the advantage of dry friction damping even in the case of moving input. Indeed, as shown by the curves of Fig. 6, as long as the optimum value of r_t is not exceeded, the friction-coupled flywheel provides a damping action for the servo with constant-velocity input which is nearly as efficient as the same friction torque applied to a servo with stationary input in the manner considered by Hazen.

Fig. 9 shows the relationship between r_t and r_i for minimum amplitude of steady-state oscillation and the way in which the maximum amplitude and velocity of oscillation and the period then depend on r_t. In general, the amplitude of oscillation can be made as small as desired by making the inertia of the flywheel large. Increasing the inertia of the flywheel while maintaining the optimum torque adjustment, however, reduces the maximum acceleration of the servo and also increases the settling time required for the initial transient to disappear.

The curves of Figs. 6, 7, and 8 apply only to the limiting steady-state oscillation and do not describe the process by which the transient motion converges to this steady state. To show the fundamental difference in transient response when the damper is free or fixed,

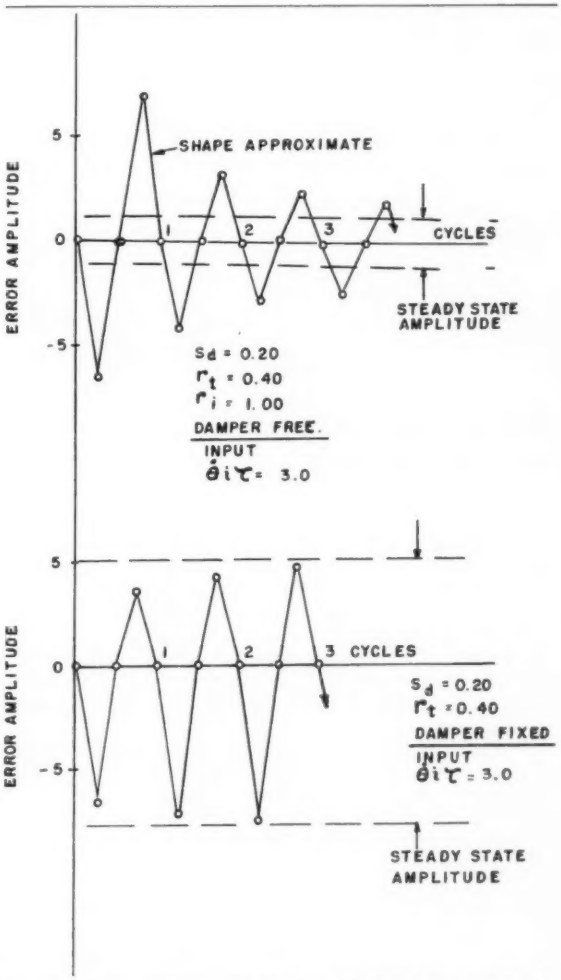

FIG. 10. Transient response of servo with free damper and with fixed damper.

phase-plane trajectories similar to those of Figs. 3, 4, and 5 were constructed for a servo initially at rest, to which a constant velocity input is suddenly applied.

Fig. 10a shows the variation of maximum error amplitude with number of cycles of oscillation when the damper is free to move in response to the friction coupling to the servo. Note that the abscissa is number of cycles rather than time. The period of oscillation actually varies with the amplitude, in general decreasing as the amplitude decreases.

Fig. 10b shows the error amplitudes for the same servo with the damper fixed so that the flywheel cannot rotate. In the latter case, the amplitude increases to an extremely large value in the steady state, while, in the former, it reduces to a comparatively small value as the flywheel is brought up to the same average angular velocity as the servo input. In fact, with the damper fixed, it is necessary that the absolute velocity of the servo output change sign in order to obtain damping. This requirement makes the fixed damper unacceptable for most servomechanism applications. The friction-coupled flywheel, on the other hand, is a useful device regardless of the nature of servo input.

Conclusions

A method has been developed for the analysis of the transient and steady-state motion of a clutch-type servomechanism with friction flywheel damper. It is shown that a steady-state oscillation of stable amplitude exists. The amplitude is determined by time lag in the control, by the ratio of friction torque to driving torque, and by the ratio of damper inertia to serve inertia. Charts are presented showing the amplitude and period of the steady-state motion as functions of the parameters describing the servo and damper.

References

[1] Timoshenko, S., *Vibration Problems in Engineering*, pp. 274–276; D. Van Nostrand Company, Inc., New York, 1937.

[2] Den Hartog, J. P., *Mechanical Vibrations*, pp. 230–236; McGraw-Hill Book Company, Inc., New York, 1934.

[3] Lear, William P., *Remote and Automatic Electric Control for Aircraft*, Journal of the Franklin Institute, Vol. 238, No. 1, pp. 9–35, July, 1944.

[4] Gille, W. H., and Kutzler, R. J., *Application of Electronics to Aircraft Flight Control*, Aeronautical Engineering Review, Vol. 4, No. 5, pp. 5–15, May, 1945.

[5] Hazen, Harold L., *Theory of Servo-Mechanisms*, Journal of the Franklin Institute, Vol. 218, No. 3, pp. 279–331, September, 1934.

[6] Weiss, Herbert K., *Analysis of Relay Servomechanisms*, Journal of the Aeronautical Sciences, Vol. 13, No. 7, pp. 364–376, July, 1946.

[7] Minorsky, N., *Non-Linear Mechanics;* Edwards Bros., Inc., Ann Arbor, 1947.

[8] MacColl, L. A., *Fundamental Theory of Servomechanisms*; Van Nostrand Company, Inc., New York, 1945.

Summary of Recent Experimental Investigations in the N.O.L. Hyperballistics Wind Tunnel

(*Continued from page 670*)

phenomena are noted with condensation at N.O.L. and in the C.I.T. tunnel.[6]

References

[1] Dodge, B. F., and Dunbar, A. K., *An Investigation of the Co-existing Liquid and Vapor Phases of Solutions of Oxygen and Nitrogen*, Jour. Am. Chem. Soc., Vol. 49, p. 591, 1927.

[2] Volmer, M., *Kinetik der Phasenbildung;* Verl. Steinkopff, Dresden and Leipzig, 1939.

[3] Wegener, P., *Experiments on the Influence of Temperature Gradient and Humidity on Condensation Shocks in Supersonic Wind Tunnels*, Phys. Review, Vol. 76, 2nd Series, No. 6, September, 1949.

[4] Becker, J. V., *Results of Recent Hypersonic and Unsteady Flow Research at the Langley Aeronautical Laboratory*, Jour. Appl. Physics, Vol. 21, p. 619, July, 1950.

[5] Stever, H. G., and Rathbun, K. C., *Theoretical and Experimental Investigation of the Condensation of Air in Hypersonic Wind Tunnels*, M.I.T. Aero. Eng. Dept., Final Report, N.A.C.A. Contract NAw 5713, October, 1950.

[6] Nagamatsu, H. J., *Results of Recent Hypersonic Flow Research in the Army Ordnance-CIT Hypersonic Wind Tunnel*, Am. Phys. Soc. Meeting, May, 1950.

[7] Burcher, M. A., *Compressible Flow Tables for Air* N.A.C.A. T.N. No. 1592, August, 1948.

[8] Liepmann, H. W., and Puckett, A. E., *Introduction to Aerodynamics of a Compressible Fluid*, p. 77; New York, 1947.

[9] Wegener, P., Stollenwerk, E., Reed, S., and Lundquist, G., *Condensation in Hypersonic Flow*, in preparation for Jour. of Appl. Phys.

[10] Reed, S., *Some Aspects of Air Condensation in Hypersonic Wind Tunnels*, Am. Phys. Soc. Meeting, February, 1951.

[11] Moeckel, W. E., and Connors, J. F., *Charts for the Determination of Supersonic Air Flow Against Inclined Planes and Axially Symmetric Cones*, N.A.C.A. T.N. No. 1373, July, 1947.

[12] Head, R., *Investigation of Spontaneous Condensation Phenomena*, GALCIT Dissertation, 1949.

[13] McLellan, C. H., Williams, T. W., and Berkwith, I. E., *Investigation of the Flow Through a Single-State Two-Dimensional Nozzle in the Langley 11-Inch Hypersonic Tunnel*, N.A.C.A. T.N. No. 2223, December, 1950.

The Lift Distribution on Low Aspect Ratio Wings at Subsonic Speeds

H. R. LAWRENCE*

Cornell Aeronautical Laboratory, Inc.

SUMMARY

A systematic procedure is developed for obtaining approximate integral equations from the linearized theory of a lifting surface in a steady incompressible flow. This procedure leads to a system of classification of the various theories currently employed in the calculation of lift distribution[2, 3, 4, 7] and to a new theory for the chordwise lift distribution over wings of low aspect ratio. A certain duality between the high aspect ratio and low aspect ratio approximations is exhibited by this classification system. The following conclusions are established for the special case of a rectangular wing, but the results are believed to be generally applicable.

(1) There does not exist a low aspect ratio analog to the infinite aspect ratio theory.[1]

(2) The low aspect ratio analog to the Prandtl lifting-line theory[7] is the Jones low aspect ratio theory.[2]

(3) The low aspect ratio analog to the Weissinger lifting-line theory[3] is the present theory.

(4) The Weissinger lifting-line theory[3] and the present theory are unique among the theories under discussion in that they both approach the exact lifting surface theory when the aspect ratio goes to infinity or to zero.

The theory developed for a rectangular wing is extended to more general plan forms. By reinterpreting the integral equation, the case of wing-body combinations and more general configurations may be solved. However, the régime of validity for these extensions of the theory must be established by comparison with test data.

The integral equation for chordwise lift distribution may be used in conjunction with the spanwise lift distributions of Jones and Spreiter to estimate pressures on the configuration only for symmetric spanwise loadings. In the antisymmetric case, an integral equation for the chordwise distribution of rolling moment may be used in conjunction with the antisymmetric Jones or Spreiter spanwise lift distribution to estimate pressures. The required integral equation for rolling moments is developed by a procedure analogous to the symmetric case.

A numerical method for solving the integral equations arising in the present theory is discussed and applied to calculations of the chordwise pressure distribution, lift curve slope, aerodynamic center, and damping in roll of rectangular and delta wings for the aspect ratio range from 0 to 4. The results are compared with test data and show satisfactory agreement.

The results of the present theory as applied to low aspect ratio wings are valid only for small angles of attack. In reference 13, a method is proposed for taking account of the nonlinear lift curve of low aspect ratio wings. A viscous cross-flow drag term $2\alpha^2$ is added to the lift coefficient and is assumed to act at the plan-form centroid of area. The present theory may be extended to large angles of attack by making use of this procedure.

Presented at the Supersonic Aerodynamics Session, Nineteenth Annual Meeting, I.A.S., New York, January 29–February 1, 1951.

* Assistant Head, Aerodynamic Research Department.

INTRODUCTION

Status of Low Aspect Ratio Theory

A METHOD FOR ESTIMATING AERODYNAMIC FORCES is necessary in the design of aircraft or missiles with low aspect ratio wings or tails. There exist, at present, four methods useful in predicting the air forces on low aspect ratio wings. Bollay[10] has treated the case of a rectangular wing of low aspect ratio. By making appropriate assumptions as to the location of the trailing vortices and the lift distribution, a nonlinear relationship between lift and angle of attack which agrees with test data was obtained. This method does not predict lift distributions and is not readily generalized to other plan forms. Weinig[11] has also treated the rectangular wing by a rather obscure procedure involving cascade theory. By making use of the assumption that the momentum of the stream intercepted by the streamwise projection of the wing is transferred to the wing, a nonlinear relation between

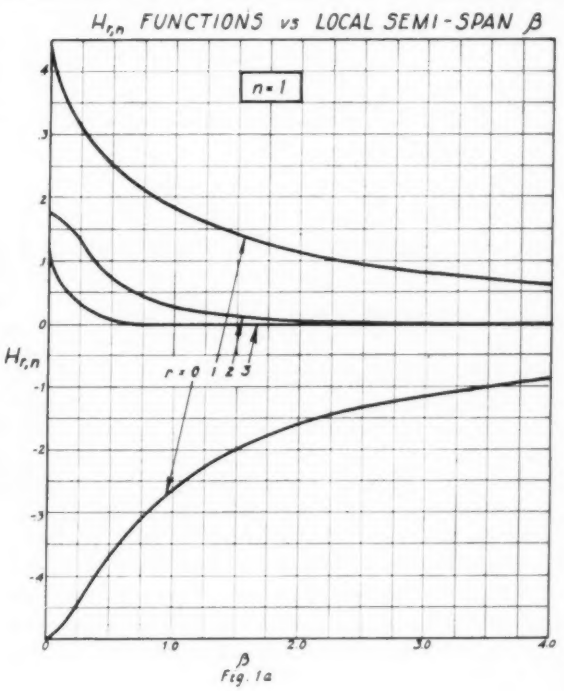

Fig. 1a

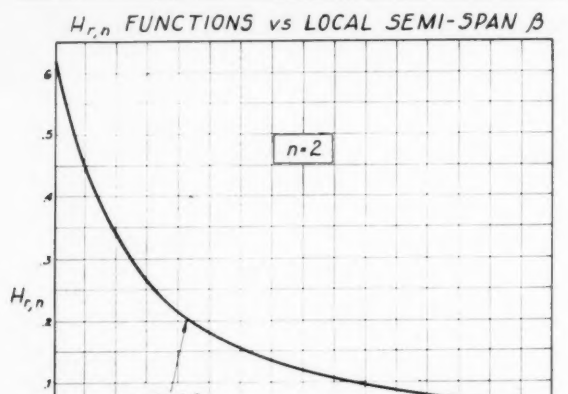

Fig. 1b

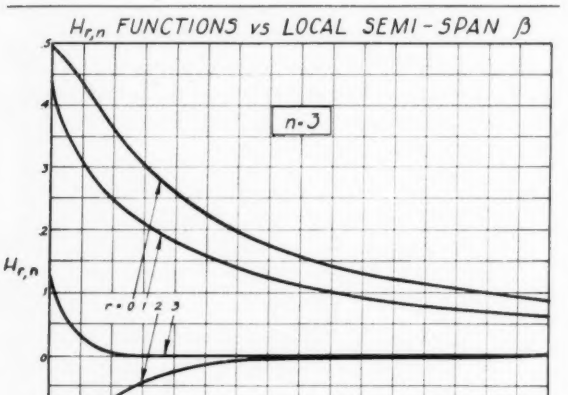

Fig. 1c

the lift and angle of attack was obtained. The results agree with test data over the entire range of aspect ratio. However, the lift distribution cannot be calculated, and the results do not appear to be readily generalized to more complex plan forms. A method for predicting the lift distribution on extremely low aspect ratio wings with unswept trailing edges has been developed by Jones.[2] For small angles of attack, the theory agrees well with test data. Since this theory predicts a linear relationship between lift coefficient and angle of attack, the results diverge from test data at higher angles. A method for estimating aerodynamic forces applicable to all plan forms has been developed by Weissinger.[3] The derivation of the Weissinger theory from lifting surface theory has been clarified by Reissner.[8] The spanwise lift distribution predicted by this theory is in good agreement with test data for all aspect ratios at low angles of attack and for high aspect ratios at unstalled angles. The chordwise lift distribution does not agree with test data for low aspect ratio plan forms. Since the Weissinger theory leads to a linear relation between lift and angle of attack, the agreement with test data on low aspect ratio wings at high angles is not to be expected.

Desired Improvements in Low Aspect Ratio Theory

An investigation of methods for computing the lift distribution on low aspect ratio wings has led to a new avenue of approach to this problem. The difficulties with present theories may be summarized as follows: The theories of Bollay[10] and Weinig[11] predict the nonlinear effects correctly but do not produce lift distributions and are restricted to rectangular wings. The theories of Jones[2] and Weissinger[3] predict the spanwise lift distribution correctly but do not give accurate chordwise lift distribution and omit the nonlinearity in lift curve. A theory that predicts the chordwise lift distribution, is applicable to a large class of plan forms, and takes account of nonlinearity is required.

Summary of the Nonlinear Theory of Reference 13

A summary of the history, motivation, and results of reference 13 are presented below as background material. The investigation started with a comparison of the Bollay[10] and Weinig[11] theories with test data, which indicated that the Weinig theory was more accurate. Closer examination of the Weinig[11] theory established the fact that the cascade analogy and momentum terms were independent. The cascade analogy is used to establish a potential flow solution that gives a lift proportional to angle of attack. The momentum term, resulting from the assumption that a column of air equal in cross section to the streamwise projection of the wing is deflected downward, leads to a lift proportional to the square of the angle of attack. These considerations suggested the possibility of adding the nonlinear term obtained by Weinig to the linear potential theory approximations developed by Jones[2] and Weissinger.[3] The results of this combination of theories reproduced Weinig's results for rectangular wings. Application of this method to more general plan forms gave excellent correlation with test data. Furthermore, the spanwise lift distribution could now be estimated for wings of low aspect ratio. Although the results obtained thus far were encouraging, Weinig's method for obtaining the nonlinear term in the lift curve did not appear convincing from a physical point of view. An alternate method for obtaining a nonlinear term was suggested by Allen's work on slender bodies of revolution.

Allen[12] assumes that the lift on a slender body contains a nonlinear term, resulting from cross-flow viscous drag. Investigation indicated that better agreement with test data was obtained if, in computing the cross-flow drag, the streamwise Reynolds Number was used in place of the cross-flow Reynolds Number as proposed by Allen. There appear to be sound physical reasons for stating that the boundary-layer state is determined by the streamwise, rather than the cross-flow, Reynolds Number.

If the cross-flow drag concept is applied to low aspect ratio wings, the cross-flow drag coefficient must be determined from some hypothesis as to the viscous cross flow. A viscous drag coefficient of two, corresponding to a plate of very low aspect ratio, was found to give precisely the Weinig nonlinear term. Further work of a fundamental nature is required to establish the physical validity of either the Weinig or the nonlinear term of reference 13 for low aspect ratio wings.

For engineering purposes, the nonlinear effects observed when testing low aspect ratio wings may be predicted by adding a term $2\alpha^2$ to the potential theory solution for lift coefficient as a function of angle of attack α and by assuming this lift to be uniformly distributed over the plan form. This leads to a great simplification in the search for an adequate theory for low aspect ratio wings. The Weissinger[3] theory provides a method for computing the spanwise lift distribution, so that only a method for computing chordwise lift distributions is required.

Linear Theory of Low Aspect Ratio Wings

A new method for computing the lift distribution on low aspect ratio wings is developed in this report. This method represents a generalization of the Jones theory and is applicable throughout the range of aspect ratio. The Weissinger[3] theory assumes the chordwise lift distribution corresponding to high aspect ratio and computes the spanwise lift distribution. The present theory assumes the spanwise lift distribution corresponding to low aspect ratio and computes the chordwise lift distribution. The slope of the lift curve computed by these two widely divergent theories leads to almost identical results over the entire range of aspect ratio 0 to ∞. The choice of theory would then depend on whether accurate values for the spanwise or chordwise lift distribution are required. If a complete lift distribution is required, the two theories can be combined in an appropriate manner.

List of Symbols

U	= velocity of free stream
$u(x, y)$	= parametric lift per unit area
x, y, z	= Cartesian coordinates of point of observation
ξ, η	= Cartesian coordinates of source point
$p(x, y)$	= $2\rho U^2 u(x, y)$ = lift per unit area
ρ	= free-stream density

VARIATION OF LIFT SLOPE WITH ASPECT RATIO FOR A RECTANGULAR WING

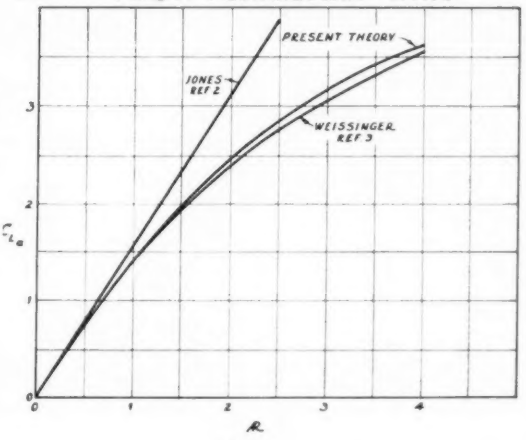

Fig. 2

VARIATION OF LIFT SLOPE WITH ASPECT RATIO FOR A TRIANGULAR WING

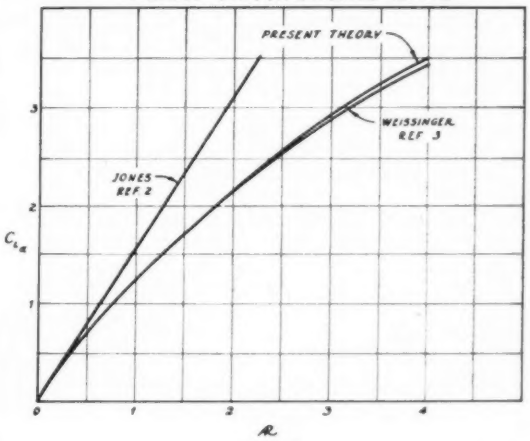

Fig. 3

VARIATION OF CENTER OF PRESSURE WITH ASPECT RATIO

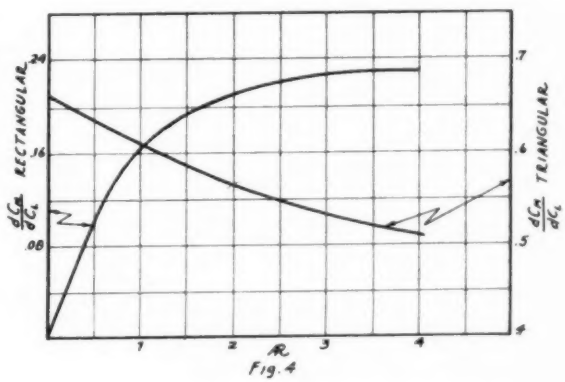

Fig. 4

$\phi(x, y, z)$ = perturbation potential
$-w(x, y)$ = local slope of airfoil in stream direction
b = wing semispan
c = wing semichord
$2\beta(x)$ = local wing span
$h(y)$ = see Eq. (10)
H = $2\rho U^2 h$ = lift per unit span for wing of infinite aspect ratio
$l(y)$ = $\int_{-c}^{c} d\xi u(\xi, y)$ = parametric lift per unit span
$L(y)$ = $2\rho U^2 l(y)$ = lift per unit span
$k(x)$ = see Eq. (21)
$K'(x)$ = $2\rho U^2 k'(x)$ = Jones lift per unit chord
$g'(x)$ = see Eq. (30)
$G'(x)$ = $2\rho U^2 g'(x)$ = lift per unit chord
$H(\theta\beta\tau)$ = see Eq. (50)
$H_{rn}(\beta)$ = see Eq. (60)
S = wing area
A.R. = aspect ratio
$e'(x)$ = see Eq. (45)
$E'(x)$ = $2\rho U^2 e'(x)$ = Jones rolling moment per unit chord
$m'(x)$ = see Eq. (46)
$M'(x)$ = $2\rho U^2 m'(x)$ = rolling moment per unit chord

(I) Integral Equation for a Lifting Surface

Eq. (62) of reference 1 will be used as a starting point for this investigation. With the notation

$$r^2 = (x - \xi)^2 + (y - \eta)^2 + z^2$$

Eq. (62) may be written

$$\phi_z(x, y, z) = -\frac{1}{2\pi}\int_{\infty}\int d\xi\, d\eta\, u(\xi, \eta)\left\{\frac{x - \xi}{r^3} + \frac{\partial}{\partial y}\left[\frac{(x - \xi)(y - \eta)}{r[z^2 + (y - \eta)^2]} + \frac{y - \eta}{z^2 + (y - \eta)^2}\right]\right\} \tag{1}$$

The airfoil is assumed to lie in the plane $z = 0$ with local angle of attack $w(x, y)$. $\phi_z(x, y, z)$ represents the z component of the perturbation velocity at the point (x, y, z), and $u(\xi, \eta)$ is proportional to the jump in the x component of the perturbation velocity on crossing the plane $z = 0$. The lift per unit area $p(x, y)$ is given in terms of $u(x, y)$ by the expression

$$p(x, y) = 2\rho U^2 u(x, y) \tag{2}$$

Eq. (1) may be rewritten in the following forms:

$$\left.\begin{aligned}\phi_z(x, y, z) &= -\frac{1}{2\pi}\int_{\infty}\int d\xi\, d\eta\, u(\xi, \eta)\frac{\partial}{\partial y}\left\{\frac{(x - \xi)(y - \eta)}{r[z^2 + (x - \xi)^2]} + \frac{(x - \xi)(y - \eta)}{r[z^2 + (y - \eta)^2]} + \frac{y - \eta}{z^2 + (y - \eta)^2}\right\}\\ \phi_z(x, y, z) &= -\frac{1}{2\pi}\frac{\partial}{\partial y}\int_{\infty}\int d\xi\, d\eta\, u(\xi, \eta)\left[\frac{y - \eta}{z^2 + (y - \eta)^2}\left\{1 + \frac{(x - \xi)(r^2 + z^2)}{r[z^2 + (x - \xi)^2]}\right\}\right]\end{aligned}\right\} \tag{3}$$

For the case of steady flow, $\phi_z(x, y, 0+) = -w(x, y)$ on the lifting surface and $u = 0$ over the remaining portion of the plane $z = 0$. Upon substituting these boundary conditions in Eq. (3), there results the integral equation

$$w(x, y) = \frac{1}{2\pi}\frac{\partial}{\partial y}\int_{R_a}\int d\xi\, d\eta\, \frac{u(\xi, \eta)}{y - \eta}\left[1 + \frac{\sqrt{(x - \xi)^2 + (y - \eta)^2}}{x - \xi}\right] \tag{4}$$

relating the unknown velocity $u(x, y)$ to the known angle of attack of the lifting surface $w(x, y)$. u is proportional to the lift per unit area and will be called the parametric lift per unit area.

(II) Infinite Aspect Ratio

The integral Eq. (4) may be solved for the case of infinite aspect ratio when the angle of attack is independent of the spanwise coordinate. Eq. (4) may then be written as follows:

$$w(x) = -\frac{1}{2\pi}\int_{-c}^{c} d\xi \int_{-\infty}^{\infty} d\eta\, u(\xi)\frac{\partial}{\partial \eta}\left[\frac{1}{y - \eta} + \frac{\sqrt{(x - \xi)^2 + (y - \eta)^2}}{(x - \xi)(y - \eta)}\right]$$

and, upon performing the integration over η,

$$w(x) = \frac{1}{\pi}\int_{-c}^{c}\frac{d\xi\, u(\xi)}{x - \xi} \tag{5}$$

Eq. (5) is the well-known infinite aspect ratio result. The solution of this equation for the parametric lift per unit span, h, is given in reference 4 as

$$h = \int_{-c}^{c} d\xi\, u(\xi) = \int_{-c}^{c} dx\, w(x) \sqrt{\frac{c+x}{c-x}} \tag{6}$$

The lift per unit span, H, is related to h by the expression

$$H = 2\rho U^2 h \tag{7}$$

(III) Prandtl Lifting-Line Theory

The case of a rectangular lifting surface is considered so as to simplify the analysis. Then Eq. (4) may be integrated by parts and written in the form

$$w(x, y) = \frac{1}{2\pi} \int_{-b}^{b} d\eta \int_{-c}^{c} d\xi\, u_\eta(\xi, \eta) \left[\frac{1}{y-\eta} \left(1 + \frac{\sqrt{(x-\xi)^2 + (y-\eta)^2}}{(x-\xi)} \right) \right] \tag{8}$$

The integral Eq. (8) will be satisfied on the average in the chordwise direction. This is achieved by multiplying Eq. (8) by a weighting factor and integrating over the chord. The weighting factor is chosen to be exact for a wing of infinite span. Multiplying Eq. (8) by $\sqrt{c+x}/\sqrt{c-x}$ and integrating over the chord, there results the equation

$$h(y) = \frac{1}{2\pi} \int_{-b}^{b} \frac{d\eta}{y-\eta} \int_{-c}^{c} d\xi\, u_\eta(\xi, \eta) \int_{-c}^{c} dx \sqrt{\frac{c+x}{c-x}} \left[1 + \frac{\sqrt{(x-\xi)^2 + (y-\eta)^2}}{(x-\xi)} \right] \tag{9}$$

where $h(y)$ is defined as follows:

$$h(y) = \int_{-c}^{c} dx\, w(x, y) \sqrt{\frac{c+x}{c-x}} \tag{10}$$

It will be noted that the definition of $h(y)$ is consistent with the interpretation of $h(y)$ as the parametric lift per unit span of a wing of infinite aspect ratio [cf. Eq. (6)].

Now an approximation based on the assumption of large aspect ratio is employed to simplify the integral Eq. (9). Consider the integral

$$J' = \int_{-c}^{c} dx \sqrt{\frac{c+x}{c-x}} \left[1 + \frac{\sqrt{(x-\xi)^2 + (y-\eta)^2}}{x-\xi} \right] \tag{11}$$

Since the aspect ratio is large, $|y-\eta|$ will, in general, be much larger than $|x-\xi|$. Hence, as a first approximation, the radical $\sqrt{(x-\xi)^2 + (y-\eta)^2}$ may be replaced by $|y-\eta|$. Then the integration over x may be performed, and Eq. (11) may be written

$$J_1' = \pi(c + |y-\eta|)$$

Upon substituting this result in Eq. (9) and making use of the definition for parametric lift per unit span $l(y)$,

$$l(y) = \int_{-c}^{c} d\xi\, u(\xi, y) \tag{12}$$

the integral Eq. (9) acquires the form

$$h(y) = \frac{1}{2} \int_{-b}^{b} d\eta \frac{dl}{d\eta} \left(\frac{c}{y-\eta} + \frac{|y-\eta|}{y-\eta} \right)$$

$$= l(y) + \frac{c}{2} \int_{-b}^{b} \frac{d\eta}{y-\eta} \frac{dl}{d\eta} \tag{13}$$

The lift per unit span $L(y)$ is defined in terms of the parametric lift per unit span by the relation

$$L(y) = 2\rho U^2 l(y) \tag{14}$$

Eq. (13) is the Prandtl lifting-line integral equation for a rectangular wing.

(IV) Jones Low Aspect Ratio Theory

The integral Eq. (4) may be solved for the Jones low aspect ratio case. For convenience, only the rectangular plan form will be considered. Then Eq. (4) may be replaced by Eq. (8) or

$$w(x, y) = \frac{1}{2\pi} \int_{-b}^{b} \frac{d\eta}{y-\eta} \int_{-c}^{c} d\xi\, u_\eta(\xi, \eta) \times \left[1 + \frac{\sqrt{(x-\xi)^2 + (y-\eta)^2}}{x-\xi} \right] \tag{8}$$

For sufficiently low aspect ratio, the radical $\sqrt{(x-\xi)^2 + (y-\eta)^2}$ may be replaced by $|x-\xi|$. Then Eq. (8) may be simplified to the form

$$w(x, y) = \frac{1}{\pi} \int_{-b}^{b} \frac{d\eta}{y-\eta} \phi_\eta(x, \eta) \tag{15}$$

where $\phi(x, y)$ is defined as follows:

$$\phi(x, y) = \int_{-c}^{x} d\xi\, u(\xi, y) \tag{16}$$

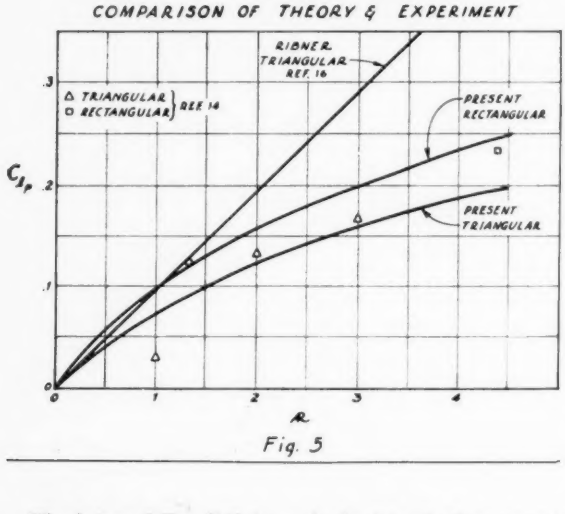

Fig. 5

The integral Eq. (15) is equivalent to the low aspect ratio theory of references 2 and 5. A solution of Eq. (15) is given by the formula[5]

$$\phi_y(x, y) = \frac{-1}{\pi\sqrt{b^2 - y^2}} \int_{-b}^{b} \frac{d\eta\, w(x, \eta)\sqrt{b^2 - \eta^2}}{y - \eta} \tag{17}$$

In the case where w is independent of y, Eq. (17) may be integrated to give the familiar result of Jones's low aspect ratio theory for a flat plate,

$$\phi(x, y) = w(x)\sqrt{b^2 - y^2} \tag{18}$$

The lift per unit chord $K'(x)$ and the parametric lift per unit chord $k'(x)$ are defined as follows:

$$\left.\begin{aligned} k'(x) &= \frac{dk}{dx} = \int_{-b}^{b} dy\, u(x, y) \\ K'(x) &= \frac{dK}{dx} = 2\rho U^2 k'(x) \end{aligned}\right\} \tag{19}$$

It is assumed that k is zero at the leading edge of the plan form. The relation between ϕ and k is given by the formula

$$k(x) = \int_{-b}^{b} dy\, \phi(x, y) = -\int_{-b}^{b} dy\, y\phi_y(x, y) \tag{20}$$

where $\phi(x, \pm b)$ is assumed to vanish. Upon multiplying Eq. (17) by $(-y)$ and integrating over the span, the parametric lift $k(x)$ may be written in the form

$$k(x) = \int_{-b}^{b} dy\, w(x, y)\sqrt{b^2 - y^2} \tag{21}$$

It is important to note that the approximation made in the Prandtl lifting-line theory consists in replacing $\sqrt{(x - \xi)^2 + (y - \eta)^2}$ by $|y - \eta|$ and that the approximation of the Jones low aspect ratio theory replaces $\sqrt{(x - \xi)^2 + (y - \eta)^2}$ by $|x - \xi|$. Hence, these cases are closely analogous. It is rather curious that no approximation exists in the low aspect ratio case that corresponds to the case of infinite aspect ratio. The first approximation to a low aspect ratio wing leads to the Jones theory, which corresponds to the second approximation in the case of high aspect ratio (Prandtl lifting-line theory). The shortcomings of the Prandtl theory and a method of improving the theory will be taken up next.

(V) Weissinger Lifting-Line Theory

There is no reason to believe *a priori* that the high aspect ratio lifting-line theory can be applied at low aspect ratio. However, a lifting-line theory that is correct in the limit as the aspect ratio approaches zero would be expected to give fair results throughout the aspect ratio range. Such is the case for the Weissinger theory. A procedure for developing the Prandtl and Weissinger theories similar to that employed in this paper was presented earlier by Reissner.[8] Consider

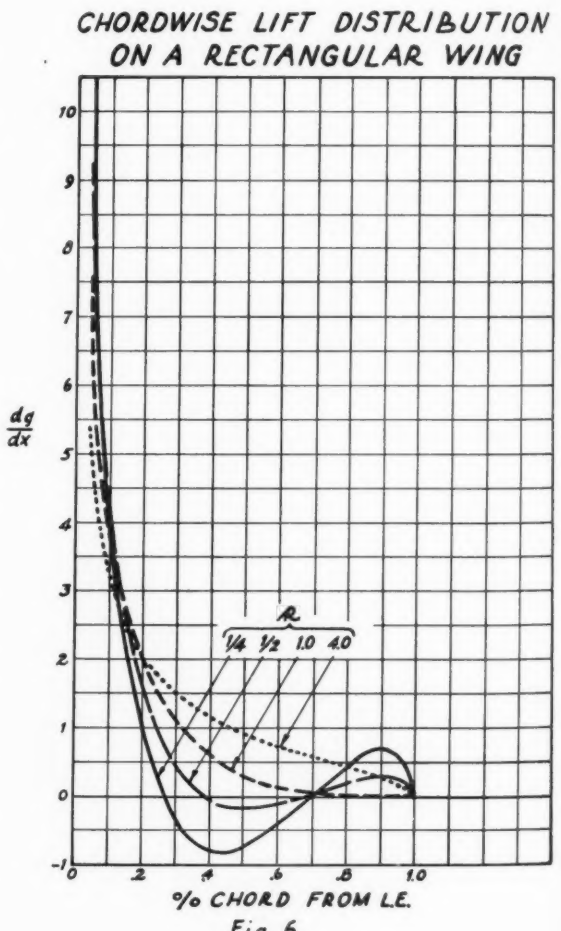

Fig. 6

first the limiting case approached by the Prandtl lifting-line integral Eq. (13) as the aspect ratio approaches 0. Making use of the definition (10) for $h(y)$, Eq. (13) may be written as

$$\int_{-c}^{c} d\left(\frac{x}{c}\right) w(x, y) \sqrt{\frac{1 + (x/c)}{1 - (x/c)}} = \frac{1}{2} \int_{-b}^{b} d\eta \frac{dl}{d\eta} \left[\frac{1 + (|y - \eta|/c)}{y - \eta}\right]$$

Upon transforming the integral on the left by the substitution $\lambda = x/c$ and noting that $|y - \eta|/c$ becomes negligible compared to unity as c approaches infinity, the limiting form as $c \to \infty$ of the above integral equation may be written as

$$\int_{-1}^{1} d(\lambda) w(\lambda c, y) \sqrt{\frac{1 + \lambda}{1 - \lambda}} = \frac{1}{2} \int_{-b}^{b} \frac{d\eta}{y - \eta} \frac{dl}{d\eta}$$

If w is independent of x, the above equation becomes

$$2\pi w(y) = \int_{-b}^{b} \frac{d\eta}{y - \eta} \frac{dl}{d\eta} \tag{22}$$

Eq. (22) represents the limiting form of the Prandtl lifting-line integral equation as the aspect ratio becomes small.

The integral Eq. (15) representing the Jones low aspect ratio theory is rigorously correct in the limiting case of low aspect ratio.

Making use of the relation $l(y) = \phi(c, y)$, the integral Eq. (15) may be written

$$\pi w(y) = \int_{-b}^{b} \frac{d\eta}{y - \eta} \frac{dl}{d\eta} \tag{23}$$

where it is assumed that w is independent of x. A comparison of the correct result for low aspect ratio given by Eq. (23) with the low aspect ratio limiting form of the Prandtl lifting-line theory given in Eq. (22) shows that the Prandtl integral equation is in error by a factor of two.

The Weissinger improvement on the Prandtl theory is found by consideration of Eq. (11). Instead of approximating to the radical $\sqrt{(x - \xi)^2 + (y - \eta)^2}$ by $|y - \eta|$, a more accurate approximation $\sqrt{(y - \eta)^2 + c^2}$ is used. Evaluating the integral in Eq. (11) with the above approximation leads to the result

$$J_2' = \pi\left[c + \sqrt{(y - \eta)^2 + c^2}\right]$$

which may be substituted into Eq. (9) to give the Weissinger integral equation

$$h(y) = \frac{1}{2} \int_{-b}^{b} d\eta \frac{dl}{d\eta} \left[\frac{c + \sqrt{c^2 + (y - \eta)^2}}{y - \eta}\right] \tag{24}$$

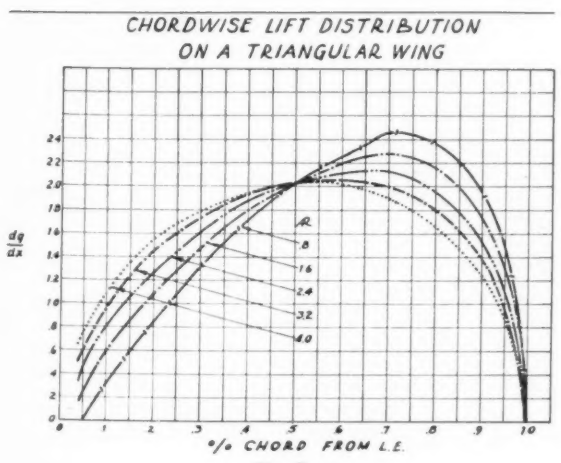

Fig. 7

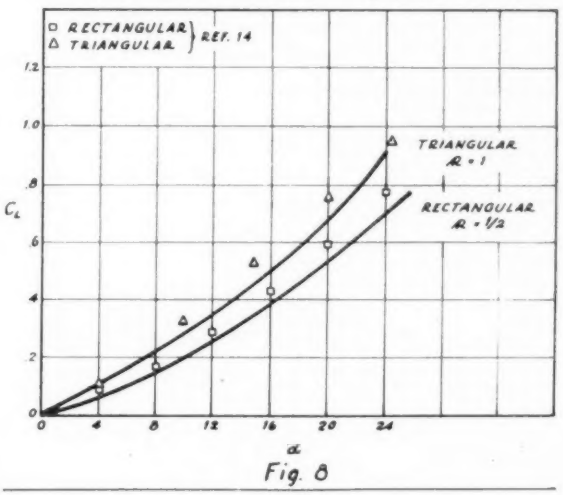

Fig. 8

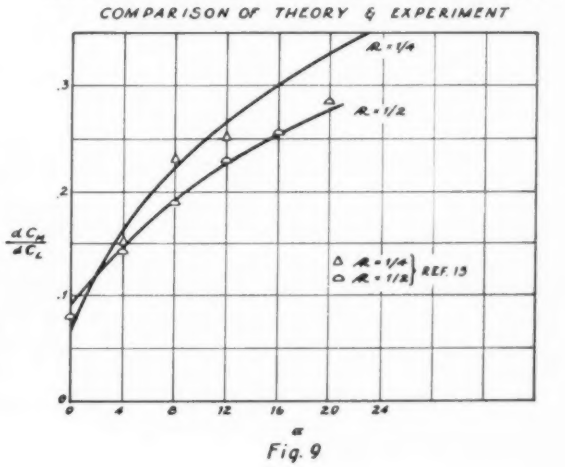

Fig. 9

or

$$h(y) = l(y) + \frac{1}{2}\int_{-b}^{b} d\eta \frac{dl}{d\eta} \times \left[\frac{c + \sqrt{c^2 + (y-\eta)^2} - |y-\eta|}{y-\eta}\right] \quad (24.1)$$

As in the Prandtl case, the limiting form of Eq. (24) is easily obtained as the aspect ratio becomes small, and the result is identical with Eq. (23). Thus, the Weissinger theory leads to the correct limiting case as the aspect ratio goes to zero.

(VI) A Low Aspect Ratio Approximation

In view of the background material presented, a method of improving the Jones theory is obvious. The weighting factor $\sqrt{b^2 - y^2}$ obtained from Eq. (21) will be used to satisfy Eq. (4) on the average in the spanwise direction. The Eq. (21) ensures that the integral equation will be satisfied exactly in the spanwise direction as the aspect ratio approaches 0. Multiplying Eq. (4) by $\sqrt{b^2 - y^2}$ and integrating over the span, the following result is obtained for a rectangular wing:

$$k(x) = \frac{1}{2\pi}\int_{-b}^{b} dy \sqrt{b^2 - y^2} \frac{\partial}{\partial y}\int_{-c}^{c} d\xi \int_{-b}^{b} d\eta \frac{u(\xi,\eta)}{y-\eta}\left[1 + \frac{\sqrt{(x-\xi)^2 + (y-\eta)^2}}{x-\xi}\right] \quad (25)$$

where $k(x)$ is defined in Eq. (21). After integrating by parts with respect to y and interchanging the order of integration, Eq. (25) becomes

$$k(x) = \frac{1}{2\pi}\int_{-c}^{c} d\xi \int_{-b}^{b} d\eta\, u(\xi,\eta) \int_{-b}^{b} \frac{dy\, y}{\sqrt{b^2 - y^2}}\left(\frac{1}{y-\eta}\right)\left[1 + \frac{\sqrt{(x-\xi)^2 + (y-\eta)^2}}{x-\xi}\right] \quad (26)$$

Consider the last integral on the right of Eq. (26),

$$J = \int_{-b}^{b} \frac{dy\, y}{(y-\eta)\sqrt{b^2 - y^2}} \times \left[1 + \frac{\sqrt{(x-\xi)^2 + (y-\eta)^2}}{x-\xi}\right] \quad (27)$$

For sufficiently low aspect ratio, the radical $\sqrt{(x-\xi)^2 + (y-\eta)^2}$ may be approximated by $|x-\xi|$. Then J may be evaluated as

$$J_1 = \pi\{1 + [|x-\xi|/(x-\xi)]\} \quad (27.1)$$

and, upon substituting this result in Eq. (26), there results

$$k(x) = \int_{-b}^{b} d\eta\, \phi(x,\eta) \quad (28)$$

Comparing Eq. (28) with Eq. (20), it is evident that this approximation leads again to the Jones result. This analysis bears out the assertion that the Jones theory for low aspect ratio wings is the analog of the Prandtl lifting-line theory for wings of high aspect ratio.

It is natural at this point to follow along on the analogy between low and high aspect ratio theories by trying the approximation

$$\sqrt{(x-\xi)^2 + (y-\eta)^2} = \sqrt{(x-\xi)^2 + b^2}$$

as an improvement over the approximation

$$\sqrt{(x-\xi)^2 + (y-\eta)^2} = |x-\xi|$$

Then the integral J may be evaluated as

$$J_2 = \pi\{1 + [\sqrt{(x-\xi)^2 + b^2}/(x-\xi)]\} \quad (29)$$

Upon introducing the parametric lift per unit chord $g'(x)$ and the lift per unit chord $G'(x)$ defined as follows:

$$\left.\begin{aligned} g'(x) &= \int_{-b}^{b} d\eta\, u(x,\eta) \\ G'(x) &= 2\rho U^2 g'(x) \end{aligned}\right\} \quad (30)$$

and substituting the result, Eq. (29), into Eq. (26), the following integral equation is obtained:

$$k(x) = \frac{1}{2}\int_{-c}^{c} d\xi\, g'(\xi)\left[1 + \frac{\sqrt{(x-\xi)^2 + b^2}}{x-\xi}\right] \quad (31)$$

$$k(x) = g(x) + \frac{1}{2}\int_{-c}^{c} d\xi\, g'(\xi) \times \left[\frac{\sqrt{(x-\xi)^2 + b^2} - |x-\xi|}{x-\xi}\right] \quad (32)$$

Here, $k(x)$ is defined by Eq. (21). The resemblance between Eqs. (31) and (32) and the Weissinger integral Eqs. (24) and (24.1) is evident.

It is of interest to compute the limiting form of Eq. (31) as the aspect ratio becomes large. For simplicity, the case where w is independent of x is considered. Then, upon integrating Eq. (21), the integral Eq. (31) may be written

$$\frac{\pi b w}{2} = \frac{1}{2}\int_{-c}^{c} d\xi\, g'(\xi)\left\{\frac{1}{b} + \frac{\sqrt{1 + [(x-\xi)/b]^2}}{x-\xi}\right\}$$

and for sufficiently large values of b, Eq. (31) may be written as

$$bw = \frac{1}{\pi}\int_{-c}^{c} \frac{d\xi\, g'(\xi)}{x-\xi} \tag{32.1}$$

For a rectangular wing of sufficiently large aspect ratio, the lift per unit span is substantially constant. Hence, from Eq. (30), $g'(x) = 2bu(x)$, and substituting this result in the integral Eq. (32.1) leads to the following equation:

$$w(x) = \frac{1}{2\pi}\int_{-c}^{c} \frac{d\xi\, u(\xi)}{x-\xi} \tag{33}$$

Upon comparing Eqs. (33) and (5), it is seen that the integral Eq. (5) differs from the limiting form of Eq. (31) as the aspect ratio becomes large by a factor of two. It is believed that one great factor in the success of the Weissinger theory is the fact that it is correct in the limiting case of low aspect ratio. Hence, although Eq. (31) is probably an improvement on the Jones theory, it cannot be considered entirely satisfactory. An integral equation that eliminates this objection is developed in the next section.

(VII) Improved Low Aspect Ratio Theory

In order to obtain a better approximation to the integral J of Eq. (27), the integral is rewritten in the following forms:

$$J = \int_{-b}^{b} \frac{dy\, y}{(y-\eta)\sqrt{b^2-y^2}}\left(1 + \frac{|x-\xi|}{x-\xi}\right) + \int_{-b}^{b} \frac{dy\, y}{\sqrt{b^2-y^2}}\left[\frac{\sqrt{(x-\xi)^2+(y-\eta)^2} - |x-\xi|}{(x-\xi)(y-\eta)}\right] \tag{34}$$

$$J = \pi\left(1 + \frac{|x-\xi|}{x-\xi}\right) + \int_{-b}^{b} \frac{dy\, y}{(x-\xi)\sqrt{b^2-y^2}}\left[\frac{y-\eta}{\sqrt{(x-\xi)^2+(y-\eta)^2} + |x-\xi|}\right] \tag{35}$$

Now in Eq. (35), the approximation

$$\sqrt{(x-\xi)^2+(y-\eta)^2} \sim \sqrt{(x-\xi)^2+b^2}$$

is introduced. It will be noted that approximation to the radical by $\sqrt{(x-\xi)^2+b^2}$ in Eq. (35) leads to a different result than the same approximation in Eq. (34). For example, when $0 < y-\eta < b$, the following inequalities apply:

$$\frac{\sqrt{(x-\xi)^2+b^2} - |x-\xi|}{y-\eta} > \frac{\sqrt{(x-\xi)^2+(y-\eta)^2} - |x-\xi|}{y-\xi} =$$

$$\frac{y-\eta}{\sqrt{(x-\xi)^2+(y-\eta)^2} + |x-\xi|} > \frac{y-\eta}{\sqrt{(x-\xi)^2+b^2} + |x-\xi|}$$

With the above approximation, the integral expression for J may be evaluated as follows:

$$J_3 = \pi\left(1 + \frac{|x-\xi|}{x-\xi}\right) + \frac{\pi b^2}{2}\left[\frac{1}{\sqrt{(x-\xi)^2+b^2} + |x-\xi|}\right]\frac{1}{(x-\xi)} \tag{36}$$

$$J_3 = \frac{\pi}{2}\left(1 + \frac{|x-\xi|}{x-\xi}\right) + \frac{\pi}{2}\left[1 + \frac{\sqrt{(x-\xi)^2+b^2}}{x-\xi}\right] \tag{37}$$

Upon comparing Eq. (37) with Eqs. (27.1) and (29), it is seen that the approximation J_3 represents the average of the Jones and the first improved approximation

$$J_3 = (1/2)(J_1 + J_2) \tag{38}$$

The expression, Eq. (38), for J_3 is substituted in the integral Eq. (25) to give the second improved low aspect ratio integral equation

$$k(x) = \frac{1}{2}\, g(x) + \frac{1}{4}\int_{-c}^{c} d\xi\, g'(\xi) \left\{1 + \frac{\sqrt{(x-\xi)^2 + b^2}}{x-\xi}\right\} \tag{39}$$

By comparing Eq. (39) with Eq. (32), it is evident that Eq. (39) reduces to the following form as the aspect ratio becomes large:

$$2bw = \frac{1}{\pi}\int_{-c}^{c} \frac{d\xi g'(\xi)}{x-\xi} \tag{40}$$

when w is independent of x. From the comparison shown in Eqs. (32.1) to (33), it is clear that Eq. (40) does, in fact, represent a correct limiting case as the aspect ratio becomes large. Eq. (39) will be taken as the improved Jones theory integral equation; Eq. (32) will no longer be considered.

(VIII) More General Plan Forms

The integral Eq. (39) proposed as an improvement over the Jones theory for low aspect ratio wings has been developed thus far for rectangular plan forms. In the following section, this result will be generalized to other cases by means of further approximations where necessary.

Consider a plan form with a trailing edge normal to the undisturbed stream. This implies that the span is nondecreasing in the direction of the undisturbed stream. It is evident that Eq. (26) may be written without approximation as follows:

$$k(x) = \frac{1}{2\pi}\int_{-c}^{c} d\xi \int_{-\beta(\xi)}^{\beta(\xi)} d\eta\, u(\xi,\eta) \int_{-\beta(\xi)}^{\beta(\xi)} \frac{dy\, y}{\sqrt{\beta^2(x) - y^2}}\left[\frac{1}{y-\eta} + \frac{\sqrt{(x-\xi)^2 + (y-\eta)^2}}{(x-\xi)(y-\eta)}\right] \tag{42}$$

The approximation used in going from Eq. (35) to Eq. (39) consisted of replacing $\sqrt{(x-\xi)^2 + (y-\eta)^2}$ by $\sqrt{(x-\xi)^2 + b^2}$ in Eq. (35). It may be shown that the replacement of $\sqrt{(x-\xi)^2 + (y-\eta)^2}$ by $\sqrt{(x-\xi)^2 + \beta^2(x)}$ in Eq. (42), after transforming the radical to the denominator, leads to the proper generalization. Then, upon performing the indicated integrations, Eq. (42) is replaced by the approximate integral equation

$$k(x) = \frac{1}{2}\, g(x) + \frac{1}{4}\int_{-c}^{c} d\xi\, g'(\xi)\left[1 + \frac{\sqrt{(x-\xi)^2 + \beta^2(x)}}{x-\xi}\right] \tag{43}$$

This generalization is equivalent to the assumption that each spanwise section acts like an element of rectangular wing with the local span $2\beta(x)$ and chord $2c$.

The definition of $k(x)$ is altered slightly to the form

$$k(x) = \int_{-\beta(x)}^{\beta(x)} dy\, w(x,y)\sqrt{\beta^2(x) - y^2} \tag{44}$$

The application of this theory to more general plan forms may be carried out along the lines given above. However, for wings that are influenced by their wakes, even the Jones case becomes complicated.

A more general procedure can be evolved from an interpretation of the results obtained thus far. Eq. (43) gives a relation between the lift computed from the Jones theory $k(x)$ and the three-dimensional lift $g(x)$. $k(x)$ may be considered as two-dimensional lift, since it depends only on the geometry at the chordwise station x. If, now, $k'(x)$ is redefined as the two-dimensional parametric lift of the spanwise element, the integral Eq. (43) may still be expected to hold approximately. Now, however, the configuration may be a wing-body combination with the two-dimensional lift per unit span given by Spreiter[6] or a more general case. This idea is entirely analogous with the treatment of a wing nacelle as a region of low lift curve slope in the Prandtl lifting-line theory. The method appears to be more useful in the present context, since the two-dimensional lift may be computed by the Spreiter theory, whereas in the high aspect ratio case the two-dimensional lift was difficult to estimate. Of course, it will be necessary to determine how far this interpretation can be carried.

(IX) Improved Low Aspect Ratio Theory for Antisymmetric Case

The pressure distribution over a wing with a spanwise symmetric local angle of attack distribution may

be estimated by combining the parametric chordwise lift distribution $g'(x)$ determined from Eq. (39) with a spanwise lift distribution estimated by the methods of Jones[2] and Spreiter.[6] When the spanwise distribution of local angle of attack is antisymmetric, the chordwise lift distribution vanishes and the above method for estimating pressures is no longer applicable. However, when the chordwise distribution of rolling moment is known, the pressure distribution over the wing can be estimated for an antisymmetric local angle of attack distribution.

The procedure for obtaining an integral equation for the chordwise distribution of rolling moment is so closely parallel to the symmetric case that only an outline of the development will be presented.

Eq. (4) is multiplied by $-(1/2)y\sqrt{b^2 - y^2}$ and integrated over the span. The resulting integral equation when simplified by the approximation employed in Section (VII) leads to the following formula:

$$-\frac{1}{2}\int_{-b}^{b} dy\, y\sqrt{b^2 - y^2}\, w(x, y) = \frac{1}{4}\int_{-c}^{c} d\xi \left[1 + \frac{|x - \xi|}{x - \xi} + 1 + \frac{\sqrt{(x - \xi)^2 + b^2}}{x - \xi}\right] \int_{-b}^{b} d\eta\, \eta u(\xi, \eta)$$

By making use of the definitions

$$e(x) = -\frac{1}{2}\int_{-b}^{b} dy\, y\sqrt{b^2 - y^2}\, w(x, y) \tag{45}$$

$$m'(x) = \frac{dm}{dx} = \int_{-b}^{b} dy\, yu(x, y) \tag{46}$$

and performing an integration on ξ, the above equation may be written as

$$e(x) = \frac{1}{2}m(x) + \frac{1}{4}\int_{-c}^{c} d\xi\, m'(\xi)\left[1 + \frac{\sqrt{(x - \xi)^2 + b^2}}{x - \xi}\right] \tag{47}$$

It will be noted that Eq. (47) becomes identical to Eq. (39) when $k(x)$ and $g(x)$ are substituted for $e(x)$ and $m(x)$.

From the definition (46), $m'(x)$ may be called the parametric rolling moment per unit chord. Then $M'(x) = 2\rho u^2 m'(x)$ becomes the rolling moment per unit chord. It may be shown that $e'(x)$ defined in Eq. (45) represents the parametric rolling moment per unit chord given by the Jones low aspect ratio theory. The corresponding rolling moment per unit chord $E'(x)$ is given in terms of $e'(x)$ by the formula $E'(x) = 2\rho U^2 e'(x)$.

As in the symmetric case, the generalization to plan forms with a straight trailing edge is found by replacing b by $\beta(x)$ in Eqs. (45), (46), and (47), where $2\beta(x)$ is the local span. Since $e(x)$ represents the Jones low aspect ratio solution,[2, 5, 6] the integral Eq. (47) may be used for more general configurations, such as a wing-body case. As in the symmetric case, the range of validity of these approximations must be established by comparison with test data.

(X) Solution of the Integral Equation

A method for solving the integral Eq. (43) is presented below. It will be observed that the same procedure is applicable to the integral Eq. (47) and that a large portion of the numerical calculations is common to both equations. The integral Eq. (43) may be written in the form

$$4k(x) = 2g(x) + g(1) + \beta(x)\int_{-1}^{1} \frac{d\xi\, g'(\xi)}{x - \xi} + \int_{-1}^{1} d\xi\, g'(\xi)\left[\frac{\sqrt{(x - \xi)^2 + \beta^2(x)} - \beta(x)}{x - \xi}\right] \tag{48}$$

where the semichord is taken as unity.

The transformation $x = \cos\theta$, $\xi = \cos\tau$ reduces Eq. (48) to the following form, where g is considered a point function:

$$4k(\theta) = 2g(\theta) + g(0) + \beta(\theta)\int_{0}^{\pi} \frac{d\tau\, g'(\tau)}{\cos\tau - \cos\theta} + \int_{0}^{\pi} d\tau\, g'(\tau)H(\theta, \tau) \tag{49}$$

where

$$H(\theta, \beta, \tau) = \left[\sqrt{(\cos\tau - \cos\theta)^2 + \beta^2(\theta)} - \beta(\theta)\right]/(\cos\tau - \cos\theta) \tag{50}$$

A series expansion of $g(\theta)$ which satisfies the Kutta-Joukowsky condition and vanishes at the leading edge is given below, where, by definition, $A_{N-1} = A_N = 0$.

$$g(\theta) = (\pi - \theta)(A_0 + A_1) + \sum_{r=1}^{N-1} (A_{r-1} - A_{r+1})(\sin r\theta / r) \tag{51}$$

Upon substituting the expansion (51) for $g(\theta)$ in Eq. (49), the resulting equation may be reduced to the form

$$(4/\pi)k(\theta) = [F_1(\theta) - F_0(\theta)]A_0 + \sum_{r=1}^{N-2} [F_{r+1}(\theta) - F_{r-1}(\theta)]A_r \tag{52}$$

where the functions $F_r(\theta)$ are defined as follows:

$$\left.\begin{aligned} F_0(\theta) &= +(2\theta/\pi) + H_0(\theta, \beta) - 3 \\ F_r(\theta) &= \frac{2 \sin r\theta}{\pi r} + \frac{\beta(\theta) \sin r\theta}{\sin \theta} + H_r(\theta, \beta) \quad r = 1, 2, \ldots \end{aligned}\right\} \tag{53}$$

$$H_r(\theta, \beta) = \frac{1}{\pi} \int_0^\pi d\tau \cos r\tau H(\theta, \beta, \tau) \tag{54}$$

With the notation $k_n = k(n\pi/N)$ and $F_{r,n} = F_r(n\pi/N)$, the following set of simultaneous equations is obtained from Eq. (52) by collocation:

$$(4/\pi)k_n = (F_{1n} - F_{0n})A_0 + \sum_{r=1}^{N-2} (F_{r+1,n} - F_{r-1,n})A_r, \quad n = 1, 2, \ldots, N-1 \tag{55}$$

For the wing alone case, $k = (\pi/2)\beta^2 w$. Upon substituting this result in Eq. (55) with w equal to $1/(2b^2)$ where b is the semispan, there result the equations

$$(F_{1n} - F_{0n})A_0 + \sum_{r=1}^{N-2} (F_{r+1,n} - F_{r-1,n})A_r = (\beta_n/b)^2, \quad n = 1, 2, \ldots, N-1 \tag{56}$$

If the A_n satisfy the Eqs. (56), the lift curve slope C_{L_α} is given by the expression

$$C_{L_\alpha} = 2\pi \text{A.R.}(A_0 + A_1) \tag{57}$$

and the center of pressure is located aft of the leading edge a fraction dC_M/dC_L of the root chord, where

$$dC_M/dC_L = (1/2) - (1/4)[(A_0 - A_2)/(A_0 + A_1)] \tag{58}$$

The parametric lift per unit chord dg/dx is given by the formula

$$dg/dx = A_0 \tan(\theta/2) + 2 \sum_{r=1}^{N-2} A_r \sin r\theta \tag{59}$$

where the angle of attack w is taken as $1/(2b^2)$.

Numerical evaluation of the parameters $H_{rn}(\beta_n)$ accounts for a large portion of the total time required to obtain a solution of Eqs. (56). The H_{rn} are seen to be the coefficients of the Fourier series development of $H(\theta, \beta, \tau)$ in terms of the variable τ. As shown in reference 9, the trapezoid rule is the preferred procedure for numerical integration under these circumstances or

$$H_{rn}(\beta_n) = \frac{1}{\pi} \int_0^\pi d\tau \cos r\tau H(\theta_n, \beta_n, \tau) = \frac{1}{M}\left[\frac{H(\theta_n, \beta_n, 0) + (-)^r H(\theta_n, \beta_n, \pi)}{2} + \sum_{m=1}^{M-1} \left(\cos \frac{mr\pi}{M}\right) H\left(\theta_n, \beta_n, \frac{m\pi}{M}\right)\right] \tag{60}$$

The $H_{rn}(\beta)$ may be computed as functions of β and plotted. The results may then be used in all further calculations.

(XI) Numerical Results

Calculations were performed using three points for rectangular- and delta-wing plan forms. The parameters $H_{rn}(\beta)$ were computed and are plotted as functions of β in Fig. 1. The slope of the lift curve, center of pressure, damping in roll, and representative chordwise lift distributions are plotted and compared with test

data and with other theories where applicable. In applying these results to the curves of lift and moment versus angle of attack, the theory of reference 13 is used.

It will be noted that the chordwise lift distribution for low aspect ratio rectangular wings is negative over a portion of the chord, indicating that the three-point collocation procedure is not satisfactory. The results shown in Fig. 4, obtained from a five-point calculation, differ somewhat from the results from the three-point collocation procedure.

References

[1] Reissner, Eric, *On the General Theory of Thin Airfoils for Nonuniform Motion*, N.A.C.A. T.N. No. 946, August, 1944.

[2] Jones, R. T., *Properties of Low-Aspect-Ratio Pointed Wings at Speeds Below and Above the Speed of Sound*, N.A.C.A. Report No. 835, 1946.

[3] Weissinger, J., *The Lift Distribution of Swept-Back Wings*, N.A.C.A. T.M. No. 1120, March, 1947.

[4] Munk, Max M., *General Theory of Thin Wing Sections*, N.A.C.A. Report No. 142, 1922.

[5] Lomax, Harvard, and Heaslet, Max, *Linearized Lifting-Surface Theory for Swept-Back Wings with Slender Planforms*, N.A.C.A. T.N. No. 1992, December, 1949.

[6] Spreiter, John R., *Aerodynamic Properties of Slender Wing-Body Combinations at Subsonic, Transonic, and Supersonic Speeds*, N.A.C.A. T.N. No. 1662, 1948.

[7] Prandtl, L., *Tragflügeltheorie. I. Mitteilung, Nachrichten der K. Gesselschaft der Wissenschaften zu Göttingen*, Math.-Phys. Klasse, pp. 451–477, 1918.

[8] Reissner, Eric, *Note on the Theory of Lifting Surfaces*, Proceedings of the National Academy of Sciences, Vol. 35, No. 4, pp. 208–215, April, 1949.

[9] Milne, William Edmund, *Numerical Calculus*, p. 302; Princeton University Press, 1949.

[10] Bollay, W., *A Nonlinear Wing Theory and Its Application to Rectangular Wings of Small Aspect Ratio*, Jb. d. Luftf.-Forschg., P.I. 139, 1939.

[11] Weinig, F., *Lift and Drag of Wings with Small Span*, N.A.C.A. T.M. No. 1151, 1947.

[12] Allen, H. Julian, *Pressure Distribution and Some Effects of Viscosity on Slender-Inclined Bodies of Revolution*, N.A.C.A. T.N. No. 2044, March, 1950.

[13] Flax, A. H., and Lawrence, H. R., *The Aerodynamics of Low-Aspect-Ratio Wings and Wing-Body Combinations*, to be presented at the Third International Joint Conference of the R.Ae.S.-I.A.S., Brighton, England, September 3–14, 1951.

[14] Tosti, L. P., *Low Speed Static Stability and Damping-in-Roll Characteristics of Some Swept and Unswept Low-Aspect-Ratio Wings*, N.A.C.A. T.N. No. 1468, October, 1947.

[15] *Wind-Tunnel Tests on Cornell Aeronautical Laboratory Static Stability Missile Models*, GALCIT Report 539, May, 1949.

[16] Ribner, H. S., *The Stability Derivatives of Low-Aspect-Ratio Triangular Wings at Subsonic and Supersonic Speed*, N.A.C.A. T.N. No. 1423, September, 1947.

Notice to Contributors

Manuscripts submitted for publication *must* be double- or triple-spaced originals. There should be wide margins on both sides of the sheets and triple spacing around formulas to allow for the marking of directions for the printer.

Original drawings (jet black India ink on white paper or tracing cloth) should accompany the manuscript. *(Blueprints are not acceptable.)* Photographs *must* be on glossy white paper. The smallest lettering on 8- by 10-in. figures should be no less than 1/4 in. high.

Only the simplest formulas should be typewritten; all others should be carefully written in pen and ink. The difference between capital and lower-case letters and Greek symbols should be clearly distinguished.

See Inside Back Cover of this issue for further details.

Readers' Forum

BRIEF REPORTS of investigations in the aeronautical sciences and discussions of papers published in the JOURNAL are presented in this special department. Publication will be completed approximately 8 to 10 weeks after receipt of the material. The Editorial Committee does not hold itself responsible for the opinions expressed by the correspondents. Contributions should not exceed 800 words in length.

Effects of Density Fluctuations on the Turbulent Skin Friction of an Insulated Flat Plate at High Supersonic Speeds

T. Y. Li and H. T. Nagamatsu
California Institute of Technology
June 20, 1951

FOR A FULLY DEVELOPED turbulent flow problem, it is important to estimate the Reynolds stresses due to the eddying motions of the fluid masses. In the compressible flow regime, these Reynolds stresses consist of three major parts—viz., (1) that due to velocity fluctuations, (2) that due to density fluctuations, and (3) that due to pressure fluctuations. (The effects of the fluctuations in the viscosity coefficient are considered to be unimportant.) The apparent stresses due to pressure fluctuations are usually neglected in a theory of thin turbulent boundary layer. In several recent papers,[1-4] the turbulent friction on an insulated flat plate at a supersonic speed has been computed without giving an adequate estimate of the apparent shear due to density fluctuations. Attempts have been made in the present research to derive a turbulent skin-friction formula that provides a reasonable estimate of the effects of density fluctuations at high supersonic speeds.

Extending von Kármán's similarity considerations and Prandtl's mixing length concepts to the compressible flow regime, we are able to derive the following fundamental differential equation representing the turbulent friction on a flat plate:

$$\tau_w = \left(\rho \frac{d\bar{u}}{dy} + \alpha\bar{u}\frac{d\rho}{dy}\right) k^2 y^2 \frac{d\bar{u}}{dy} \tag{1}$$

In the derivation of Eq. (1), we have assumed that the flat plate is lying parallel to the main stream. $\bar{u}$ and $\bar{\rho}$ designate the mean velocity and the mean density of the flow within the turbulent boundary layer; they are essentially functions of y, which is the distance in the direction perpendicular to the flat plate. τ_w is the shear stress at the surface of the flat plate. k is the incompressible mixing length constant. α is a proportionality constant that is defined as the compressibility mixing length constant. The term containing α represents the contribution from density fluctuations.

Crocco[5] has shown that the differential equations for compressible flow, including viscosity and heat conductivity, have a particular integral of the following form:

$$(u^2/2) + C_P T = \text{constant} \tag{2}$$

provided that no heat is added from external sources and that the Prandtl Number is unity. We shall assume that Eq. (2) holds for the mean flow in the turbulent boundary layer on an insulated flat plate. We can then integrate Eq. (1). The result of such integration is substituted into the momentum integral relation.

$$\tau_w = \frac{\partial}{\partial x}\int_0^\delta \bar{\rho}\bar{u}\,(u_1 - \bar{u})\,dy \tag{3}$$

where the x-direction is parallel to the surface of the flat plate, δ represents the total thickness of the boundary layer, and the subscript 1 designates the conditions pertaining to the main free stream. Thus, we obtain a new formula for the turbulent friction of an insulated flat plate as follows:

$$\frac{F(\Lambda)}{[(\gamma-1)M_1^2/2]^{1/2}}\left(\frac{2}{C_{F_1}}\right)^{1/2} = \frac{1}{k}\left\{\ln C_{F_1}R_1 - \omega\ln\left(1 + \frac{\gamma-1}{2}M_1^2\right) + \frac{1}{2}\ln\left[1 + \frac{(2\alpha-1)(\gamma-1)M_1^2}{2[1+(\gamma-1)M_1^2/2]}\right]\right\} \tag{4}$$

where

$$\left.\begin{aligned} F(\Lambda) &= \int_0^\Lambda \frac{[1 + (2\alpha-1)Z^2]^{1/2}}{1 - Z^2}\,dZ \\ \Lambda &= \left\{\frac{[(\gamma-1)/2]M_1^2}{1 + [(\gamma-1)/2]M_1^2}\right\}^{1/2} \end{aligned}\right\} \tag{5}$$

$$C_{F_1} = \int_0^x \tau_w\,dx \Big/ \frac{1}{2}\rho_1 u_1^2\, x = \text{mean skin-friction coefficient}$$

$$R_1 = \rho_1 u_1 x/\mu_1$$

$$\omega = \log(\mu_w/\mu_1)/\log(T_w/T_1)$$

and μ, γ, and T represent the coefficient of viscosity, the ratio of specific heats, and the absolute temperature, respectively, while R_1 and M_1 denote the free-stream Reynolds Number and Mach Number, respectively. The function $F(\Lambda)$ in Eq. (5) has been analytically evaluated for fixed α.[6]

It is clear that the value of α gives a measure of the relative importance of the apparent shear stress due to density and velocity fluctuations. When the density variation across the boundary layer is slight—for instance, in the lower supersonic range,

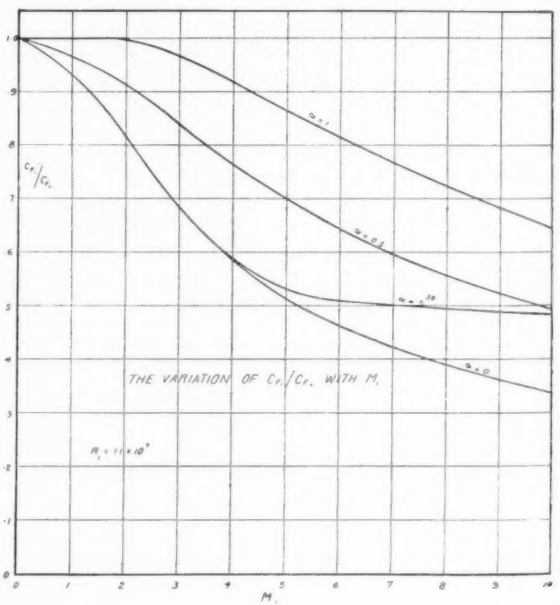

FIG. 1.

$M_1 \leq 2.5$—we may take $\alpha = 0$. On the other hand, when the density variation is pronounced—for instance, in the higher supersonic range—we have to use some other values of α. Thus, α has to be regarded as a function of the free-stream Mach Number, M_1. We shall assume

$$\alpha = \Lambda^n \tag{6}$$

Eq. (6) states that as $M_1 \to 0$, $\alpha \to 0$, and as $M_1 \to \infty$, $\alpha \to 1$; the latter statement appears reasonable, because it is plausible that, as $M_1 \to \infty$, the effects of density and velocity fluctuations are equally important.

In Fig. 1, several curves representing the variation in C_{F_1}/C_{F_i}* with M_1 at $R_l = 1.1 \times 10^7$, computed on the basis of Eq. (4) with various values of α, are presented. It is noted that $\alpha = 0$ corresponds to Van Driest's (and Wilson's) curve, $\alpha = 0.5$ corresponds to Ferrari's analysis, while $\alpha = 1$ gives Clemmow's† results. We think that the effects of density fluctuations are varying with the free-stream Mach Number; thus, a theory on the basis of a fixed value of α perhaps may not be adequate for the entire speed range that we are interested in ($0 \leq M_1 \leq 10$, say). A simple variation of α with M_1, as proposed in Eq. (6), is therefore likely to be more useful. Some intensive experimental program will be conducted in the higher supersonic range by utilizing the Army Ordnance-GALCIT Hypersonic Wind Tunnel to verify and improve the present theory.

REFERENCES

[1] Wilson, R. E., *Turbulent Boundary-Layer Characteristics at Supersonic Speeds—Theory and Experiment*, Journal of the Aeronautical Sciences, Vol. 17, No. 9, p. 585, September, 1950.

[2] Van Driest, E. R., *Turbulent Boundary Layer in Compressible Fluids*, Journal of the Aeronautical Sciences, Vol. 18, No. 3, p. 145, March, 1951.

[3] Ferrari, C., *Study of the Boundary Layer at Supersonic Speeds in Turbulent Flow: Case of Flow Along a Flat Plate*, Quarterly of Applied Mathematics, Vol. 18, No. 1, p. 33, April, 1950.

[4] Clemmow, D. M., *The Turbulent Boundary Layer Flow of a Compressible Fluid Along a Flat Plate*, D.G.W.R.D. Report 50/6, August, 1950.

[5] Crocco, L., *Su di un valore massino del coefficiente di trausmissione del calose da una limina piana a un fluido seconente*, Rendiconti R. Accademia dei Lincei, Vol. 14, p. 490, December, 1931, see also L'Aerotechnica, Vol. 12, No. 2, 1932.

[6] Li, T. Y., and Nagamatsu, H. T., *Effects of Density Fluctuations on the Turbulent Skin Friction of an Insulated Flat Plate at High Supersonic Speeds*, GALCIT Hypersonic Wind Tunnel Memorandum No. 5, May, 1951.

On Subsonic Conical Methods

Seymour Lampert
Ames Aeronautical Laboratory, N.A.C.A., Moffett Field, Calif.
June 18, 1951

IN THE COMMENTS[1] by Theodore R. Goodman which appeared in the Readers' Forum of the June, 1951, issue of the JOURNAL on the paper[2] by the author, it was pointed out that, in general, the conical solutions to Laplace's equation do not in themselves represent physically possible subsonic flow fields since the boundary condition of zero disturbance at infinity will not be fulfilled.

In reference 2, the example of the uniformly loaded semi-infinite sector was inserted to illustrate this point, which, however, may not have been sufficient clarification. It is clear, however, that by the proper superposition of these conical solutions, as was done in reference 2, the boundary conditions at the wing and infinity can be satisfied so that a physically possible subsonic flow may be represented.

REFERENCES

[1] Goodman, Theodore R., *On the Nonexistence of Subsonic Conical Flows*, Journal of the Aeronautical Sciences, Vol. 18, No. 6, p. 427, June, 1951.

[2] Lampert, Seymour, *Conical Flow Methods Applied to Uniformly Loaded Wings in Subsonic Flow*, Journal of the Aeronautical Sciences, Vol. 18, No. 2, p. 107, February, 1951.

Small Pitot Tubes with Fast Pressure Response Time*

W. S. Bradfield and G. E. Yale
University of Minnesota, Rosemount Research Center, Rosemount, Minn.
June 25, 1951

THE NEED FOR A SMALL PITOT TUBE appears fairly often in aerodynamic investigation—for example, exploration of thin boundary layers is one common application. The production of small probes suited to this application has been well understood for some years. The experiment of Stanton and Marshall[1] involved one of the first attempts at this technique. However, the Stanton tube, while small, was unlike the small probes that are in use today. It differed principally in that it utilized as its lower surface the actual surface of the plate. The distance of the "tube opening" from the surface of the plate was obtained by raising or lowering the top surface of the tube from within the plate. Examples of the recent application of small pitot tubes of conventional types are found in references 2 and 3.

Particularly in an intermittent flow wind tunnel, emphasis must be placed on fast response as well as on small size. In connection with an experiment[4] relating to the determination of velocity profiles within the boundary layer at high speed, the authors succeeded in developing a technique for producing a pitot tube with an opening 1 mil high which will come to equilibrium in a period of time between 5 and 20 sec.

Analysis of the optimum configuration of a pressure-sensing instrument involving a pressure orifice, tubing, and an end organ

* This work was done as a portion of research sponsored by the Office of Air Research, Air Materiel Command.

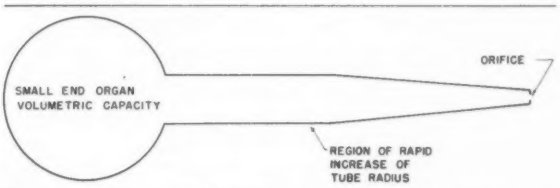

FIG. 1. Optimum configuration for a fast response pressure-sensing system.

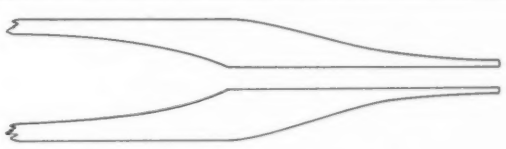

FIG. 2. Poor total pressure probe entry.

* $C_{Fi} = (C_{F_1})_{M_1=0}$.

† There is apparently a misprint in Clemmow's formula for $F(\Lambda)$.

FIG. 3. Photomicrograph of typical total pressure probe.

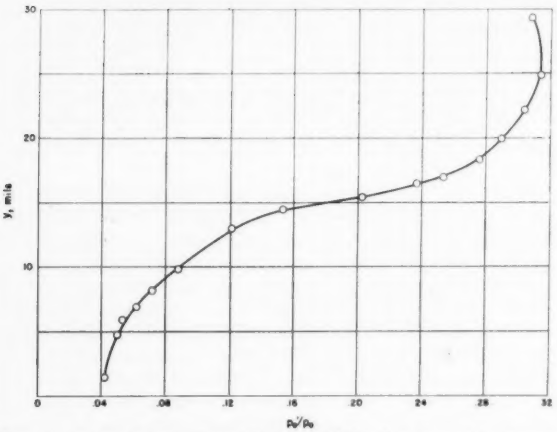

FIG. 4. A total pressure profile through laminar boundary layer at Mach Number 3.

(such as a manometer or capsule type electrical pickup) has resulted in a clear specification of conditions to be met.[5,6] Fig. 1 shows schematically the optimum configuration of a fast response pressure-sensing system. The salient point is that the opening into the pressure measuring system—that is, the pressure orifice itself—must be an orifice; it must not be a passageway. It is clear that, if it is a passageway, the Reynolds Number will be small because of its small height. The friction coefficient, then, will be correspondingly high. In general, the other features of the design are simply structural and aerodynamic considerations that make certain that the tube between the orifice and the manometer diverges in such a manner that extremely high friction coefficients are avoided. The length of connecting tube is minimized in order that the volumetric capacity of the system shall be as small as possible. However, the most important single feature is the production of an orifice at the probe opening. Attention to this particular detail made a difference in response time of a factor of six to ten in the present investigation.

The most satisfactory method of construction was found to be the following. Heat gently a piece of $^1/_{32}$-in. brass tubing approximately 3 in. long by passing a gas torch flame back and forth across the tube while the tube is placed under tension. The tube will elongate a certain amount and become smaller in diameter, finally breaking and yielding a tube of considerably less diameter. The wall of the tube is still thicker than necessary, and the thickness is reduced to approximately 0.002 or 0.003 in. by etching with a solution of 1 part copper sulphate and 2 parts water (distilled).

Obtain a piece of sheet steel 0.001 in. thick by 0.010 in. wide, if necessary, by etching a thicker piece with the following solution: 34 parts sulphuric acid (concentrated), 42 parts ortho-phosphoric acid, and 24 parts water (distilled). Slightly flatten probe and insert steel approximately $^1/_4$ in. and flatten probe with hammer for about $^1/_{10}$ in. from end. Polish surface of probe with a fine wet stone and withdraw steel insert. View probe under a suitable microscope to verify probe dimensions and smoothness of surfaces. When the size and smoothness of the tip are satisfactory, the response time should be checked. This can be done easily on the bench using a U-tube with the probe connected in series with one leg and a pressure (or vacuum) source with the other leg. If the response time is unreasonable, it is most probably a result of too much tip flattening. In this case the passageway will appear as in Fig. 2. The error may be corrected by clipping about $^1/_{61}$ in. off the end of the tube and reopening the tube by filling or stoning. The clipping procedure should be repeated until the response time is satisfactory.

A photomicrograph of a typical total head probe produced by the foregoing technique is shown as Fig. 3. The dimensions of this probe were checked by the use of a 100-power microscope. The response time was found to be from 5 to 7 sec. for 21 in. of mercury.

Tubes produced in accordance with the technique outlined in the foregoing paragraphs were used to obtain velocity profiles in a laminar boundary layer on a cone at Mach Number 3. The boundary-layer thickness was as small as 16 mils (0.4 mm.). The tunnel was an intermittent tunnel having a running time at this Mach Number of approximately 50 sec. After bench testing of the probes used to determine their response time, they were applied to the actual determination of the total pressure in the boundary layer of the model. By careful and repeated observation of the manometer during the run, it was established that a definite point of equilibrium was reached during each run and that the time required to reach equilibrium was not noticeably different from that required on the bench. The total pressure being run varied from approximately 0.7 to 50 in. of mercury. A typical total pressure profile at a relatively low Reynolds Number is shown in Fig. 4.

It should be easily possible to make probes of even smaller physical dimensions having almost equally good response. The metal deposition technique has been suggested as a possibility in this regard. For example, the deposition of metal on nylon fibers has been developed to the point where tubes having inside diameters as small as 2 mils have been made.[7]

REFERENCES

[1] Stanton and Marshall, Roy. Soc. Proc., Series A, Vol. 97, p. 413, 1920.

[2] Blue, R. E., *Interferometer Corrections and Measurements of Laminar Boundary Layers in Supersonic Stream*, N.A.C.A. T.N. No. 2110.

[3] Liepmann, H. W., Roshko, A., and Dhawan, S., *On Reflection of Shock Waves from Boundary Layers*, N.A.C.A. T.N. No. 2334.

[4] Bradfield, W. S., *Measurement of Shearing Stress on a Body of Revolution*, Report of Progress 1 October to 31 December 1950, Air Materiel Command Contract AF 33(038) 12918.

[5] Kendall, J. M., *Time Lags Due to Compressible Poisville Flow Resistance in Pressure Measuring Systems*, N.O.L.M. 10677.

[6] Schaaf, S. A., *Theory of Minimum Response Time for Vacuum Gages*, University of California, Rep. No. HE-150-21.

[7] Gezelius, R. J. E., *Making Small Metal Tubes by Electrodeposition on Nylon Fibers*, Review of Scientific Instruments, Vol. 21, No. 10, October, 1950.

Cooling Required To Stabilize the Laminar Boundary Layer on a Flat Plate

E. R. Van Driest

Aerophysics Laboratory, North American Aviation, Inc., Downey, Calif.

July 6, 1951

IN HIS REMARKABLE PAPER,[1] Lees predicted that it would be possible, by cooling, to completely stabilize the laminar

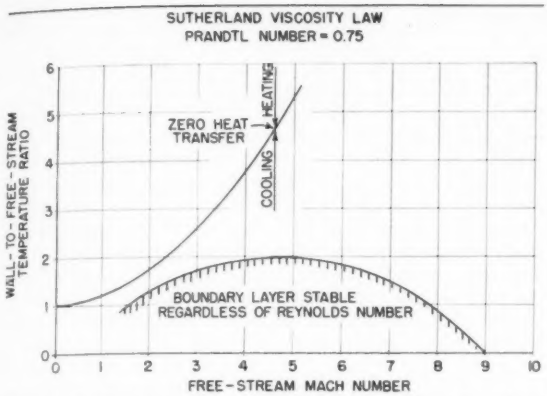

FIG. 1. Cooling required to stabilize the laminar boundary layer on a flat plate regardless of Reynolds Number.

boundary layer on a flat plate at all Reynolds Numbers in supersonic flow. In fact, his calculations showed that radiation alone would be sufficient to maintain complete stability of the boundary layer on a plate moving at Mach Number 3 at altitude 50,000 ft. This was, of course, comforting to engineers engaged in high-speed aerodynamics. The assumptions made by Lees were that the Prandtl Number was unity and that the viscosity was directly proportional to the temperature.

Because of the significance of Lees' conclusion to high-speed aerodynamics, the writer has recalculated the amount of cooling required to completely stabilize the boundary layer, using the more realistic Prandtl Number of 0.75 and Sutherland viscosity-temperature law. The Crocco method was used to obtain the properties of the boundary layer. Fig. 1 shows the results of the calculations. It seems that considerably more cooling is required than predicted by Lees and that, above about Mach Number 9, it is impossible to stabilize the boundary layer by any amount of cooling. Furthermore, it appears that when the layer can be stabilized by cooling, even full radiation (emissivity unity) is not sufficient.

The question arises as to the reason for the radical difference between the results of Lees and those of the writer. In the first place, the writer's lower Prandtl Number would require more cooling than predicted by Lees, but the writer does not expect this to be the major cause of the discrepancy. In the second place, it seems that Lees' assumption of viscosity-temperature proportionality should show an even greater effect than obtained by the writer because of the greater thickness of the layer compared to that resulting from viscosities given by the Sutherland law. Therefore, it seems that Lees' original calculations should have shown a much greater cooling required to completely stabilize the laminar boundary layer regardless of Reynolds Number than was indicated in reference 1.

REFERENCE

[1] Lees, Lester, *The Stability of the Laminar Boundary Layer in a Compressible Fluid*, N.A.C.A. T.N. No. 1360, July, 1947.

Secondary Flow in Cascades

J. M. Stephenson
Farnborough, England
July 13, 1951

THE RECENT PAPER by Squire and Winter[1] is the first to describe the gyroscope effect that occurs when the flow into a bend contains vorticity. However, the effect can be derived simply from the principle of conservation of circulation (or of angular momentum in the case of a gas).

Consider the cascade of Fig. 1, deflecting a stream of incompressible inviscid fluid. The inlet velocity v_1 has a profile of arbitrary shape. With the usual assumption that the number of blades is infinite, the velocity diagram is as drawn in Fig. 2. At every point upstream, there exists a vorticity vector at right angles to the stream direction of magnitude $\xi = -\partial v_1/\partial x$; similarly, downstream is a vector $\eta = -\partial v_2/\partial x$. If we assume that the spanwise perturbations are small, the profile of the axial (z-wise) velocity component v_a is unchanged through the cascade.* Therefore, if α_2 is independent of the velocity (a common assumption), we have

$$\xi = -\sec \alpha_1 \cdot \partial v_a/\partial x$$
$$\eta = -\sec \alpha_2 \cdot \partial v_a/\partial x$$

To conserve the circulation in the system, an axial vorticity vector appears downstream of magnitude

$$\xi \sin \alpha_1 - \eta \sin \alpha_2 = -(\tan \alpha_1 - \tan \alpha_2)\cdot \partial v_a/\partial x$$

which has a component ζ in the direction of α_2, such that

$$\zeta = -(\tan \alpha_1 - \tan \alpha_2)\cdot \cos \alpha_2 \cdot \partial v_a/\partial x$$
$$= (\tan \alpha_1 - \tan \alpha_2)\cdot \cos \alpha_1 \cdot \cos \alpha_2 \cdot \xi \qquad (1)$$

This vorticity implies a secondary rotation of the fluid as in Fig. 3.

Both the theory and the measurements of reference 1 only apply to a single passage in a cascade. But there is also present in the downstream flow the circulation shed from the trailing edges of each airfoil. This phenomenon is well known; the resulting vorticity is

$$\Omega = -(1/s)\cdot(\partial K/\partial x)$$

where K is the circulation on each airfoil and s is the airfoil spacing.

But

$$K = s v_a (\tan \alpha_1 - \tan \alpha_2)$$

Hence,

$$\Omega = -(\tan \alpha_1 - \tan \alpha_2)\cdot \partial v_a/\partial x$$

* If this assumption is not made, it can be shown that the subsequent analysis is unaltered, except that in Eqs. (1) and (2) $\tan \alpha_2$ must be replaced by $C \tan \alpha_2$, where

$$C = \frac{2 + (\tan^2\alpha_1 - \tan^2\alpha_2)}{2 - (\tan^2\alpha_1 - \tan^2\alpha_2)}$$

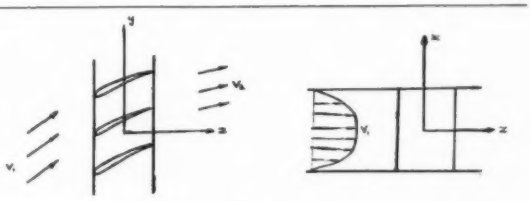

FIG. 1.

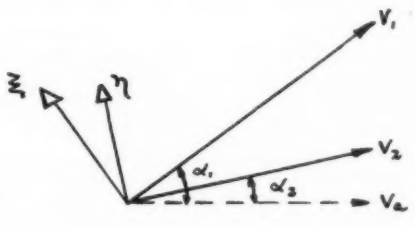

FIG. 2.

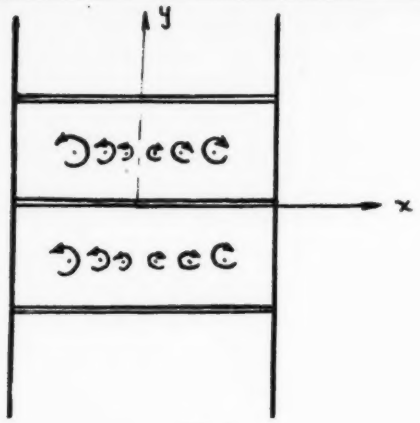

FIG. 3.

and

$$\Omega = -(\tan \alpha_1 - \tan \alpha_2) \cdot \cos \alpha_1 \cdot \xi \qquad (2)$$

The resultant vorticity in the direction of α_2 is thus, from Eqs. (1) and (2),

$$\Omega + \zeta = (1 - \cos \alpha_2) \cos \alpha_1 (\tan \alpha_1 - \tan \alpha_2) \cdot \xi$$

which has always the same sign as ξ but is zero when $\alpha_2 = 0$. Therefore, there is a minimum induced velocity field and secondary flow downstream of the cascade if the gas flow at outlet is in the axial direction.

It is perhaps worth mentioning that in the most important application of cascade theory—namely, to the design of axial-flow compressors and turbines—the gyroscope effect plays no part. For, when annular cascades are closely spaced, only the axial velocity component at any point has a peaked profile. Therefore, the vorticity vector ξ is not rotated on passing through a row, and the only extra component to appear is that shed from the blades. It is still true, however, that this component is a minimum when the outlet velocity is in the axial direction, but for a different reason.

A small correction is necessary in Fig. 4 of reference 1, where the ordinate scale should be multiplied by 0.9.

REFERENCE

[1] Squire, H. B., and Winter, K. G., *The Secondary Flow in a Cascade of Airfoils in a Nonuniform Stream*, Journal of the Aeronautical Sciences, Vol. 18, No. 4, p. 271, April, 1951.

Note on the Hypersonic Similarity Law for an Unyawed Cone*

Lester Lees
Department of Aeronautical Engineering, Princeton University
June 4, 1951

ACCORDING TO THE HYPERSONIC SIMILARITY LAW,[1, 2] at very high Mach Numbers the pressure coefficient on the surface of a series of unyawed slender bodies of revolution with the same thickness distribution along their axes can be written in the form

$$C_p = \frac{p - p_1}{(1/2)\rho_1 U_1^2} = \frac{G(K_1, \xi)}{M_1^2}$$

Here, $K_1 = M_1/(l/d)$ is the similarity parameter, l is body length, d is maximum body diameter, M_1 is free-stream Mach Number, and $\xi = x/l$, where x is axial distance measured from the nose. Also, the drag coefficient based on maximum frontal area takes the form $C_D = F(K)/M_1^2$. Recently, it has been found that the hypersonic similarity law for slender cones and ogival bodies applies not only for $M \gg 1$, as postulated in the original derivations, but extends also to moderate supersonic speeds ($M \approx 3$).[3] The purpose of this brief note is to show that, at least in the case of the unyawed cone, the extensive range of applicability of hypersonic similarity is foreshadowed by the analytical expressions for the velocity components of the conical flow behind the shock and by the boundary condition at the shock surface. In the course of the discussion, a relatively simple algebraic expression is derived for the drag function $F(K)$ which is applicable when the shock is not too far from the cone surface.

Taylor and Maccoll[4] showed that the continuity and momentum equations, plus the irrotationality condition, for the flow over an unyawed cone lead to the following differential equation for the velocity component, u, along a ray from the cone vertex

$$\left[\frac{\gamma + 1}{2} U'^2 - \frac{\gamma - 1}{2}(1 - U^2)\right] U'' - (\gamma - 1) U(1 - U^2) - \frac{\gamma - 1}{2}(1 - U^2)U' \cot \omega + \gamma U U'^2 + \frac{\gamma - 1}{2} U'^3 \cot \omega = 0 \quad (1)$$

Here, $U = u/w_{max.}$, $w_{max.}$ is the limiting adiabatic velocity, ω is the conical ray angle, and the primes denote differentiation with respect to ω. Also, $V = U'$, where V is the velocity component normal to a ray, taken positive in the direction of ω increasing. At the cone surface, $U = U_c$, $U' = 0$ and, from Eq. (1), $U'' = -2U_c$, $U''' = 2U_c \cot \theta_c$, where θ_c is the cone half-angle, and $U^{iv} = -24a_4$, where

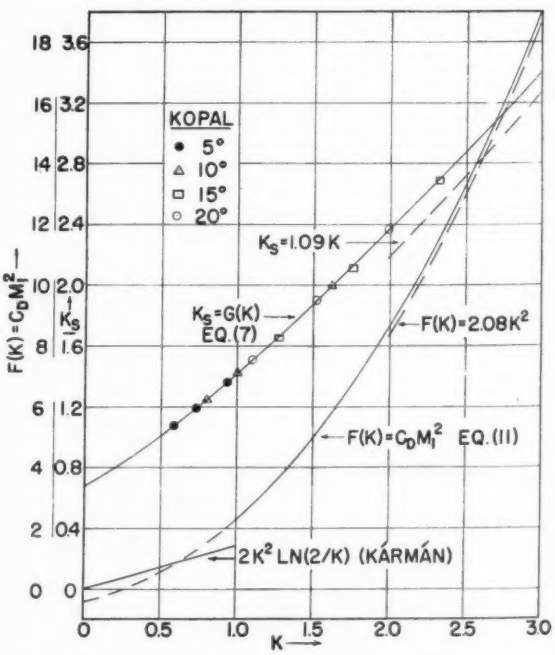

FIG. 1. Conical shock angle parameter $K_s = M_1\omega_s$ and drag function $F(K) = C_D M_1^2$ as functions of similarity parameter $K = M_1\theta_c$.

* After this note had been prepared, it was brought to my attention by S. I. Cheng that this problem had been treated previously by Shen,[5] who utilized Hayes' suggestion[2] of considering the flow in a transonic plane as that generated by a radially expanding cylinder. However, simple algebraic expressions were not obtained, and the numerical solutions appear to differ somewhat from the present results, except in the limiting case $K \to \infty$.

$$a_4 = \frac{1}{4}\cot^2\theta_c + \frac{2}{3(\gamma-1)}\frac{U_c^2}{1-U_c^2}$$

etc. Therefore the Taylor series expansions for the velocity components from the cone surface outward are as follows:

$$\left.\begin{aligned}\frac{U}{U_s} &= 1-(\omega-\theta_c)^2+\frac{1}{3}\cot\theta_c(\omega-\theta_c)^3-a_4(\omega-\theta_c)^4+\dots\\ \frac{V}{U_c} &= -2(\omega-\theta_c)+\cot\theta_c(\omega-\theta_c)^2-4a_4(\omega-\theta_c)^3+\dots\end{aligned}\right\} \quad (2)$$

By substituting the Eqs. (2) in Eq. (3), one obtains

$$M_1(\omega_s-\theta_c) = \frac{\gamma-1}{\gamma+1}\left[\frac{M_1\sin^2\omega_s+\frac{2}{\gamma-1}\frac{1}{M_1}}{\sin 2\omega_s}\right]\left[\frac{1-(\omega_s-\theta_c)^2+\frac{1}{3}\cot\theta_c(\omega_s-\theta_c)^3-a_4(\omega_s-\theta_c)^4+\dots}{1-\frac{1}{2}\cot\theta_c(\omega_s-\theta_c)+2a_4(\omega_s-\theta_c)^2+\dots}\right] \quad (4)$$

But

$$\left.\begin{aligned}2a_4(\omega-\theta_c)^2 &= \frac{1}{2}\left(\frac{K_s-K}{K}\right)^2+\frac{1}{\gamma-1}\frac{4}{3}\frac{(K_s-K)^2\left[1-\frac{K_s^2}{M_1^2}+\dots\right]}{K_s^2-(K_s-K)^2+\frac{2}{\gamma-1}\left[1-\frac{(K_s-K)^2}{M_1^2}+\dots\right]+\dots}\\ \sin^2\omega &= \omega^2\left(1-\frac{1}{3}\frac{K_s^2}{M_1^2}+\dots\right),\ \text{etc., where } K_s = M_1\omega_s\end{aligned}\right\} \quad (5)$$

Therefore, the relation (4) becomes

$$K_s-K \approx \frac{1}{2}\frac{\gamma-1}{\gamma+1}\frac{\left[K_s\left(1+\frac{1}{3}\frac{K_s^2}{M_1^2}+\dots\right)+\frac{2}{\gamma-1}\left(1+\frac{2}{3}\frac{K_s^2}{M_1^2}+\dots\right)\frac{1}{K_s}\right]\left[1-\frac{(K_s-K)^2}{M_1^2}+\dots\right]}{\left[1-\frac{1}{2}\frac{K_s-K}{K}+\frac{1}{2}\left(\frac{K_s-K}{K}\right)^2+\dots+O\left\{\frac{(K_s-K)^2}{K_s^2+\frac{2}{\gamma-1}}\right\}\right]} \quad (6)$$

Two important conclusions can be drawn from Eq. (6).

(1) The hypersonic similarity law should apply for the unyawed cone so long as ω_s is less than about 0.4 rad., or $\omega_s < 24°$ (approx.), because, when this condition is satisfied, ω_s and θ_c enter only as the parameters K_s and K and terms involving K_s^2/M^2 and $(K_s-K)^2/M_1^2$ make only small contributions to the final result. Thus, hypersonic similarity should begin to apply for the slenderest cones ($\theta_c \approx 0°$) at $M_1 \approx 2.5 \to 3$, and the range of applicability increases rapidly as M_1 increases, up to a value of θ_c of about 20° for air ($\gamma = 1.4$) when $M_1 \to \infty$ (see curve $\omega_s = 24.4°$, Fig. 2).

In Tsien's original derivation,[1] the square of the perturbation velocity in the flight direction must be small compared with the square of the velocity normal to the flight direction in order for hypersonic similarity to exist. From Eq. (2) and the shock relations, it can be seen that this condition is satisfied when ω^2 is sufficiently small—i.e., $\omega < 24°$ (approx.), and $2.5 \to 3.0 < M < \infty$. Also, under these conditions, the *local* sonic velocity is small compared with the local velocity parallel to the flight direction ($a^2/U^2 \sim \omega^2$), as required in Hayes' analysis.[2]

(2) When, *in addition*, $(K_s-K)/K$ is small compared with unity—i.e., when the conical shock is not too far from the cone surface—Eq. (6) is approximated as follows:

$$K_s-K \approx \frac{1}{2}\left(\frac{\gamma-1}{\gamma+1}\right)\left[K_s+\frac{2}{\gamma-1}\frac{1}{K_s}\right]$$

or

and the succeeding terms do not bring any new factors into this discussion.

Now the boundary condition at the conical shock can be put in the form (see, for example, Kopal[5])

$$-\frac{\gamma-1}{\gamma+1}\frac{1-U_s^2}{U_sV_s} = \tan\omega_s \quad (3)$$

$$K_s \approx \frac{\gamma+1}{\gamma+3}K+\sqrt{\left(\frac{\gamma+1}{\gamma+3}\right)^2K^2+\frac{2}{\gamma+3}} \quad (7)$$

This approximation, which amounts to utilizing only the first term in the expansions of Eq. (2), should be valid for $K \geq 1.0$ (approx.) within the range of values of M_1 and θ_c for which hypersonic similarity applies. In other words, this approximation is valid for $M_1 > 4$ and $1/M < \theta_c < \bar{\theta}$, where $\bar{\theta}$ corresponds to the upper limit of the "zone" of hypersonic similarity. In Fig. 1 the relation between conical shock angle and cone angle prescribed by Eq. (7) is compared with the actual values given by the Taylor-Maccoll theory as computed by Kopal.[5] For $K > 0.5$, the difference between exact values of conical shock angle and the prediction of Eq. (7) is negligible.

When the approximate relation given by Eq. (7) is valid, a correspondingly simple expression is obtained for the pressure coefficient on the surface of an unyawed cone. Now,

$$p_c/p_1 = (p_s/p_1)(p_c/p_s) \quad (8)$$

where

$$\frac{p_s}{p_1} = \frac{2\gamma}{\gamma+1}M_1^2\sin^2\omega-\frac{\gamma-1}{\gamma+1} \quad (8a)$$

and

$$p_c/p_s = (a_c^2/a_s^2)^{\gamma/(\gamma-1)} \quad (8b)$$

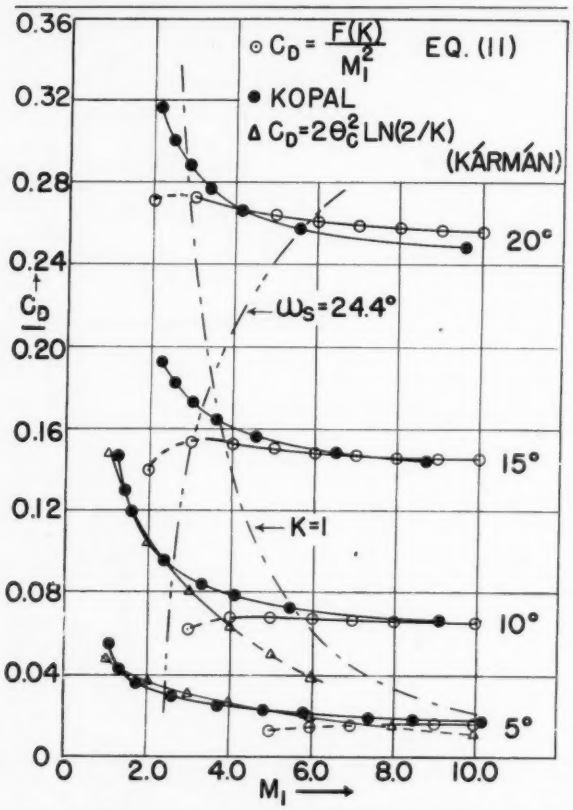

FIG. 2. Comparison between approximate drag formula for unyawed cone and exact values as computed by Kopal. The curve $\omega_s = 24.4°$ shows the approximate limits of applicability of the hypersonic similarity law.

Here, p_c and a_c are the static pressure and sonic velocity, respectively, on the cone surface, and p_s and a_s are the static pressure and sonic velocity just behind the conical shock. From the energy equations,

$$\frac{a_c^2}{a_s^2} = 1 + \frac{\gamma - 1}{2}\frac{u_s^2}{a_1^2}\frac{a_1^2}{a_s^2}\left[1 - \left(\frac{u_c}{u_s}\right)^2 + \left(\frac{v_s}{a_s}\right)^2\right] \qquad (9)$$

so that, with $v_s/u_c \approx -2(\omega_s - \theta_c)$ and $u_s/u_c \approx 1 - (\omega_s - \theta_c)^2$,

$$\left.\begin{aligned}\frac{a_c^2}{a_s^2} &\approx 1 + (\gamma - 1)\frac{a_1^2}{a_s^2}(K_s - K)^2 \\ \frac{p_c}{p_s} &\approx 1 + \gamma\frac{a_1^2}{a_s^2}(K_s - K)^2\end{aligned}\right\} \qquad (10)$$

From Eqs. (8a), (8b), and (10),

$$F(K) \equiv \frac{2}{\gamma}\left(\frac{p_c}{p_1} - 1\right) \equiv C_D M_1^2 = \frac{4}{\gamma + 1}(K_s^2 - 1) + 2(K_s - K)^2\left\{\frac{\gamma + 1}{\gamma - 1 + (2/K_s^2)}\right\} \qquad (11)$$

and K_s is related to K by Eq. (7). The drag function $F(K)$ is plotted in Fig. 1. Again, this approximate formula is expected to be valid for $K \geqq 1$, or for $M_1 > 4$ (approx.), and $1/M_1 < \theta_c < \hat{\theta}$. For comparison, the drag function $C_D M_1^2 = 2K^2 \ln(2/K)$ obtained from the "slender-body" approximation to the linearized supersonic theory[6] is also shown, for $K < 1$. In this approximation, the shock or Mach cone must be far from the body, while in the present approximation the shock cone is close to the body.

In Fig. 2, the drag coefficient for an unyawed cone given by Eq. (11) is compared with the "exact" values as computed by Kopal. The approximate limits of applicability of hypersonic similarity are indicated by the dashed curve labeled $\omega_s = 24.4°$. For $K > 1$, the present approximation gives values of C_D within 7 per cent of the exact values. An interesting result is that, for the cones of 5° and 10° half-angle, the von Kármán approximation and Eq. (11) taken together give an approximate analytical representation of the drag coefficient over practically the entire range of supersonic velocities. At very high Mach Numbers, $C_D \to 2.08 \sin^2 \theta_c$ for $\gamma = 1.405$, which is close to the Newtonian value.

Recently, hypersonic similarity has been shown to apply also for the slender yawed cone at moderate supersonic speeds.[7] In principle, there would seem to be no difficulty in extending the present considerations to this case, and perhaps also to ogival bodies.

REFERENCES

[1] Tsien, H. S., *Similarity Laws of Hypersonic Flows*, Journal of Math. and Physics, Vol. 25, No. 3, October, 1946.

[2] Hayes, W., *On Hypersonic Similitude*, Quart. of Appl. Math., Vol. V, No. 1, April, 1947.

[3] Ehret, D. M., Rossow, V. J., and Stevens, V. I., *An Analysis of the Applicability of the Hypersonic Similarity Law to the Study of the Flow about Bodies of Revolution at Zero Angle of Attack*, N.A.C.A. T.N. No. 2250, December, 1950.

[4] Taylor, G. I., and Maccoll, J. W., *The Air Pressure on a Cone Moving at High Speeds*, Proc. Roy. Soc. (London) A, 139, pp. 278–311, 1933.

[5] Staff of the Computing Section, Center of Analysis (under the direction of Zdenek Kopal), *Tables of Supersonic Flow Around Cones*, Tech. Report 1, 1947.

[6] von Kármán, Theodore, *The Problem of Resistance in Compressible Fluids*, Proc. 5th Volta Congress, Rome, 1935, pp. 210–271 (GALCIT Pub. No. 75, 1936).

[7] Neice, S. E., and Ehret, D. M., *Similarity Laws for Slender Bodies of Revolution in Hypersonic Flows*, Journal of the Aeronautical Sciences, Vol. 18, No. 8, pp. 527–530, 568, August, 1951.

[8] Shen, S. F., *Hypersonic Flow Over a Slender Cone*, Journal of Math. and Physics (M.I.T.), Vol. XXVII, No. 1, April, 1948.

A Limitation on Shock Position

E. W. Graham
Consultant in Aerodynamics, Douglas Aircraft Company, Inc., Santa Monica, Calif.

May 18, 1951

THE FOLLOWING DEVELOPMENT APPLIES in the steady adiabatic flow of a compressible fluid past a body if the flow upstream is uniform. The Mach Number and body fineness ratio are not restricted, but the results should be of greatest interest for blunt bodies and Mach Numbers slightly greater than unity.

The maximum mass of fluid which can flow through a unit cross-sectional area in unit time is $\rho^* a^*$ (where ρ^* is the density and a^* is the fluid velocity existing when the speed of sound is reached locally). For a steady flow $\rho_1 {}^* a^*$ (the value of $\rho^* a^*$ in the uniform free stream ahead of a body) cannot be exceeded at any other point in the flow. The value of a^* is constant, and ρ^* behaves in the same fashion as stagnation pressure and can only decrease as the entropy is increased by viscous effects and shocks.

Since an upper limit for the mass flow of fluid is known, it is possible to establish an inner limit on shock position based on con-

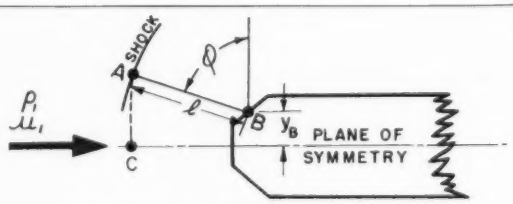

FIG. 1.

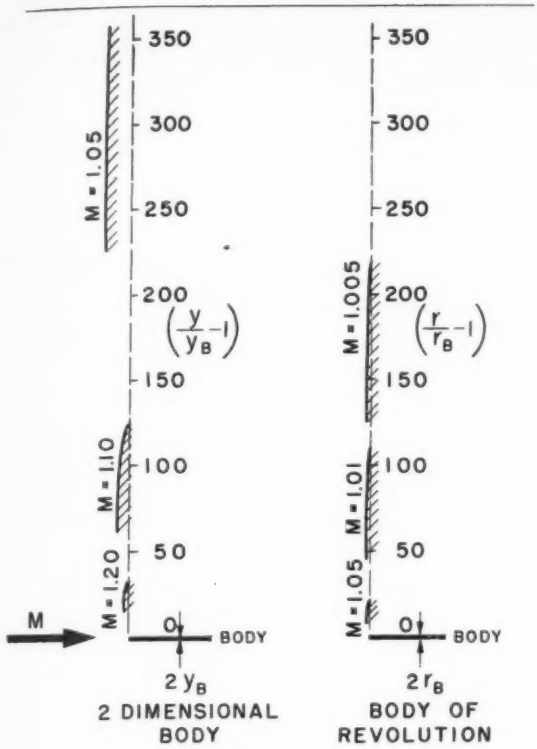

FIG. 2.

tinuity. For the two-dimensional body shown in Fig. 1, the maximum possible flow across the line AB is $\rho_1{}^*a^*l$. The flow across the line AC is $\rho_1 u_1(l \cos \varphi + y_B)$ and by continuity

$$\rho_1{}^*a^*l \geq \rho_1 u_1(l \cos \varphi + y_B)$$

Therefore,

$$l \geq \{y_B/[(\rho_1{}^*a^*/\rho_1 u_1) - \cos \varphi]\}$$

By finding l for different points on the body and different angles φ, an inner limit for the shock position is established.

A similar analysis can be made for bodies of revolution, assuming that the line AB lies in a conical surface connecting the circle of body points at one radius with the circle of shock points at another radius. However, a more positive statement about shock position can be made by considering the flow through the surface of minimum area connecting the two circles. In the two-dimensional case, AB was a line element in a plane, and the plane was the surface of minimum area connecting the specified end points. For the body of revolution the corresponding conical surface is not the surface of minimum area connecting the circle of shock points with the circle of body points. The minimum area surface is obtained by rotating the catenary

$$y = C_1 \cosh [(x - C_2)/C_1]$$

about the axis of the body, C_1 and C_2 being determined by the end points.

This makes the geometry considerably more complicated for the rotationally symmetric case. The distinction between the conic surface and the surface of minimum area is probably most important as the Mach Number approaches unity.

The actual shock position lies outside of the limit calculated above for two reasons: (1) The actual ρ^*a^* behind the shock is less than the limiting value $\rho_1{}^*a^*$ because of entropy increases; (2) These actual values of ρ^*a^* are, in general, not attained at every point on the surface of minimum area. It can be concluded from (1) that the limiting shock position could be far from the actual position at high Mach Numbers where the entropy increases are large. However, at Mach Numbers slightly greater than unity, the agreement might be good, depending upon the shape of the sonic line.

In Fig. 2 the significant portion of the limiting shock position is shown for two-dimensional bodies and bodies of revolution at several Mach Numbers.

Comment on "Vibration of Rectangular Plates"

Charles Massonnet
Université de Liège, Belgium
June 8, 1951

IN NOTE IN THE READERS' FORUM of February, 1951, the paper by Harold Lurie entitled "Vibrations of Rectangular Plates." Nearly the same demonstration is given in my book entitled *Les relations entre les modes normaux de vibration et la stabilité des systèmes élastiques*, published in 1940. This book formed parts 1 and 2 of the *Bulletin des Laboratoires d'essais des Constructions du Génie Civil de l'Université de Liège*. (See pages 273–287.)

Author's Reply

Harold Lurie
The RAND Corporation
June 15, 1951

IN A READERS' FORUM NOTE (February, 1951), I derived an expression relating the natural frequency of vibration of a rectangular plate and the plate buckling factor k. It has subsequently been brought to my attention that Massonnet had previously derived an expression relating the natural frequency to the buckling load. My note does, however, present the results in terms of the N.A.C.A. buckling factors, enabling actual numerical calculations of frequency to be made by direct use of the N.A.C.A. tables.

Shear Flow in a Thin-Skin Tapered Beam

H. W. Sibert
Professor in Aeronautical Engineering, University of Colorado
June 22, 1951

SUMMARY

It is proved that a simple formula involving the shear force carried by the webs, which is sometimes used for the shear flow in a thin-skin tapered beam, is not valid in general but will give correct results under certain specified conditions.

SYMBOLS

I = moment of inertia of the cross section under investigation about its x axis
M = external bending moment about x axis of the cross section (+ when compression at + values of z)

V = total shear force on the cross section (assumed to be parallel to z axis and + when in $+z$ direction)
V_s = portion of V carried by the stiffeners of the cross section (+ when in $+z$ direction)
V_w = portion of V carried by the webs of the cross section (+ when in $+z$ direction)
A_i = area of ith stiffener of the cross section
P_i = normal force on A_i (+ when compression)
z_i = distance from x axis of cross section to centroid of area A_i
s_i = dz_i/dy
q_i = difference in shear flow in the two webs of the cross section on either side of area A_i
n = number of stiffeners intersecting the cross section

NOTE: Subscript i will be used to indicate a particular stiffener. Subscript k will be used instead of i when a summation is to be taken for all the stiffeners of a cross section.

ASSUMPTIONS

IN THE FOLLOWING ANALYSIS it will be assumed that:

(1) The x axis is a principal axis of the cross section under investigation, and the y axis is perpendicular to this cross section.

(2) The skin of the beam is thin enough to assume that only the stiffeners resist the bending.

(3) The cross-sectional area of each stiffener is constant throughout its length.

(4) Each stiffener is sufficiently far from the x axis for $z_i^2A_i$ to be its moment of inertia about the x axis to a close approximation.

(5) The curvature of each stiffener is small enough to assume that the axis of the stiffener is a straight line.

Although an analysis can be made when the curvature of the stiffeners cannot be neglected, it would be difficult to draw any general conclusions from the resulting formulas.

FORMULAS

Consider a portion of the beam of longitudinal length dy. The difference between the normal forces on the two ends of the ith stiffener is dP_i, and the difference in transverse shear flow in the two webs of the cross section on either side of area A_i is $q_i = dP_i/dy$. Since the bending stress at area A_i is Mz_i/I, $P_i = A_iMz_i/I$. Since $dM/dy = V$ and $dz_i/dy = s_i$,

$$q_i = (Vz_iA_i/I) + (Ms_iA_i/I) - (Mz_iA_i/I^2)dI/dy \qquad (1)$$

Instead of Eq. (1), the following simple formula for q_i is sometimes used:

$$q_i = V_wz_iA_i/I \qquad (2)$$

with V_w the shear force carried by the webs of the cross section. The validity of Eq. (2) will now be investigated.

Since the correct value of q_i is given by Eq. (1), a necessary and sufficient condition for Eq. (2) to give the correct value of q_i for each stiffener can be found by equating the right sides of Eqs. (1) and (2). Since $V - V_w = V_s$ by definition, the resulting equation when multiplied by I^2/Mz_iA_i is

$$(V_sI/M) + (Is_i/z_i) - (dI/dy) = 0 \qquad (3)$$

Since the normal force P_k on A_k is parallel to the y axis, the z-component of the resultant force on A_k is $P_k\,dz_k/dy = P_ks_k = Ms_kz_kA_k/I$. Then V_s, the shear force carried by all the stiffeners, is

$$V_s = \sum_{k=1}^{n} P_ks_k = (M/I)\sum_{k=1}^{n} s_kz_kA_k \qquad (4)$$

Since it was assumed that only the stiffeners resist the bending and since $dz_k/dy = s_k$, it follows from Assumption (4) that

$$I = \sum_{k=1}^{n} z_k^2A_k, \qquad dI/dy = 2\sum_{k=1}^{n} s_kz_kA_k \qquad (5)$$

The substitution in Eq. (3) of the above values of V_s, I, and dI/dy gives

$$(s_i/z_i)\sum_{k=1}^{n} z_k^2A_k - \sum_{k=1}^{n} s_kz_kA_k = 0 \qquad (6)$$

as a necessary and sufficient condition for Eq. (2) to give the correct value of q_i in the ith stiffener.

Now consider the lines formed by projecting the axes of the stiffeners upon the yz plane. Since all of these projection lines cannot be parallel in a tapered beam, at least two of them must meet at a point (call it 0). If y is measured from point 0, it follows from Assumption (5) that the equations of these projection lines are:

$$z_k = b_k + s_ky \qquad (7)$$

in which b_k is a constant for each projection line and $b_k = 0$ for the projection lines that meet at point 0.

Since Eq. (6) must be satisfied for each stiffener if Eq. (2) is to give the correct value of q_i at each stiffener, a necessary condition for the validity of Eq. (2) can be based upon the projection lines that meet at point 0, for which $z_i = s_iy$. Then Eq. (6) for these particular projection lines becomes

$$(1/y)\sum_{k=1}^{n} (b_k + s_ky)^2A_k - \sum_{k=1}^{n} s_k(b_k + s_ky)A_k = 0 \qquad (8)$$

which reduces to

$$(1/y)\sum_{k=1}^{n} b_k^2A_k + \sum_{k=1}^{n} b_ks_kA_k = 0 \qquad (9)$$

Note that b_k, s_k, and A_k are constant for each stiffener and, hence, are independent of y. Since Eq. (9) must be valid for all cross sections of the beam (that is, for all values of y for which there is a cross section of the beam), each summation in Eq. (9) must separately equal zero. Hence, it is necessary that

$$\sum_{k=1}^{n} b_k^2A_k = 0 \qquad (10)$$

if Eq. (2) is to give the correct value of q_i at each stiffener. Since neither b_k^2 nor A_k can be negative, Eq. (10) will not be satisfied if each b_k is not zero. Hence, each $b_k = 0$ is a necessary condition for Eq. (2) to give the correct value of q_i at each stiffener. Conversely, if each $b_k = 0$, Eq. (9) reduces to zero. It follows, then, that:

A necessary and sufficient condition for Eq. (2) to be valid for a thin-skin tapered beam composed of essentially straight stiffeners is that the lines formed by projecting the axes of the stiffeners upon the yz plane shall all meet at one point.

It should be noted that this condition rules out the use of Eq. (2) in the important case of a wing with straight stiffeners which is tapered in both plan form and thickness.

Note that from Eqs. (4) and (5), $dI/dy = 2V_sI/M$. The substitution of this value of dI/dy in Eq. (1) gives

$$q_i = [(V - 2V_s)z_i + Ms_i]A_i/I \qquad (11)$$

If the condition mentioned above in italics is not satisfied, Eq. (11) should be used instead of Eq. (2). Note that Eq. (11) is only slightly more difficult to apply than Eq. (2), because in using Eq. (2) it is necessary to calculate V_s before V_w (which equals $V - V_s$) can be found.